A Study of Highly Deformed α-Cluster Structures in Light Nuclei

Peter Mark Simmons
Trinity College

A thesis submitted in fulfillment of the requirements
for the degree of Doctor of Philosophy
in the University of Oxford

Trinity Term 1995

To my parents

A Study of Highly Deformed α-Cluster Structures in Light Nuclei

Peter Mark Simmons

Trinity College, Oxford

A thesis submitted in fulfillment of the requirements
for the degree of Doctor of Philosophy
in the University of Oxford

Trinity Term 1995

Abstract

The inelastic scattering reaction $^{16}O+^{12}C$ has been studied in the centre-of-mass energy region from 37.7 MeV to 51.4 MeV, in a search for evidence for a seven-alpha chain state in ^{28}Si. The decay products were detected in coincidence at angular separations around 90° in the centre of mass using two position-sensitive strip detectors. Kinematic reconstruction of the quasi-three body final states yielded the differential cross-sections for the decay channels leading to excited states in ^{12}C, ^{16}O and ^{20}Ne.

The excitation functions measured for the $^{12}C(0_2^+)$-$^{12}C(0_2^+)$-α and $^{12}C(0_2^+)$-^{8}Be-^{8}Be final states agree broadly between the three experiments that were performed, but contain no structure. Reaction channels have also been identified leading to the ^{8}Be-$^{20}Ne^*$ and $^{12}C^*$-$^{16}O^*$ final states. The cross-sections for the ^{8}Be-$^{20}Ne^*$ decay channels, with the ^{20}Ne in its lowest excited states, have been compared with previous measurements and provide good agreement. However, none of the excitation functions for these channels contain any structure.

The absence of structure in any of the final states, that were identified in this study, indicates that a ^{28}Si chain state is probably not being observed. The same model, that predicts that the seven-alpha chain state should lie in this excitation region in ^{28}Si, has also been used to assign a six alpha chain structure to a resonance at E_x=46.6 MeV in ^{24}Mg. These two results are compared, and possible reasons for the absence of evidence for a ^{28}Si chain structure are discussed.

Acknowledgements

First I would like to thank Professor R. Cashmore for allowing me to use the excellent facilities of the Nuclear Physics Laboratory and the Engineering and Physical Sciences Research Council for a postgraduate studentship, without which this work would not have been possible.

I am especially indebted to my supervisor Dr. W.D.M. Rae for his constant encouragement and advice throughout my time at Oxford. He taught me how to conduct research, inspired me and offered me endless patience and advice.

A large number of people worked hard to help make the experiments a success; my apologies and thanks to anyone who may have been inadvertently omitted from the following list.

I wish to thank my fellow collaborators from the Universities of Birmingham, Surrey and York, especially Brian Fulton, and in particular Steve Chappell, Simon Fox and Chris Jones for a fruitful working relationship in Australia and for being so polite about my driving.

The first two experiments were performed at the Nuclear Structure Facility, Daresbury. These would not have been possible without the technical expertise of Tom Davinson and the organisational skills of John Lilley. I am also most grateful to the workshop staff and operators for ensuring the smooth running of the accelerator.

In Australia my thanks go to all of the technical and research staff for their invaluable support and hospitality, particularly Paddy Regan for liaising on our behalf.

In Oxford itself, there are a large number of people to whom I am grateful. Within the Charissa group, my thanks go to Alan Merchant, Jie Zhang and Peter Fry who have answered my innumerable questions with patience and have kept me company at coffee; Dick Hunt imparted knowledge of the electronics and the wider world and Pete Gronbech kept the computers up and running.

The staff and Fellows of Trinity College deserve a special mention for providing a friendly home within Oxford, and a generous travel grant to allow me to attend the Santorini conference.

Without my friends in the MCR and my house-mates, I would not have survived the last four years - nor had such a good time along the way. I am particularly grateful to the German contingent, and to Stefanie for her e-mails. Dom, Gerd and Dan have been a great source of encouragement, especially Domenico whose cooking has sustained me.

Finally, and most of all, I would like to thank my parents and my sister, Jane, for their continuing support, encouragement and love, and Shannon, for her warm friendship and for always being there.

Contents

List of Figures

Chapter 1

Introduction

Extreme deformation of the nucleus has long held a fascination for nuclear physicists. This phenomenon is most pronounced in the light nuclei [Afz 67, Hor 72], however it is not exclusive to them. Indeed perhaps one of the clearest examples of deformation is found in the so-called superdeformed band in ^{152}Dy [Nya 84, Twi 85] which is seen to have a prolate shape with an axis ratio of 2:1. Through the detailed study of these structures, it is expected that significant advances can be made in our understanding of the centrifugal and structure effects, acting on nuclear matter at high angular momentum, and at the edge of stability.

The following sections detail this study for the light A=4N alpha conjugate nuclei and discuss the evidence for extremely deformed structures in these nuclei.

1.1 Introduction to Clustering

Although there are many different nuclear models, for the purposes of studying deformed states, a cluster model approach is usually taken. The purpose of introducing the cluster concept is to help us to think more clearly about the processes taking place within the nucleus and also to make calculations simpler. In addition, by referring to clusters, the concept of deformation can be easily and naturally introduced. Clustering is defined relative to the nucleon structure of the nucleus, with models assuming that protons and neutrons form groups within the nucleus. While recognising that interchange between groups occurs, these models nevertheless depend for their validity on the assumption that the diffusion does not go on at such a rate that the groups lose their identity during one characteristic period of nuclear rotation.

The probability of formation of a particular cluster is largely determined by its binding energy and this implies that, of all possible clusters, the alpha particle cluster is the most probable. The idea of alpha clustering within the nucleus was first suggested by Gamow in 1929 after his studies of alpha decay [Gam 29]. However it was not until 1937, when Wheeler [Whe 37], Wefelmeier [Wef 37] and later Margenau [Mar 41] formulated alpha cluster models which explicitly took into account the separate alpha particles, that the study of clustering within nuclei began.

Brink and Castro [Bri 73] have shown that the onset of alpha clustering depends on the nuclear density. They found that nucleons condense into alpha particles when the density falls to about one-third of the central nuclear density. This suggests that alpha particle formation may be energetically favoured in the region of the nuclear surface and hence that light nuclei, which are essentially all surface, will have a pronounced cluster structure. This is expected to be enhanced if they contain 2N neutrons and 2N protons and so can be formed entirely of alpha particles.

1.2 Clustering in Light Nuclei

From the observations above it is perhaps not surprising that the nucleus to which Wheeler, Wefelmeier and Margenau chose to apply their model was ^{8}Be.

The ground state of ^{8}Be is a quasi-bound state which lies 92 keV above the alpha-decay threshold. It constitutes a rotational band together with the excited 2^+ and 4^+ states at 3.04 MeV and 11.4 MeV respectively. No other levels are observed in the excitation spectrum below about 17 MeV [Ajz 88]. It was found that the intrinsic structure of ^{8}Be could be well modelled using an $\alpha - \alpha$ effective potential, with repulsion between the alpha particles originating from the Pauli principle [Afz 67]. The large moment of inertia calculated from the rotational band gives an $\alpha - \alpha$ separation of about 4 fm.

After this initial success, attempts were made to examine other nuclei using alpha cluster techniques. In ^{16}O, Dennison suggested a tetrahedral symmetry for the ground state [Den 54]. The agreement between his predicted energy levels and those observed experimentally [Bit 54] was sufficiently good to suggest that this model contained some degree of correctness. This led Ikeda to attempt to systematise the occurrence of clustering phenomena [Ike 68] by generalising an original idea by Morinaga [Mor 56]. Ikeda suggested that cluster-like configurations would appear in A=4N self conjugate nuclei near the decay threshold for decay into the relevant sub-nuclei. Using this hypothesis he successfully predicts the $\alpha - \alpha$ cluster structure of ^{8}Be. In addition the rotational band based on the 6.05 MeV 0_2^+ in ^{16}O is believed to have a ^{12}C-α cluster configuration [Rae 88]. However, it is his prediction of chain-like configurations that is of most interest here. He predicts that these will occur in essentially all A=4N alpha conjugate nuclei just above the nα threshold.

1.3 Chain States in A=4N Alpha Conjugate Nuclei

In addition to the predictions by Ikeda, chain states have been shown to be stable using a number of different nuclear models. Although most of these calculations have concentrated on ^{12}C and ^{16}O, for example those by Nilsson [Nil 55] and the Hartree-Fock calculations by Zamick, Zheng and Sprung [Zam 92], there have nevertheless been some studies of the heavier A=4N alpha conjugate nuclei.

Leander and Larsson have calculated the potential-energy surfaces for all doubly even N=Z nuclides from ^{12}C to ^{44}Ti as a function of deformation [Lea 75]. In each nucleus they find a number of local minima including, in each case, a minimum corresponding to a linear alignment of the alpha particles. The minima observed in the potential-energy surface of ^{24}Mg have been studied in more detail by Marsh and Rae [Mar 86] using the Bloch-Brink alpha cluster model [Bri 66] with the cranking approximation [Rae 85a]. They calculate that the six alpha chain state should lie at an excitation energy of 43.6 MeV. Subsequently, Merchant and Rae have extended these calculations to predict the excitation energy of the chain states in essentially all A=4N alpha conjugate nuclei [Mer 92].

Horiuchi, Ikeda and Suzuki [Hor 72] have made an extensive study of the stability of chain states by extending their effective $\alpha - \alpha$ interaction model which was able to reproduce the properties of ^{8}Be. They found that instabilities may arise along the direction of the two kinds of displacements, that is, the transverse and longitudinal ones. In the transverse direction, the instability occurs due to mixing with lower order molecular structures. If the amplitudes of the transverse vibrational modes become very large, then the alpha particles may connect with one another resulting in the decay of the chain. In the longitudinal direction, the instability is due to decay or fission. If the energy of the chain is near or larger than the Coulomb plus centrifugal barrier for the decay or fission modes then the chain structure cannot be realised. From these studies they concluded that nα-chain (n$\geq$5) structures have a high probability for existence as a quasi-bound state or a resonance. They also hypothesised on the possible formation and decay mechanisms of chain states. They expected that chains would be formed through two body interactions when

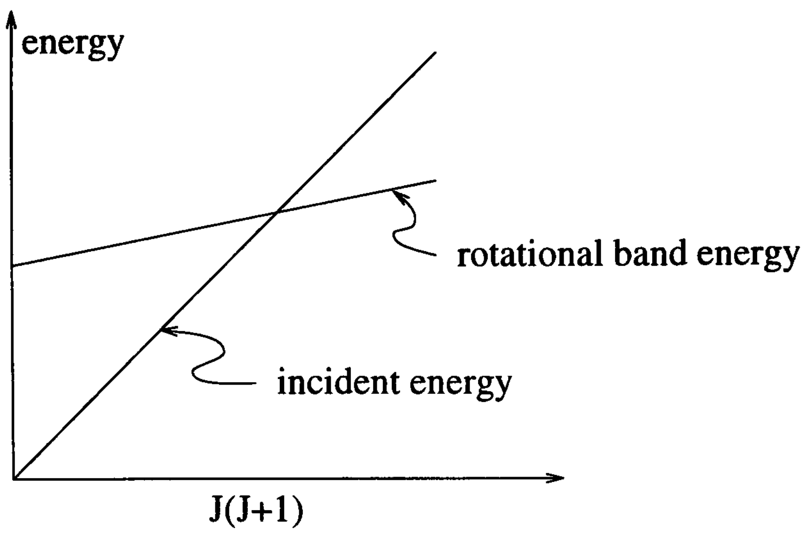

Figure 1.1: *The relation between the incident energy with relative angular momentum J and the energy of the chain state band.*

Nucleus	α-decay threshold (MeV)	Experiment (MeV)	Theoretical Predictions (MeV)	
			[Hor 72]	[Mer 92]
^{8}Be	-0.093	0.0	-	0.0
^{12}C	7.272	7.65	8.2	7.9
^{16}O	14.433	(16.75)	16.7	18.9
^{20}Ne	19.167	-	23.3	31.7
^{24}Mg	28.477	(46.4)	34.7	45.5
^{28}Si	38.460	-	47.2	60.2
^{32}S	45.408	-	56.8	75.5

Table 1.1: *A table comparing the experimental chain state assignments with the predictions from [Hor 72] and [Rae 92].*

the energy and relative angular momentum of the beam and target nuclei matched that of the J-state in the rotational band, shown in Figure 1.1. It was noted that these states would decay dominantly into the specific channels where the fragment nuclei are also of chain configurations.

A compilation of some of the predictions for the excitation energies of chain states is shown in Table 1.1

1.4 Experimental Aspects of Chain States

In the above introduction to chain states, very little has been said about the experimental work that has been performed in the search for chain structures. In fact, there is also a large body of experimental data which has been built up to support or refute the chain state hypothesis. As experiments have generally been performed on a nucleus by nucleus basis, the remainder of this introduction will be split into sections to cover each nucleus in turn. It is generally taken that the structure of the ^{8}Be ground state is that of a two alpha chain, as described in Section 1.2, so that this nucleus is not covered here.

1.4.1 ^{12}C

In ^{12}C, the best candidate for a chain state is the 0_2^+ state at 7.65 MeV, however this assignment is one of the most controversial and uncertain of all of the suggested $n\alpha$ chain states.

Interest in this excited state derives mainly from Astrophysics. At stellar densities and temperatures, the direct formation of ^{12}C through the $\alpha + \alpha + \alpha \rightarrow ^{12}$C, is inhibited by the negligible probability that three alpha particles will simultaneously collide. Therefore in order to explain the presently observed abundance of ^{12}C, an alternative production mechanism was required. A solution was proposed by Salpeter and Öpik [Öpi 51, Sal 52] who suggested that ^{12}C could be formed through a two stage process, $\alpha(\alpha,^{8}\text{Be})$ followed by the reaction $^{8}\text{Be}(\alpha,\gamma)^{12}\text{C}$. However this was still not enough to account for the observed abundance. Hoyle [Hoy 53] speculated that the reaction rate of the second stage of ^{12}C formation may be enhanced if the reaction proceeded via an s-wave resonance in ^{12}C close to the formation threshold. This prediction was subsequently verified experimentally, when a resonance which possessed the required properties (E_x=7.65 MeV and $J^{\pi}=0^+$) was discovered in studies of the $^{14}\text{N}(\text{d},\alpha)^{12}\text{C}$ [Hoy 53] reaction and the β decay of ^{12}B [Coo 57].

The 0_2^+ level is located 379 keV above the alpha threshold energy and has a very large alpha-decay width. This led Morinaga to suggest that it may have a linear chain structure [Mor 56]. He subsequently added that a possible 2^+ assignment to the 10.3 MeV state may constitute a deformed band in ^{12}C [Mor 66]. The spin assignment of the 10.3 MeV level is still uncertain but it now seems more likely that a 0^+ assignment should be made [Ajz 90].

Although the electron form factors indicate that both the 7.65 MeV and 10.3 MeV levels have a large deformation [Fla 78, Cra 79], the chain assignment has been questioned in a number of studies. Takigawa and Abgrall [Tak 71, Abg 74] found that, using a Brink-type three-alpha model [Bri 66], the rather strong $0_2^+ \rightarrow 0_{g.s.}^+$ monopole and $0_2^+ \rightarrow 2_1^+$ E2 transitions could not be explained unless an artificial mixture of the equilateral triangle and linear chain three-alpha geometries were assigned to both the 0_1^+ and 0_2^+ states. Horiuchi suggested [Hor 72] that, on the basis of the magnitude of the level spacing between the 0_2^+ and 2_2^+ (10.3 MeV) levels, which is similar to that of the ground state band in ^{8}Be, a weakly coupled $\alpha-^8$Be structure may be more appropriate. This structure assignment has been strengthened by the work of Kamimura [Kam 81] who used the 3α-Resonating Group Method (RGM) wavefunctions obtained by Fukushima and Kamimura [Fuk 77] to examine the transition densities between the 0_1^+, 2_1^+, 4_1^+, 0_2^+, 2_2^+, 1_1^- and 3_1^- states. He concluded that the 0_2^+ and 2_2^+ states have a dominant weakly coupled ^{8}Be$_{g.s.}$-α molecule-like configuration.

A true linear chain might be expected to lie at higher excitation energies. Using a recent model of ^{16}O [Rae 94b], Rae and Merchant have speculated that the chain may be formed when the ^{8}Be is in its 2^+ state. Thus the linear chain might be some 3 MeV (viz. the excitation of the ^{8}Be(2^+)) above the "bent chain". Generator Coordinate Method (GCM) calculations [Zha 95] support this speculation. The role of the 10.3 MeV (0_3^+) level may therefore be important.

1.4.2 ^{16}O

In the case of ^{16}O, all of the experimental information about the states which are assigned to have a chain structure of four alpha particles, are supplied by a single experiment by Chevallier et al. using the breakup reaction ^{12}C(α,^{8}Be)^{8}Be [Che 67]. A number of positive parity resonances were identified between 16.95 MeV and 19.35 MeV with spins between 2 and $6\hbar$. Chevallier noted that three of the four most prominent and clearly established levels, at 17.15 MeV (2^+), 18.05 MeV (4^+) and 19.35 MeV (6^+) appeared in the exact energy spacing associated with a rotational band structure with an interpolated position for the 0^+ level of the band at 16.75 MeV. However he also observed that the widths of these levels, shown in Table 1.2, do not exhibit any clear and regular pattern. In particular he was not able to explain the extremely narrow width of the 4^+ level. From the large moment of inertia calculated for this band, Chevallier concluded that the only conceivable structure was of four alpha particles laid out in a string and rotating rigidly. The distance between centres of adjacent alphas in this configuration is 4.1 fm.

Brink et al. [Bri 70] have performed a 'microscopic' calculation using an alpha particle model to calculate the excitation energy of the chain state relative to the ^{16}O ground state. Their spectrum, obtained from this chain state configuration by angular momentum projection, showed a strong resemblance to the observed levels,

J^π	E_x (MeV)	Γ_{total} (keV)
0^+	16.75	-
2^+	16.95	370
2^+	17.15	260
4^+	18.05	20
6^+	19.35	70

Table 1.2: *The widths of the resonant states in ^{16}O observed by the reaction $^{12}C(\alpha,^{8}Be)^{8}Be$ [Che 67].*

however, using this model they were unable to explain the anomaly in the decay widths. This has been explained by Suzuki et al. [Suz 72] who performed a coupled channels calculation taking into account all of the possible two body break-up channels. They found good agreement between their calculated total widths and the observed widths for the 4^+ and 6^+ resonances. For the 2^+ state the calculated total width was of the same order of magnitude as the 4^+ and 6^+, while the experimental Γ_{total} is about ten times larger. They suggest that this is the result of coupling of the chain with a nearby compound state at 16.95 MeV, then the large widths of the two 2^+ levels can be attributed to single nucleon decays. Thus they conclude that the information concerning widths is not unfavourable for the assumption of a four alpha chain.

There have recently been two new experimental studies of the ^{16}O excitation region up to ~20 MeV. The first of these was by Ames [Ame 82]. He performed a systematic study of ^{16}O levels using the ^{12}C+α reaction in the range 15 MeV<E_x(^{16}O)<22 MeV at over one thousand energies. He found a number of resonant states decaying to ^{12}C(0_2^+)+α which have been assigned chain state structures on the basis of their decay through this channel. Freer et al. [Fre 95] have examined the states in ^{16}O which decay into ^{8}Be+^{8}Be or ^{12}C(0_2^+)+α using the ^{12}C(^{16}O,4α)^{12}C reaction. They observed a number of resonances which could be associated with those observed by Chevallier [Che 67] and Ames [Ame 82], however they assigned a spin of J=4 to a resonance observed at 19.3 MeV in contrast to its previous J=6 assignment [Che 67].

1.4.3 ^{20}Ne

The optimum reaction channel to form a five alpha chain should be ^{12}C+^{8}Be, however because of the short lifetime of the ^{8}Be ground state (~10^{-16} s) this reaction is not possible. There have been many studies of the $\alpha+^{16}O$ reaction up to 25 MeV and a number of resonances have been identified in this energy region. Due to technical limitations of the detector systems, no studies have been made of the ^{8}Be-$^{12}C(0_2^+)$ and α-$^{16}O_{chain}$ decay channels. Thus no chain structure has been identified in this nucleus.

1.4.4 ^{24}Mg

Possible evidence for a chain state in ^{24}Mg has recently been found by a group in Argonne [Wuo 92]. For ^{24}Mg, a decay channel of particular interest is $^{24}Mg^* \rightarrow ^{12}C(0_2^+)$ $+^{12}C(0_2^+)$. Since the $^{12}C(0_2^+)$ is known to have a large deformation, structural and phase space considerations suggest that a six-alpha chain structure in ^{24}Mg should have a large branch for symmetric breakup into a final state consisting of two ^{12}C nuclei in their 0_2^+ levels. Therefore the observation by Wuosmaa et al. of a strong resonance at an energy of $E_{c.m.}$=32.5 MeV with $\Gamma_{c.m.}$=4.7 MeV in the mutual scattering reaction $^{12}C+^{12}C\rightarrow^{12}C(0_2^+)+^{12}C(0_2^+)$, shown in Figure 1.2a, has been interpreted as a signature for the existence of an elongated structure in ^{24}Mg, possibly a six-alpha chain. It is thought that the chain is being populated directly, as a result of mixing of cluster configurations in the ^{12}C ground state and 0_2^+ level [Hor 72, Rae 94c].

Another feature of this resonance is the behaviour of the angular distribution around 90° in the centre of mass frame, see Figure 1.2b. The cross-section on resonance is very strongly enhanced near 90° and significantly more pronounced than the neighbouring local maxima. Rae, Merchant and Buck have suggested that as a result of the large moment of inertia of this band, the resonances with different angular momenta are very closely spaced, becoming effectively degenerate [Rae 92a]. This manifests itself as a definite spacial alignment which is observed through the unusual angular distribution associated with the $^{12}C(0_2^+)$-$^{12}C(0_2^+)$ decay channel.

An alternative explanation of these phenomena has been offered by Hirabayashi et al. [Hir 95]. They have extended the Band Crossing Model [Abe 78, Mat 78, Kon 79] to di-nuclear molecular configurations with structure changes, such as from the compact ground state to the spatially extended three alpha particle 0_2^+ state in ^{12}C. By using this model and including all possible ^{12}C-^{12}C channels, they find that the dominant configuration of the resonance is of two ^{12}C nuclei weakly coupled and both in their 0_2^+ state. The angular distribution thus obtained provides a good fit to the experiment 'on-resonance', however the quality of the 'off-resonance' fit is not as good. In particular, the 90° enhancement seen 'on-resonance' is present in their

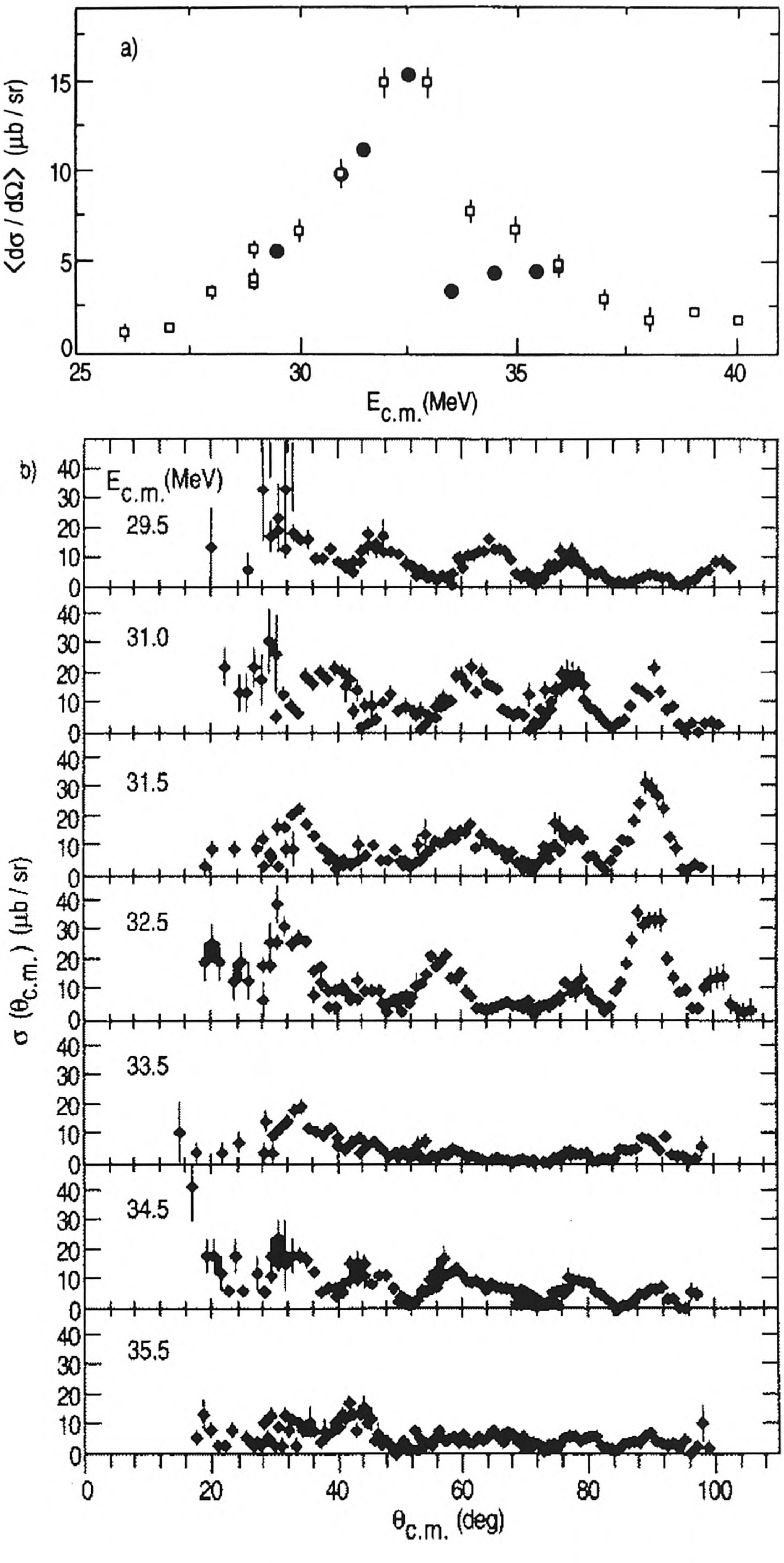

Figure 1.2: *a) A comparison between the excitation functions measured for the $^{12}C(^{12}C,^{12}C(0_2^+))^{12}C(0_2^+)$ reaction from References [Wuo 92] (squares) and [Wuo94b] (circles) taken from Reference [Wuo94b] and b) the corresponding angular distribution data for the same reaction from Reference [Wuo 94b].*

model at all energies, contrary to the fluctuations observed in the data.

The cranked cluster model used by Marsh and Rae to predict the excitation energy of the six-alpha chain [Mar 86] also predicts band crossings of the chain state with some two-dimensional configurations, built on different bandheads. This has prompted a number of groups to search in other decay channels in the same centre of mass region for evidence of the decay of the chain.

Aliotta et al. [Ali 95] appear to have observed the decay of this resonance to $^{16}O_{g.s.}$+ ^{8}Be, while Mirgule et al. [Mir 95] observe enhancements of the cross-sections leading to the 13.9 MeV (6^+) and 20.5 MeV (8^+) states in ^{20}Ne. They also see an enhancement of the cross-section for ^{8}Be decay to states around 18 MeV in ^{16}O. Chappell et al. [Cha 95a] have found evidence for this resonance decaying into the $^{12}C(0_2^+)$+$^{12}C(0_3^+$, 10.3 MeV) and $^{12}C(0_2^+)$+$^{12}C(3^-)$ channels. In all cases the cross-sections for these decay modes are much higher than for the $^{12}C(0_2^+)$+$^{12}C(0_2^+)$ channel. In addition to the enhancement of the cross-sections at $E_{c.m.}$=32.5 MeV, Aliotta and Chappell also observe the enhancement of the angular distribution at 90°. No angular distribution measurements have been made by Mirgule et al.

1.4.5 ^{28}Si

The discovery of a possible chain configuration in ^{24}Mg by Wuosmaa et al. [Wuo 92] has led to interest in the identification of chain structures in other A=4N alpha conjugate nuclei in this mass region, particularly in ^{28}Si. Although there is currently no experimental evidence for a seven-alpha chain configuration, we may infer some of its properties by analogy with the six-alpha chain in ^{24}Mg.

The formation mechanism is expected to be through the inelastic scattering reaction ^{16}O+^{12}C, while the only identifiable decay channel, if the chain decays through shorter chains, is $^{12}C(0_2^+)$+$^{16}O_{chain}$. Merchant and Rae have calculated that the excitation energy of the chain will be E_x=60.2 MeV [Mer 92], with an expected width of $\Gamma_{c.m.}$ ≈4 MeV, similar to that of the six-alpha chain. The cross-section for this reaction is expected to be significantly lower than that for the ^{24}Mg chain since the chain structure in ^{16}O resides at a much higher excitation energy. In addition the chain state resonances in ^{16}O are likely to be significantly more difficult to identify than the 0_2^+ level in ^{12}C since the level density at the chain state excitation energy in ^{16}O is much greater.

A compilation of the result from alpha-cluster model calculations by Rae, Merchant and Zhang [Mer 92, Zha 93, Zha 94], shown in Figure 1.3, suggest that band cross-

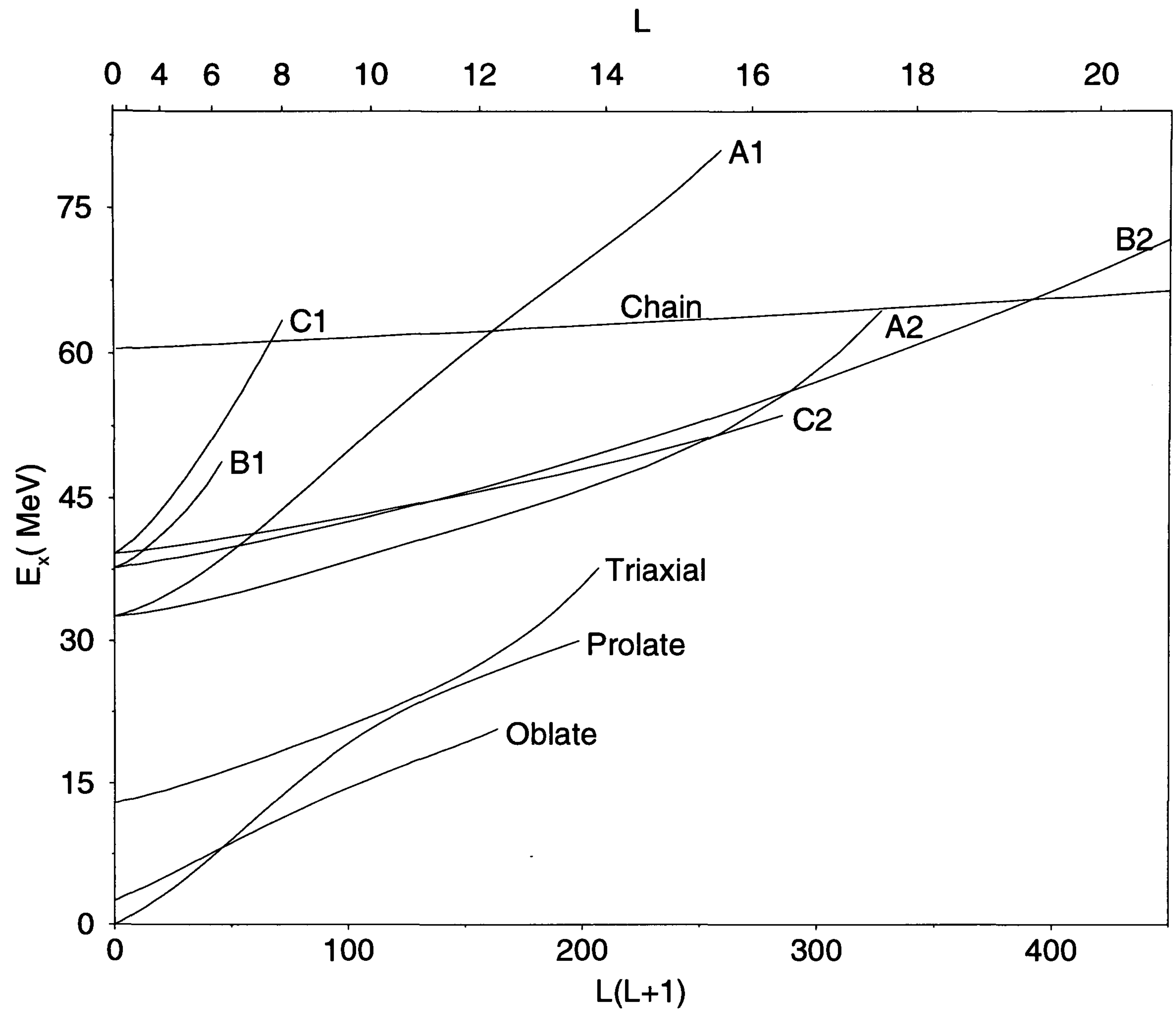

Figure 1.3: *The figure shows a compilation of the rotational energies of calculated* ^{28}Si *configurations as a function of L, from References [Mer 92], [Zha 93] and [Zha 94]. For the triaxial configurations, the energies obtained by cranking about the axes of maximal moment of inertia are plotted. In the case of the two dimensional bands A, B and C, two axes yield similar moments of inertia and so only two curves are shown.*

ings also occurs between the different alpha cluster structures in ^{28}Si. Hence other decay channels may also contain the seven-alpha chain state signature. By comparison with the ^{24}Mg data these decay channels are expected to have a much higher cross-section than the decay through $^{12}C(0_2^+)+^{16}O_{chain}$.

It is these predictions, and the wish to further explore the alpha chain state phenomenon, that is the motivation for the work to be described in this thesis.

1.5 Summary

This chapter has presented a review of the experimental and theoretical evidence for chain structures in A=4N alpha conjugate nuclei. It can be seen that, except in the case of ^{8}Be, the debate concerning chain states is still far from resolution.

In ^{12}C, the 0_2^+ state can be said to be highly deformed, probably with an ^{8}Be-α structure, as a result of mixing between the chain and equilateral triangle alpha cluster configurations. It has been suggested that the 0_3^+ at 10.3 MeV may be a better candidate for the pure linear chain structure.

A rotational band has been identified in ^{16}O built on an unidentified 0^+ level at 16.75 MeV. The level spacing between members of this band exactly matches those for a four-alpha chain with spacings between the alpha particles of 4.1 fm. These levels have been observed to decay via ^{8}Be+^{8}Be and ^{12}C(0_2^+)+α. A number of other resonances have been found in the excitation energy region between 16 and 20 MeV which decay through ^{12}C(0_2^+)+α. These may also have a chain structure.

Although chains have been predicted in ^{20}Ne, there is no experimental evidence for their existence.

An enhancement of the ^{12}C+^{12}C inelastic scattering reaction at $E_{c.m.}$=32.5 MeV has been interpreted as a six-alpha chain in ^{24}Mg. This resonance has a width of 4.7 MeV in the centre of mass and features an unusual enhancement of the angular distribution at 90°. A resonance has also been observed in other decay channels at the same centre of mass energy and with the same properties. It is thought that these alternative decay channels are populated because of band crossings between the chain and other alpha cluster structures.

No seven-alpha chain structure has been identified in ^{28}Si, however some of its properties have been inferred. The remainder of this thesis details the research undertaken to investigate a possible chain state in ^{28}Si.

Chapter 2

Reaction Kinematics

In Chapter 1 the predictions for the excitation energy of a ^{28}Si chain state were discussed, together with some of the properties that such a state may have. The most easily detected decay path is expected to be ^{12}C(0_2^+)+^{16}O$^*_{chain}$, where the ^{16}O decays to ^{8}Be+^{8}Be or ^{12}C(0_2^+)+α, resulting in a seven-alpha-particle final state. In this chapter the kinematic topics relevant to an experimental search for a state of this nature are presented.

2.1 Introduction

A seven body final state would be very difficult to handle if the nucleus decayed to this directly, however, this is not the case, since the decay actually proceeds via well defined states in relatively long lived nuclei, and therefore certain simplifications can be made. Kinematically the reaction ^{12}C(^{16}O,7α) can be treated like a quasi-three-body breakup reaction of the form:

$$\begin{array}{lll} ^{12}\mathrm{C} + ^{16}\mathrm{O} \rightarrow ^{12}\mathrm{C}(0_2^+) + ^{16}\mathrm{O}^*_{chain} & \rightarrow ^{12}\mathrm{C}(0_2^+) + ^{8}\mathrm{Be}_{g.s.} + ^{8}\mathrm{Be}_{g.s.} \\ \qquad\qquad\qquad \text{or} & \rightarrow ^{12}\mathrm{C}(0_2^+) + ^{12}\mathrm{C}(0_2^+) + \alpha. \end{array} \tag{2.1}$$

In this chapter the reaction will be represented by

$$\mathrm{A} + \mathrm{a} \rightarrow \text{Compound System} \rightarrow \mathrm{b} + \mathrm{B}^* \rightarrow \mathrm{b} + \mathrm{c} + \mathrm{d} \tag{2.2}$$

and is shown schematically in Figure 2.1. The decay proceeds sequentially via a state in the decaying ejectile (B*, also referred to as the resonant particle) with definite width, spin and parity. This nucleus subsequently decays to the two body state containing c and d. The quasi-three-body simplification is valid because the

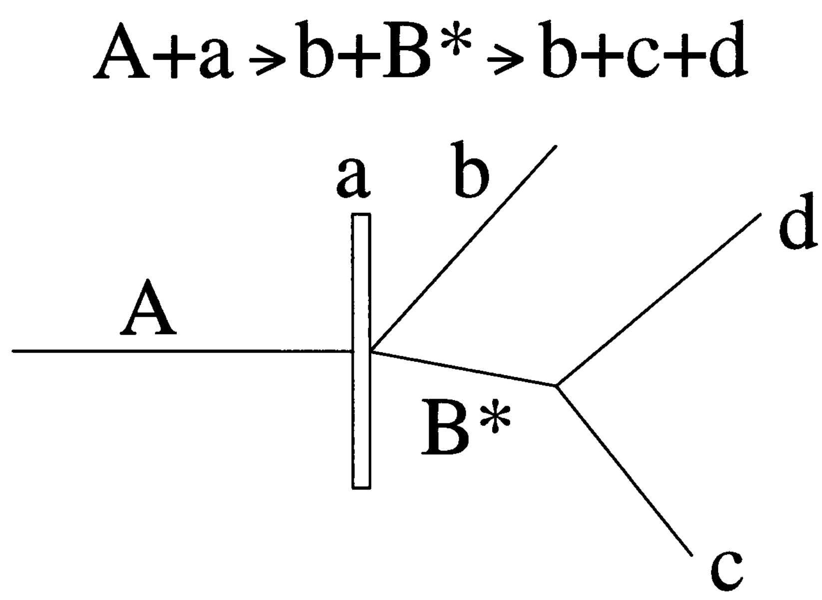

Figure 2.1: *A schematic diagram showing a sequential decay to a three body final state.*

$^{12}C(0_2^+)$ and the $^8Be_{g.s.}$ nuclei in this final state are relatively long lived states with half lives of 0.05 fs [Obs 72] and 0.097 fs [Ben 68] seconds respectively. In addition, they are 0^+ states and decay isotropically in the centre of mass, so that the decay of these nuclei can be treated separately.

Working with this simplification, this chapter will first cover the relevant two and three body kinematics. The process by which the nuclei comprising the quasi-three-body state are rebuilt from their alpha decay products will also be described. Finally, the methods used to calculate yields and differential cross-sections for the observed reactions will be presented.

2.2 Resonant Particle Spectroscopy

In any three body sequential reaction, if at least two out of the three decay products are detected, so that the masses, energies and angles of these two particles are known, then all of the kinematic quantities of the reaction can be calculated. In this way all of the resonant states of the decaying ejectile can be measured simultaneously. This process is called Resonant Particle Spectroscopy (RPS) and is a well known technique in Nuclear Physics [Rob 73].

To increase the efficiency with which the two particles are detected in coincidence, inverse kinematics can be used [Ben 93]. When a heavy beam is incident on a light target, the equivalent centre of mass bombarding energy of the beam particle is at a much higher energy than if the reaction had been performed the other way around. This results in a forward focussing of the decay products, and hence in a greatly increased detection efficiency.

2.3 Reaction Kinematics

The kinematics of breakup reactions have been well covered elsewhere, see for example [Dri 80] and [Rae 85b], and so will only be briefly described here.
By detecting two of the three decay products, the kinematic properties of the undetected particle can be determined using conservation of momentum:

$$\underline{p}_A = \underline{p}_b + \underline{p}_c + \underline{p}_d \tag{2.3}$$

where p_A, p_b, p_c and p_d are the momenta of the particles A, b, c and d respectively. In so doing, the problem can be considered as a quasi-two body reaction problem, with the two nuclei b and B*. In this case it is useful to transform to two new variables:

1. the three body Q value, Q_3
2. the relative kinematic energy, E_{rel}, between the resonant particle decay products c and d.

2.3.1 The Three Body Q-value Q_3

The three body Q-value, Q_3 is defined as the difference between the final and initial state kinetic energies and can be written in the form:

$$Q_3 = E_b + E_c + E_d - E_A \tag{2.4}$$

where E_b, E_c, E_d and E_A are the energies of the particles b, c, d and A. This Q-value is normally negative. When it is calculated for an experiment the various reaction channels are differentiated by their different Q_3. The most positive peak usually corresponds to the case when all three final state particles are in their ground states, this is denoted Q_{ggg}. Channels containing two or one of the three particles in their ground states are denoted Q_{gg} and Q_g respectively. At more negative Q values, peaks appear corresponding to excited states in the two resonant particle fragments.

Energy Resolution in Q_3

The resolution in Q_3, ΔQ_3 will be determined by the uncertainties in the energies of the detected particles and of the beam. Their relative contributions to Q_3 in equation in 2.4 can be found by differentiation and summing in quadrature assuming that none of the effects are correlated:

$$(\Delta Q_3)^2 = (\Delta E_d)^2 + (\Delta E_c)^2 + (\Delta E_b)^2 + (\Delta E_A)^2 \tag{2.5}$$

In fact there are small correlations between these terms, so that this is an approximation. Contributing factors will be detector resolution, beam resolution, energy straggling in the target, effects of differential target thickness, kinematic shifts from the beam spot size and beam divergence. These factors will all contribute approximately in quadrature to ΔQ_3. There may also be kinematic shifts arising from the finite resolution of the detectors.

2.3.2 The Relative Energy

Reaction channels can be selected by gating within Q_3. Then the states of the resonant particle excited in this reaction can be examined by looking at the relative energy between the two decay products c and d. When the excited ejectile decays, the excitation energy, E_x minus the breakup energy threshold and minus the excitation energies of the two decay fragments, E_x(c) and E_x(d) is converted into kinetic energy between the breakup remnants,

$$E_{rel} = E_x - E_{threshold} - E_x(c) - E_x(d) \tag{2.6}$$

This relative kinetic energy will be seen as peaks in a relative energy spectrum corresponding to the different excited states of the resonant particle.

Energy Resolution in E_{rel}

The energy resolution for E_{rel} is significantly better than that of the individual energies E_c and E_d. Many of the random errors which contribute to the Q_3 resolution are correlated for E_{rel} in such a way that considerable cancellation occurs [Rae 84]. A typical decay configuration for these experiments is shown in Figure 2.2. It has been shown [Smi 85] that for detectors placed symmetrically on either side of the beam and at equal distances from the target, the energy resolution for E_{rel} is determined mainly by the accuracy of the measurement of the angle between the two decay fragments, θ_{cd}:

$$dE_{rel} \approx \frac{2\sqrt{M_c M_d E_c E_d}}{M_c + M_d} \sin\theta_{cd} d\theta_{cd} \tag{2.7}$$

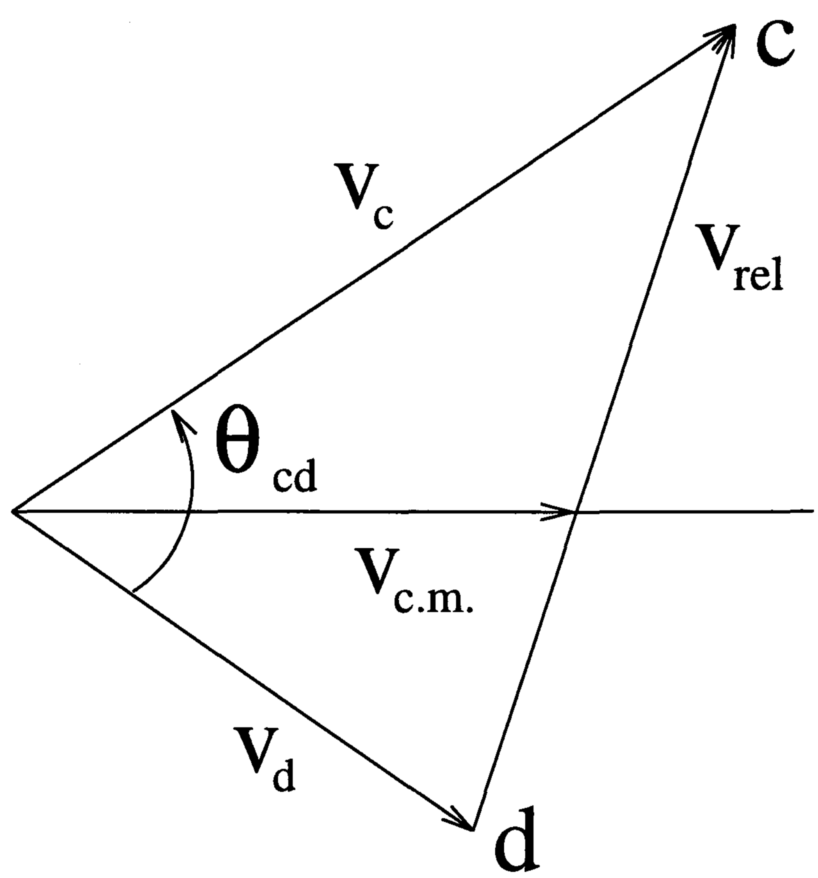

Figure 2.2: *A typical resonant particle decay configuration.*

It should be noted that θ_{cd} is not just the in-plane[1] angle between $\underline{v}_c$ and $\underline{v}_d$, so that a y position measurement is needed. However for large θ_{cd} this out of plane angle enters only in second order [Rae 84].

2.3.3 Phase Space and Angular Distributions

A strong enhancement of the angular distribution was seen in the $^{12}C(0_2^+)+^{12}C(0_2^+)$ decay channel from the Argonne data at θ^*_{cm}=90° [Wuo 92]. Rae, Buck and Merchant have suggested [Rae 92a] that this enhancement represents the signature for a chain state and have further suggested that a similar feature should be present for a ^{28}Si chain state [Rae 92b]. This suggested that during these experiments the detectors should be positioned to maximise the probability for collecting data in this region of phase space. To do this, a set of polar and associated azimuthal angles need to be defined. These angles are shown in Figure 2.3. They are θ^*_{lab} and ϕ^*_{lab}, the laboratory angles of the resonant nucleus before it decays and ψ and χ, the angles of the relative velocity, $\underline{v}_{rel}$ with respect to the beam velocity $\underline{v}_A$. The angles θ^*_{lab} and ϕ^*_{lab} have corresponding centre of mass angles θ^*_{cm} and ϕ^*_{cm}.

The positions and finite sizes of the detectors and their energy thresholds introduce complex multidimensional cuts in θ^*, ϕ^*, ψ and χ space. The program RPS [All 86]

[1]the in-plane angle refers to the horizontal angle between c and d, while the out of plane angle is the vertical angle between c and d.

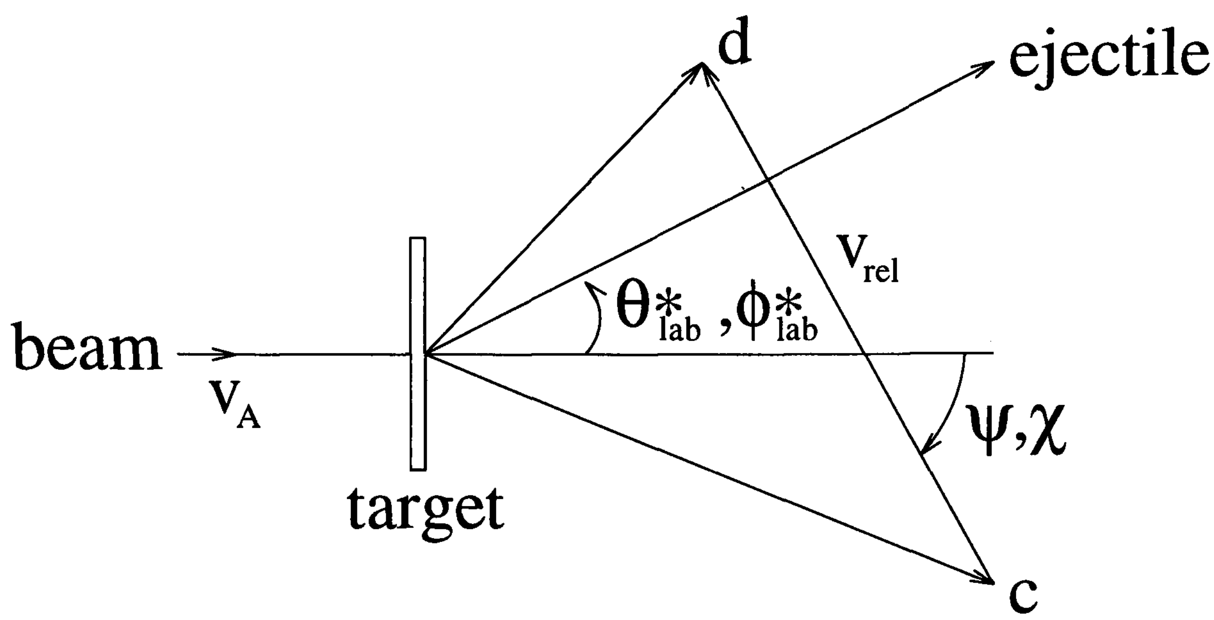

Figure 2.3: *The defining angles for the breakup of the resonant particle.*

was used to calculate the $\theta^*_{c.m.} - \psi$ coverage for different detector settings. It assumes that two of the three nuclei from the quasi-three body final state are detected and steps through the angles $\theta^*_{c.m.}$ and ψ, calculating backwards at each point to the corresponding laboratory angles and energies of these two particles. The resulting parameters are compared with the constraints imposed to determine whether the current $(\theta^*_{c.m.}, \psi)$ pair constitutes a 'hit' (a point accessible with the given detector settings) or a 'miss'. By varying the detector settings the optimum angles of the detectors can be calculated.

2.4 Event Rebuilding

Before the reaction can be treated as quasi-three-body, it is necessary to calculate the kinematic properties, ie. E and $\underline{p}$, for each of the three nuclei in the quasi-three-body final state from information about their constituent alpha particles.

Since two types of events were recorded, two methods were used in event reconstruction. For the first event type, alpha particles were detected in both detectors in coincidence. These events were reconstructed by assuming the decay path for each parent nucleus, this assumption requires that each nucleus decays via a two body decay process into decay products whose excitation energies are known. Several steps were possible in these decay paths before the alpha particle final state was reached and each step needed to be treated individually. The second event type consisted of events where alpha particles had only been detected in one detector, with no hits recorded for the other detector. The method used for these events made no assumptions regarding the decay path. Both of these methods are described below.

2.4.1 Two Body Event Rebuilding

The relative energy described in Section 2.3.2 can be used to rebuild two body events. The two particles resulting from a two body breakup decay will have a relative energy:

$$E_{rel} = \frac{1}{2}\mu(\underline{v}_1 - \underline{v}_2)^2 \tag{2.8}$$

where μ is the reduced mass $\frac{m_1 m_2}{m_1+m_2}$ and $\underline{v}_1$ and $\underline{v}_2$ are the velocities of the two daughter nuclei. When calculated on an event by event basis and histogrammed, peaks are seen corresponding to the energies of the excited states of the parent nucleus above the breakup threshold. In Figure 2.4a the relative energy spectrum is given for $^8\mathrm{Be}_{g.s.}\rightarrow 2\alpha$. The $^8\mathrm{Be}_{g.s.}$ is unbound to alpha decay, with the ground state lying 92 keV above the threshold for breakup into two alpha particles. Events corresponding to $^8\mathrm{Be}_{g.s.}\rightarrow 2\alpha$ lie within the peak at 92 keV and can be selected by gating. Conservation of momentum can now be used to reconstruct the kinematic properties of the parent nucleus. Its momentum will be:

$$\underline{p} = \underline{p}_1 + \underline{p}_2 \tag{2.9}$$

where $\underline{p}_1$ and $\underline{p}_1$ are the momenta of the decay fragments. The kinematic energy will be

$$E = \frac{|\underline{p}|^2}{2(m_1 + m_2)}. \tag{2.10}$$

This method can also be used to reconstruct more complex decays such as $^{12}\mathrm{C}(0_2^+)\rightarrow$ $^8\mathrm{Be}_{g.s.}+\alpha \rightarrow 3\alpha$. The reconstruction is performed in two stages. Firstly the $^8\mathrm{Be}_{g.s.}$ is rebuilt as above from its two alpha decay products. The relative energy between all pairs is calculated, if any pair yields the correct relative energy then the $^8\mathrm{Be}_{g.s.}$ is assumed. The relative energy is then calculated between the $^8\mathrm{Be}_{g.s.}$ and the remaining alpha particle. In ^{12}C there are states lying at 7.65 MeV and 9.64 MeV, these are 284 keV and 2.27 MeV above the breakup threshold into $^8\mathrm{Be}+\alpha$ at 7.37 MeV. In Figure 2.4b the relative energy spectrum is shown for $^{12}\mathrm{C}^*\rightarrow{}^8\mathrm{Be}_{g.s.}+\alpha$. These two excited states in ^{12}C are clearly identifiable. The kinematic properties of the ^{12}C can now be calculated from equations 2.9 and 2.10 as before.

2.4.2 Q-value Reconstruction

For a final state containing n alpha particles, the assumption can be made that they all result from the decay of the same excited parent nucleus. Then, irrespective of

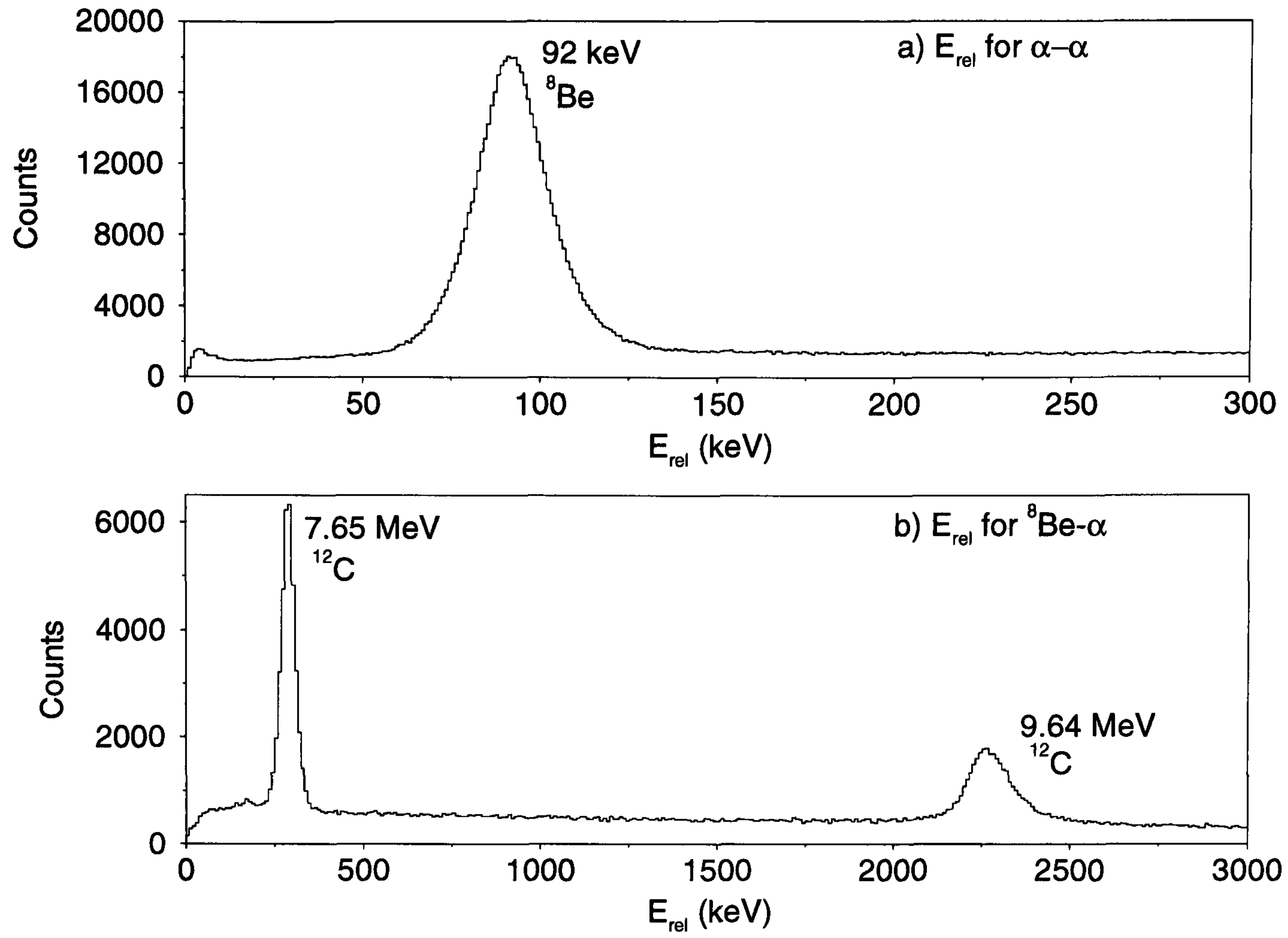

Figure 2.4: *The nuclei* a) ^8Be *and* b) $^{12}C(0_2^+)$ *rebuilt from their decay products using the two body method described in Section 2.4.1.*

the decay path, the excitation of the parent nucleus will be:

$$E_x = \sum_{i=1}^{n} E_{\alpha i} - \frac{1}{2nm_\alpha} \left| \sum_{i=1}^{n} \underline{p}_{\alpha i} \right|^2 + threshold \tag{2.11}$$

where the first term is the sum of the kinetic energies of the final state alpha particles, the second term is the energy of the parent nucleus calculated from the summed momenta of the final state nuclei and the third term is the threshold energy for breakup into n alpha particles.

This method has been used to re-construct ^{8}Be and ^{12}C* nuclei, see Figure 2.5. These two spectra can be compared with those produced using the two body method described in Section 2.4.1; the ^{8}Be spectra are identical. There are two differences between the ^{12}C spectra. Firstly, the threshold is now ^{12}C$^*\rightarrow 3\alpha$, resulting in a 92 keV increase in the relative energy. Secondly, the background is significantly higher, particularly for the 9.6 MeV state, when using the Q-value method. This is because the additional ^{8}Be gate is not applied. For singles events this was not a significant effect.

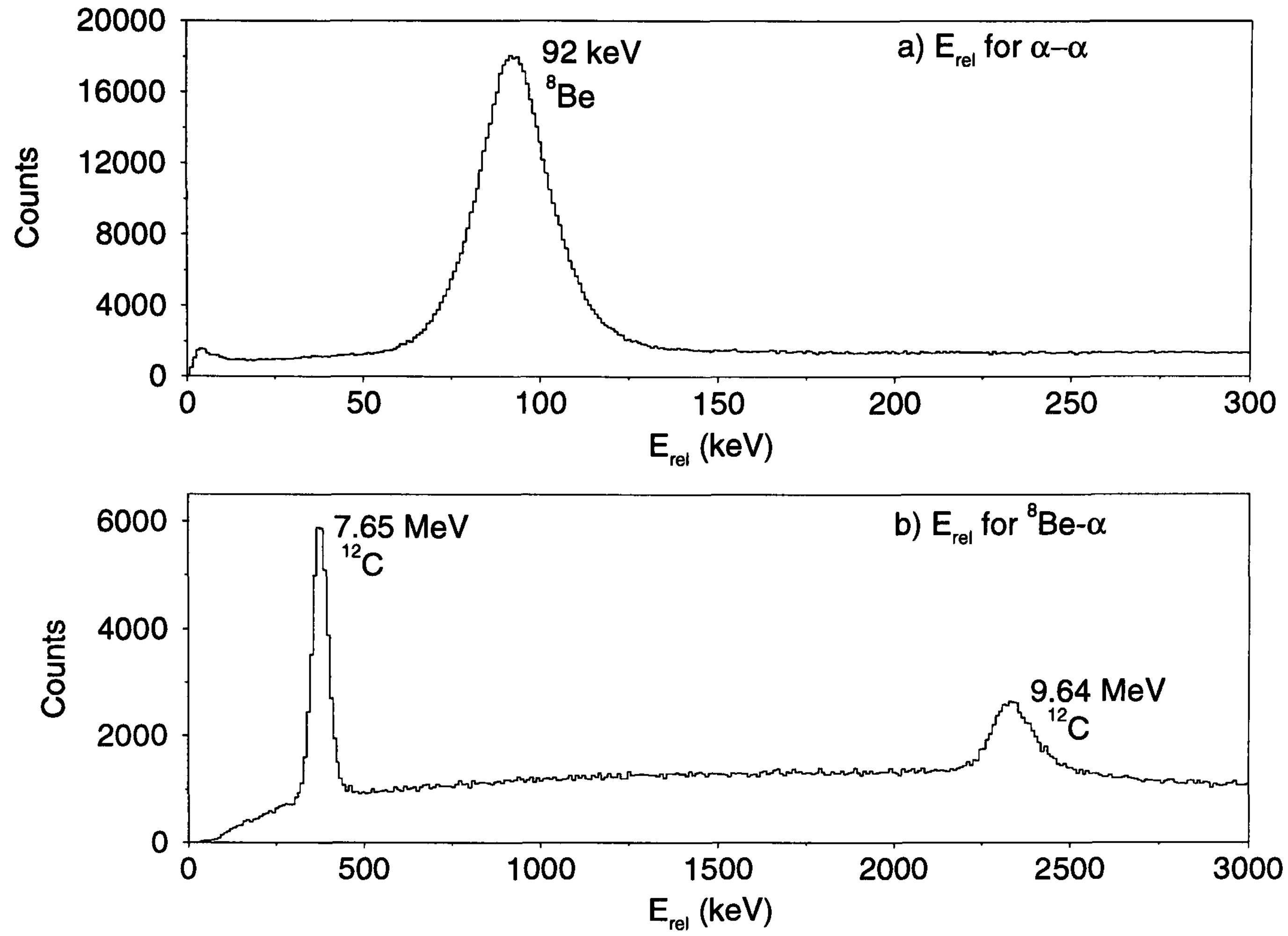

Figure 2.5: a) ^{8}Be *and* b) $^{12}C(0_2^+)$ *rebuilt from their decay products using the Q-value reconstruction method described in Section 2.4.2.*

2.4.3 Excitation Energy of the Undetected Nucleus for Singles Events

For singles events, where only the particle b is detected, it is still possible to calculate the excitation energy of the undetected resonant particle using two body kinematics. Conservation of momentum and conservation of energy gives the Q-value for the reaction:

$$Q = \frac{M_b + M_{B^*}}{M_{B^*}} E_b - \frac{M_{B^*} - M_A}{M_{B^*}} E_A - \frac{2\sqrt{M_A M_{B^*} E_A E_b}\cos\xi}{M_{B^*}} \tag{2.12}$$

where ξ is the angle of the trajectory of b with respect to the beam axis. The excitation energy of the resonant particle can now be calculated from:

$$Q = -E_x(b) - E_x(B^*) + Q_{gg}. \tag{2.13}$$

Q_{gg} is the Q-value when both of the nuclei are in their ground states.

By using this method all reactions of the form b+B* can be examined. In particular the ground state and first excited states of the resonant particle may be observed. These states are not alpha unstable and hence it is not possible to identify them in a coincidence event. The high background swamps higher lying excited states.

2.5 Yields and Differential Cross-Sections

An essential part of this experimental work was to measure the differential cross-section for the reaction $^{16}O+^{12}C\rightarrow^{12}C(0_2^+)+^{16}O^*_{chain}$ as a function of energy. If the chain state is being seen, then a resonance should be observed in the cross-section with a predicted width of approximately 4 MeV. This resonance is calculated to lie in the energy region around E_x=60 MeV.

In the ^{12}C-^{12}C scattering reaction there have been recent reports of resonances seen in decay channels other than $^{12}C(0_2^+)$-$^{12}C(0_2^+)$ at similar centre of mass energies to the six-alpha chain state [Ali 94, Cha 95a, Mir 94]. This might also be expected to be the case for ^{28}Si since band crossing between different configurations are predicted, and would be seen as resonances in the yield of other channels.

As a preliminary to calculating the cross-section, the yield in all channels can be measured.

$$\text{Yield} = \frac{\text{Number of Counts}}{\text{Integrated Beam Current } (\times 10^{-9} \text{ Coulombs})} \tag{2.14}$$

The yield in each decay channel is measured by integrating the peaks seen in the Q_3 spectrum. From the yield, the cross-section is given by

$$\frac{d\sigma}{d\Omega} = 266.0 \times \text{Yield} \times \frac{A_t.C_s}{\Delta\Omega_{c.m.}.T_t} \times \frac{1}{\text{eff}_1.\text{eff}_2} \tag{2.15}$$

where C_s= charge state of the beam at the Faraday cup

T_t= target thickness in μgm/cm^2

A_t= atomic weight of the target in gms

and $\Delta\Omega_{c.m.}$= detector solid angle in the centre of mass in msr.

Eff_1 and eff_2 are the efficiencies for detecting the alpha particles comprising the two nuclei detected. The calculation of these two terms is covered below in, Section 2.5.2. Transformation of the solid angle covered by the detectors into the centre of mass frame for non-relativistic reactions is obtained using the relation [Pas 75]

$$\frac{d\Omega_{cm}}{d\Omega_L} = \left\{1 + \frac{\cos\theta_L}{\sqrt{1-\gamma^2\sin^2\theta_L}}\right\} \times \frac{\sin\theta_{cm}}{\sin\theta_L} \tag{2.16}$$

with

$$\gamma = \left\{\frac{M_a M_b}{M_A M_{B^*}} \frac{1}{\left[1 + \left(1 + \frac{M_a}{M_A}\right) \times \frac{Q}{E}\right]}\right\}^{\frac{1}{2}} \tag{2.17}$$

The centre of mass angle of detection is related to the angle of observation by

$$\theta_{cm} = \theta_L + \sin^{-1}(\gamma\sin\theta_L) \tag{2.18}$$

2.5.1 Errors Introduced into the Cross-Section

There will be both systematic and statistical error contributions to the error in the cross-section. Of these, systematic contributions will come from uncertainties in the target thickness, detector efficiency, detector distances from the target and the detector angles. Statistical errors will arise from uncertainties in the number of counts in the peak and in the background.
Due to the low cross-sections of the channels examined in this thesis, the largest error is contributed from the uncertainties in the number of counts in the peak and the other errors can be neglected. Also, for weak states, or states with a large background, then the errors can be bigger than the statistical errors. These errors are mainly introduced by the procedure used to fit the peak and the background. In these experiments the error in the cross-section was of the order of 10% -20% .

2.5.2 Detector Efficiency

In general, when a nucleus breaks up isotropically, there will be an efficiency associated with the detection of the breakup fragments. This efficiency will depend on the direction of the original nucleus with respect to the detector setup and the opening angle associated with the breakup cone. This is shown schematically in Figure 2.6. The breakup cone results from kinematic focussing and confines the breakup fragments kinematically. The opening angle is the maximum angle through which the fragments can be separated and is a characteristic of each reaction, depending on the energy released by the reaction, equation 2.6 and the energy of the decaying nucleus.
The detection efficiency must be corrected for in the differential cross-section. There are two ways to do this. Firstly the whole reaction can be modelled and the overall efficiency can be calculated and folded in to the cross-section calculation. This method involves accurate modelling of each breakup state and its associated angular distributions and is prone to error. Alternatively, for J=0 states, it is a simple matter to correct for the detection efficiency on an event by event basis. A characteristic of J=0 states is that they break up isotropically in the centre of mass frame, so that there is an equal probability for detection of the decay fragments within all solid angles of equal area in the centre of mass. The breakup can be modelled using a Monte-Carlo routine, to produce a representative set of breakups. For each set of breakups the parent nucleus is given a specified energy and would be incident on a certain point on the detector, if it did not breakup. The efficiency can be

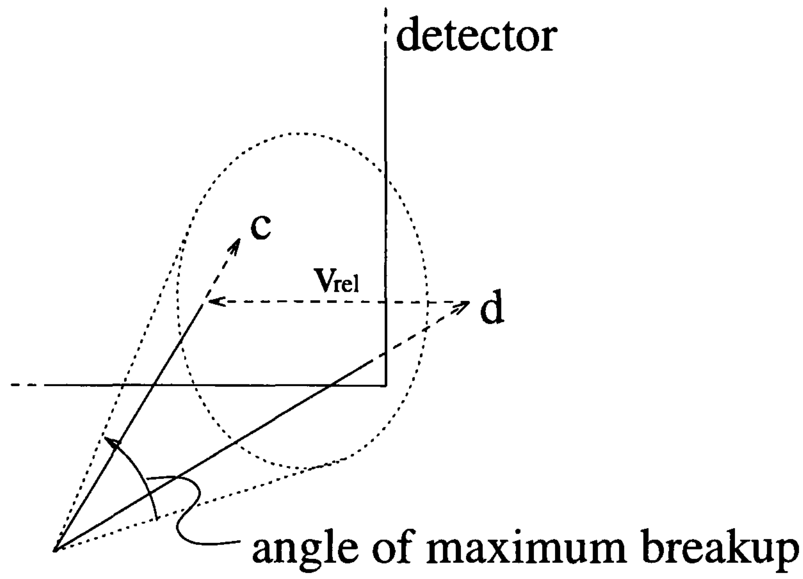

Figure 2.6: *A diagram showing a typical two-body breakup reaction with relation to a detector. The reason for efficiency variations across the detector can clearly be seen.*

calculated from the number of times that all of the breakup fragments are detected, versus the number of times when one or more miss the detector. The energy of the parent nucleus and its position can be varied to calculate the efficiency of the detector across the whole surface, as a function of energy of the incoming nucleus, before it breaks up. When analysing the data, the originating nucleus is rebuilt and the efficiency for its detection at that position on the detector can be calculated and folded in. No additional corrections are needed later in the efficiency formula. The details and implementation of the efficiency codes used during this analysis are covered in Appendix A.

2.6 Summary

This chapter has covered the kinematic topics necessary to deal with three-body events. Although the ^{28}Si is expected to decay to a final state containing seven alpha particles, three-body techniques can be used, because the decay is sequential and proceeds via a series of two-body decays through relatively long lived states in alpha unstable nuclei. These decays can then be described by two variables, Q_3, the three body Q-value, and E_{rel}, the relative energy between the two decay products from the resonant nucleus. Two methods were described for re-building and examining the event, depending on whether particles were detected in only one detector or in both detectors in coincidence. The errors in Q_3 were found to arise mainly through uncertainties in the measurement of the energies of the final state alpha particles. For E_{rel}, the imprecision of the measurement of the in-plane angles provides the most significant contribution to the errors. The main signature of a ^{28}Si

chain state is expected to be an enhancement of the yield in the ^{12}C(0_2^+)-^{16}O$_{chain}$ decay channel.

Chapter 3

Experimental Setup

This chapter contains an overview of the experimental apparatus used in the acquisition of the data presented in this thesis. It begins with a brief overview of the general laboratory facilities. Much of this section has been covered in detail elsewhere, so that only the pertinent features are described, with references given to more detailed works. In the second half, a more thorough description is given of the experimental apparatus specific to these experiments.

3.1 Introduction

Three experiments have been performed, using the $^{16}O+^{12}C$ reaction to explore the excitation region between 54.5 MeV and 68.2 MeV in ^{28}Si. Two exploratory experiments were performed at the Nuclear Structure Facility (NSF), Daresbury, during January and August 1992. The first of these experiments took place over three days and covered the laboratory energies 92 MeV, 99 MeV and 106 MeV. The second experiment ran for 5 days and covered 7 energies between 88 MeV and 112 MeV. During the analysis of these two experiments an enhancement of the seven-alpha yield was measured at E_x=59.5 MeV, however the statistics were low. Therefore it was thought worthwhile to perform a third experiment, not only to improve the statistics, but also to increase upwards the energy region covered and to improve the energy resolution. Due to the closure of the NSF, in March 1993, this final experiment was performed at the Australian National University (ANU), Canberra. It covered 13 energies from 88 MeV to 120 MeV in the laboratory frame. The move to the ANU necessitated some changes to the setup and calibration of the detectors, in addition minor changes were made to the electronics. However

Date	Duration (Days)	Location	Beam Energies (MeV)	Target Thickness ($\mu g/cm^2$)	Detector Thickness (μm)	Detector Distances (cm)
February 1992	3	NSF	92, 99, 103	200	1000, 1000	12.0, 12.0
August 1992	5	NSF	88, 96, 99 101, 103, 107 112	200	1000, 500	12.0, 12.0
October 1993	7	ANU	88, 91, 95 99, 101, 103 105, 108, 110 115, 118, 120	90	1000, 1000	12.8, 12.7

Table 3.1: *A summary of the experiments carried out.*

in general it will be possible to describe the experiments together, with differences noted where they occurred. An overview of the details for each experiment is given in Table 3.1.

3.2 Ion Sources and Beams

The only ion species used during these experiments was ^{16}O, which was used for both the calibration beam and the reaction beam. At the NSF, the ions were produced by a Middleton source [Mid 74], while at the ANU, a SNICS (Source of Negative Ions by Cesium Sputtering) source [Cas 78] was utilised. These two sources work on similar principles. Positively ionised cesium vapour is sputtered onto the solid surface of a target containing the species to be accelerated. The sputtering releases negatively charged ions from the surface of the target in a process similar to surface ionisation [Alt 81]. These ions are electrostatically accelerated and extracted.

Sputter sources have several advantages over their predecessors. For charged particle experiments the most important of these is that the ions can be produced with fairly high intensities and that the emittance and energy spread of the extracted beam are low.

During these experiments intensities of between 5 pnA and 10 pnA (particle nA) were employed for the calibration beam and between 40 pnA and 200 pnA for the reaction beam.

3.3 Accelerators

Both the NSF and the ANU employ Tandem Van Der Graff accelerators to accelerate the ions beams. The NSF Tandem was custom built and was capable of reaching 20 MV on the central terminal [Ait 74]. The ANU accelerator employs an "off the shelf" design by NEC and is able to operate with a maximum terminal voltage of 16 MV [Oph 74]. Both accelerators have high transmission efficiencies and produce beams of high stability and high energy accuracy.

Negative ions from the source are accelerated towards a stripping foil located at the central terminal. Here some of the electrons are stripped from the ions, leaving them with a positive charge. The ions are re-accelerated and extracted at the foot of the accelerator. The final energy is

$$E = (1 + C_s)T_V \tag{3.1}$$

where C_s is the charge state of the beam after stripping and T_V is the terminal voltage. Charge states of between 5^+ and 7^+ were used, producing ^{16}O ions with energies of 35 MeV (NSF) and 32 MeV (ANU) for the calibration beam and between 88 MeV and 120 MeV for the reaction beam.

3.4 Scattering Chamber

The scattering chamber provided a large evacuated volume within which the targets and detectors were mounted. The detectors were mounted on two independently movable arms, whose angles could be varied under computer control from outside the chamber.

These arms revolved around a target apparatus mounted at the centre of the chamber. Both the NSF and ANU chambers allowed the user to interchange targets while the chamber remained under vacuum, although different methods were used to accomplish this. At the NSF the targets were held on a ladder mounted on the base of the chamber, which could be raised or lowered in order to select the required target. In contrast to this, the target mechanism at the ANU, consisted of a wheel suspended from the lid of the chamber into which several targets could be mounted. Targets could be removed through a port on the lid of the chamber while the chamber remained under vacuum. Unfortunately, this system was a lot larger, with an 8cm disk protruded from the central column of the target mechanism, preventing the detectors from being placed as close to the target as was possible during the NSF experiments.

The beam entered the chamber through a port on one side. In order to maximise the energy and angular resolution, it was important that the beam divergence was minimised and that the beam was well focussed at the target. This was achieved by using a collimation system between the entry port and the target. It consisted of 4 mm$\times$4 mm collimation slits and 6 mm$\times$6 mm anti-scatter slits mounted at 225 mm and 125 mm from the target respectively. During beam steering, when the beam is first guided down the beam pipe from the ion source to the target, these slits provided feedback on the position of the beam. By minimising the current on the slits, the beam could be made to pass centrally down the beam line.

Also during beam steering a 1.5 mm$\times$1.5 mm hole was placed in the target holder. The fraction of the beam passing through this hole was measured by a Faraday cup at the end of the beam pipe. The current on this cup was maximised. The final beam spot size was thought to be of the order of 1 mm$\times$1 mm with little beam divergence.

The vacuum pumps used at the NSF and the ANU had quite different properties. In particular the pumps at the ANU took longer to pump down and could not be used again for a significant time. This difference necessitated some changes to the calibration procedure at the ANU. At the NSF, vacuum was achieved by using a rotary pump as the backing pump and a turbo-molecular pump as a final stage pump. These gave a pump down time of approximately 30 minutes and could be repeated indefinitely. In contrast, the pumps at the ANU were a carbon vane pump from atmospheric pressure and later a sorbation pump and a cryo-pump. Using this system the evacuation time was several hours. In addition, each evacuation filled the pores in the sorbant, thus requiring that the sorbation pump be degassed after each pump-down. The degassing process took 6 hours and considerably slowed down the process of repeated evacuation. The result of this was that the scattering chamber at the ANU was not re-opened once it had been evacuated. To get around this a new calibration method was devised, it is described in Section 4.4.3.

3.5 Targets

Two sets of targets were loaded for each experiment. First, a calibration set was mounted, followed by the reaction foils. All foils were self supporting and mounted on a frame so that they presented a 1 cm diameter circular area to the beam.

The calibration foils consisted of a ^{197}Au target and a natural carbon target. These were 200 μg/cm^2 and 90 μg/cm^2 respectively. At the ANU these were supplemented by a 150 μg/cm^2 ^{27}Al target.

The reaction targets consisted of a range of natural carbon foils varying in thickness from 90 μg/cm^2 up to 200 μg/cm^2. The final foil thickness was chosen as a trade off between energy loss and straggling in the target, and hence a degradation in detected resolution, versus intensity of the scattered beam. In the first two experiments a 200 μg/cm^2 target was chosen, while in the last experiment this was reduced to 90 μg/cm^2. Energy resolution in the first experiment was 190 keV, while in the second experiment this deteriorated to 260 keV, due mainly to poor detectors rather than the thickness of the targets. In the final experiment, at the ANU, the resolution was again improved to 190 keV.

Two targets were common to each target load. These were a blank frame and a 1.5 mm$\times$1.5 mm hole. They were used during beam steering.

3.6 Detectors

From Chapter 2 it has been seen that the detectors for these experiments must have certain properties. These are:

- a large solid angle coverage,
- good horizontal resolution and medium out of plane resolution,
- the ability to detect multi-particle events.

Additionally, particle identification would be useful. These criteria were most obviously met by the position sensitive strip detector (PSSD). The PSSD's used consisted of 16 horizontal resistive strips etched on to a 5 cm by 5 cm silicon wafer. The vertical position is given by the strip number. Although a single strip cannot detect multiple events, each strip works independantly, giving the possibility of multi-particle detection. A large number of channels are needed to obtain a full readout from the detector. Two channels are needed for each strip for the position / energy signal, plus one timing signal. This amounts to 48 channels per detector.
The PSSD cannot provide particle identification and so two options were examined to allow identification, or to remove the need for it, by removing particles heavier than alpha particles. The most usual way to obtain particle identification is to place a thin ΔE detector in front of the strip detector. The particle type can now be calculated using an energy loss formula. ΔE detectors are normally gas or thin silicon detectors. The silicon detectors are usually 1 cm$\times$1 cm, and thus were rejected because of their small size, while the use of a gas detector would have precluded multi-particle event detection since they only have a single detecting volume. Using two strip detectors placed one in front of the other was also considered. This idea was rejected since the thinnest PSSD is 300 μm, thick enough to stop most incident nuclei of all types within the detector.
The idea of selectively stopping the heavy ions was also examined. This is commonly achieved by placing a thin mylar foil between the target and the detector. The longer range of the alpha particles within the mylar at a given energy means that these particles can pass through with a small energy loss, while the heavier nuclei are stopped. Unfortunately, calculations showed that the energy of the alpha particles would have given them a similar range within the mylar to the heavy ions, ruling out this method.
In the end, no particle identification method was used. It was found that if the multiplicity gates (that is the number of hits required within each detector) were

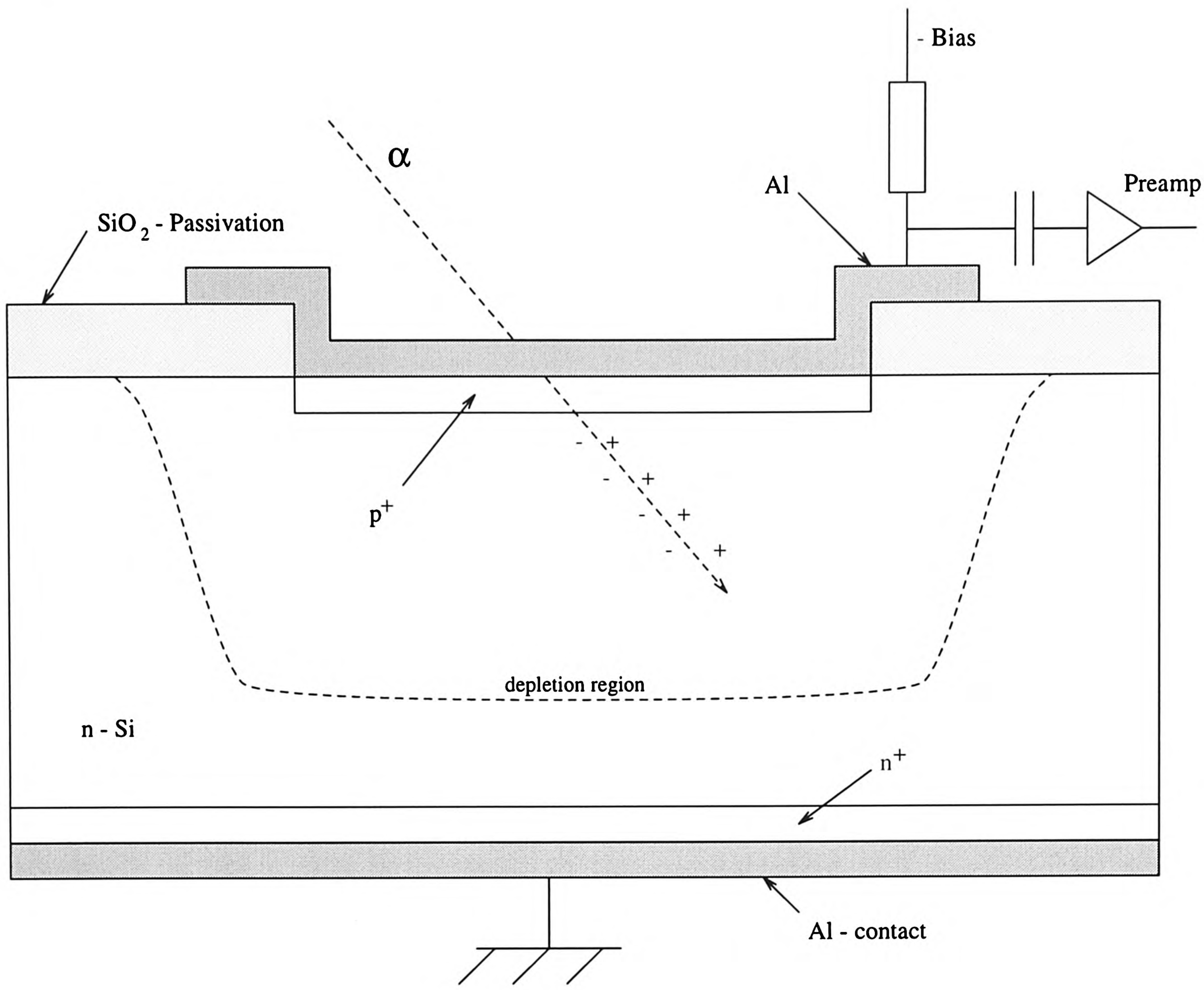

Figure 3.1: *A schematic diagram showing one strip from a position sensitive strip detector.*

set high enough, then the background was reduced to a negligible amount.

3.6.1 Detector Design

The PSSD's were designed by Micron Semiconductors for Edinburgh University [Dav 90] using photolithographic techniques developed by Kemmer [Kem 84]. They consist of 16 horizontal 3 mm wide strips etched onto a 5 cm by 5 cm silicon wafer, with 0.1 mm gaps between strips. The effect of the inter-strip gaps on the detector efficiency and background contributions is discussed in Appendix B.

Calculations performed prior to the experiments showed that the maximum energy expected for the alpha particles of interest would be 30 MeV. To stop these, the detectors needed to be at least 300 μm thick. In practice 1 mm thick detectors were used.

The PSSD is essentially a reverse biased p-n junction diode, Figure 3.1. By applying a negative voltage, referred to as the bias voltage, to the p$^+$ side of the junction, a depletion region can be formed within the detector. Within the depletion region a

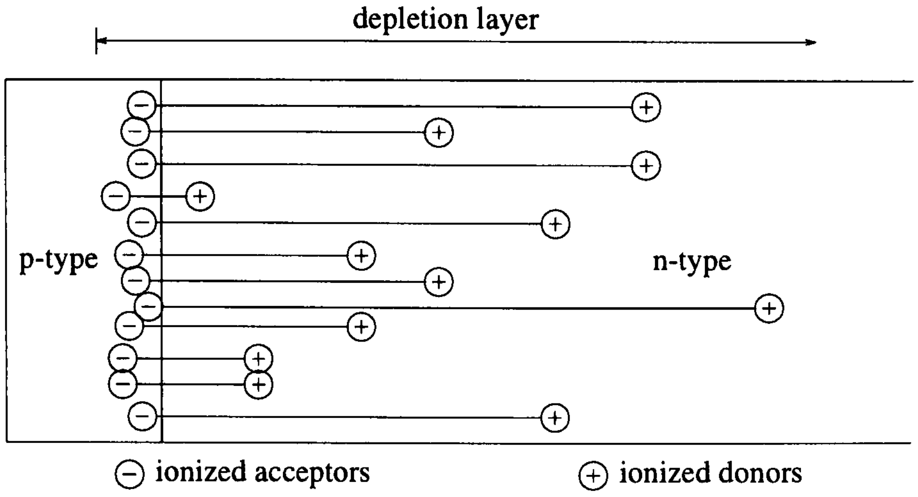

Figure 3.2: *Charge distribution in the depletion layer of a reverse-biased $p - n$ junction.*

charge imbalance exists caused by the migration of electrons into the p-type material. This diffusion leaves behind positive donor impurity sites within the n-type material. The combined effect is to build up a net negative space charge on the p side and a positive space charge on the n side of the junction. If the concentration of the acceptors on the n side is the same as the concentration of donors on the p side then the depletion region will extend equal distances on both sides. However, the thickness of the depletion region can be maximised by heavily doping the p-type material, while the other side consists of high purity silicon that is only mildly n-type [Dea 67]. In this way the detector can be fully depleted, so that the depletion region extends through the entire depth of the detector, see Figure 3.2. Also, for a large difference in the doping levels the heavily doped p^+ layer can be made very thin, providing a thin entrance window.

In order to create an electric field large enough to achieve an efficient collection of the charge carriers, a voltage of several hundred volts must be applied as a bias voltage. Even in the absence of ionising radiation some steady state leakage current will occur. Random fluctuations in this leakage current will tend to obscure the small signal currents following an ionising event and it is therefore important to reduce the leakage current to a minimum. In the PSSD this is achieved by using a blocking contact. The blocking contact, n^+, can be seen as the lower contact on the detector in Figure 3.1. When charge carriers are initially removed by the application of the electric field, the blocking contact prevents their replacement at the opposite electrode, and their overall concentration will drop after the application of the electric field. The leakage current is thus reduced to a sufficiently low level that the current pulse from the ionising event can be detected. With the bulk leakage reduced to a negligible level, leakage across the surface of the detector is often more

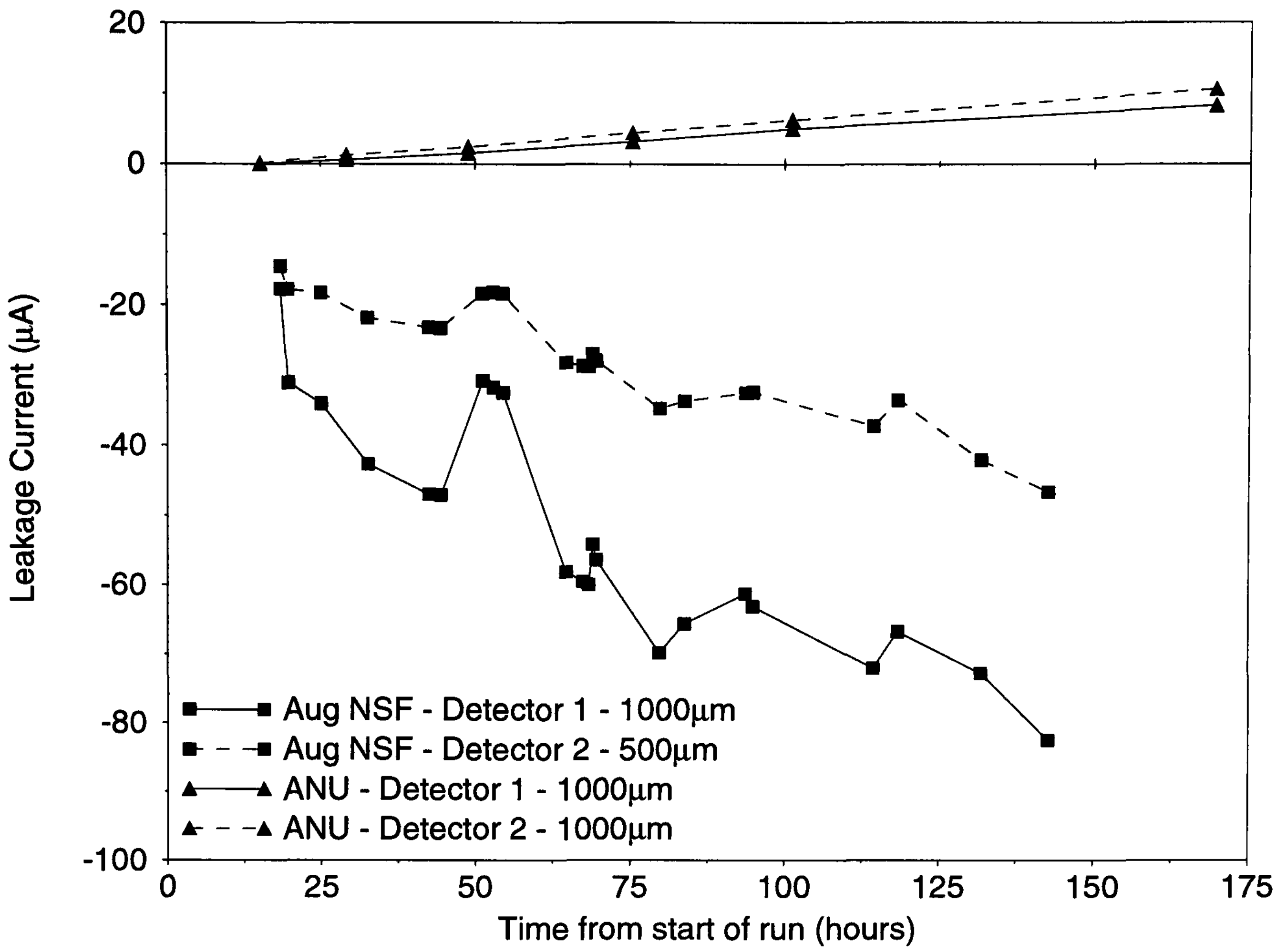

Figure 3.3: *A comparison of the change in the leakage current with time between the second experiment at the NSF and ANU experiment.*

significant. This is discussed further in the next section.

3.6.2 Detector Bias

To operate a p-n junction detector in reverse bias mode, the p^+ layer must be held negative with respect to the n^+ layer. During experiments at the NSF this was achieved using the method shown in Figure 3.1. The pre-amplifiers have an input which allows the bias to be applied along the same cable that carries the signal from the detector. The bias is supplied through a 1 MΩ bias resistor to one end of each strip from a single bias supply for each detector. The bias resistor is usually made as large as possible to reduce noise. However, any leakage current drawn by the detector must also flow through this resistor. In this case, a substantial voltage drop can be registered across the resistor, and the voltage applied to the detector is reduced. The variation of the leakage current during the second experiment at the NSF is shown in Figure 3.3. The magnitude of the leakage current was seen to fall if the beam was switched off, indicating that the largest contributor was leakage across the surface of the detector.

The bias supply automatically compensated for the voltage drop across the bias resistor by increasing the bias voltage. However there were worries that the contribution to the leakage current from the in plane (central) strips may be greater than for the outer strips. This would have caused uneven biasing and hence a greatly reduced depletion thickness for the centre strips.

In the last experiment, at the ANU, the detectors were changed. The new detectors were designed specifically for us by Hamamatsu. These detectors employ an additional passivation layer over the front of the detector. This reduced the leakage current significantly, as can be seen in Figure 3.3. The bias method was also changed. Instead of applying a negative bias voltage to the p^+ layer of each strip individually, a positive bias voltage was applied through a 100 kΩ resistor to the entire back face. This is thought to have resulted in a more even biasing, since the smaller resistor led to a smaller drop in the bias voltage as the leakage current increased, without an increase in noise, which was significant for our application.

3.6.3 Detector Geometry

Prior to the experiments, the program RPS [All 85] was used to determine the optimum detector distances and angles, see Section 2.3.3. The simulation was run for each of the intended energy steps and for ^{16}O excited energies of 16.95 MeV, 20.0 MeV and 22.0 MeV. A typical output is shown in Figure 3.4 at the laboratory energy of 92 MeV and with a ^{16}O excitation energy of 16.95 MeV. The Argonne data showed a strong enhancement of the angular distribution at θ^*_{cm}=90° [Wuo 92] and it is thought that a similar enhancement will also be present for a seven-alpha chain in ^{28}Si. The area of phase space around θ^*_{cm}=90° is denoted by dashes on the $\theta^*_{c.m.} - \psi$ phase space plot (left hand plot in Figure 3.4). The laboratory angles that this area of phase space corresponds to are marked on the right hand plot. From these plots it was found that the detectors should be placed symmetrically one on either side of the beam at a distance of 12 cm from the target and at angles of 30.5° to the beam line.

3.7 Electronics

The electronics used in these experiments can be conveniently split into several parts according to the function performed. The signals from each end of each strip are processed separately, first to increase their amplitude and then to convert them to a digital form so that they can be stored. The signals are only stored if the whole event meets certain user defined criteria. These criteria are checked using logic electronics.

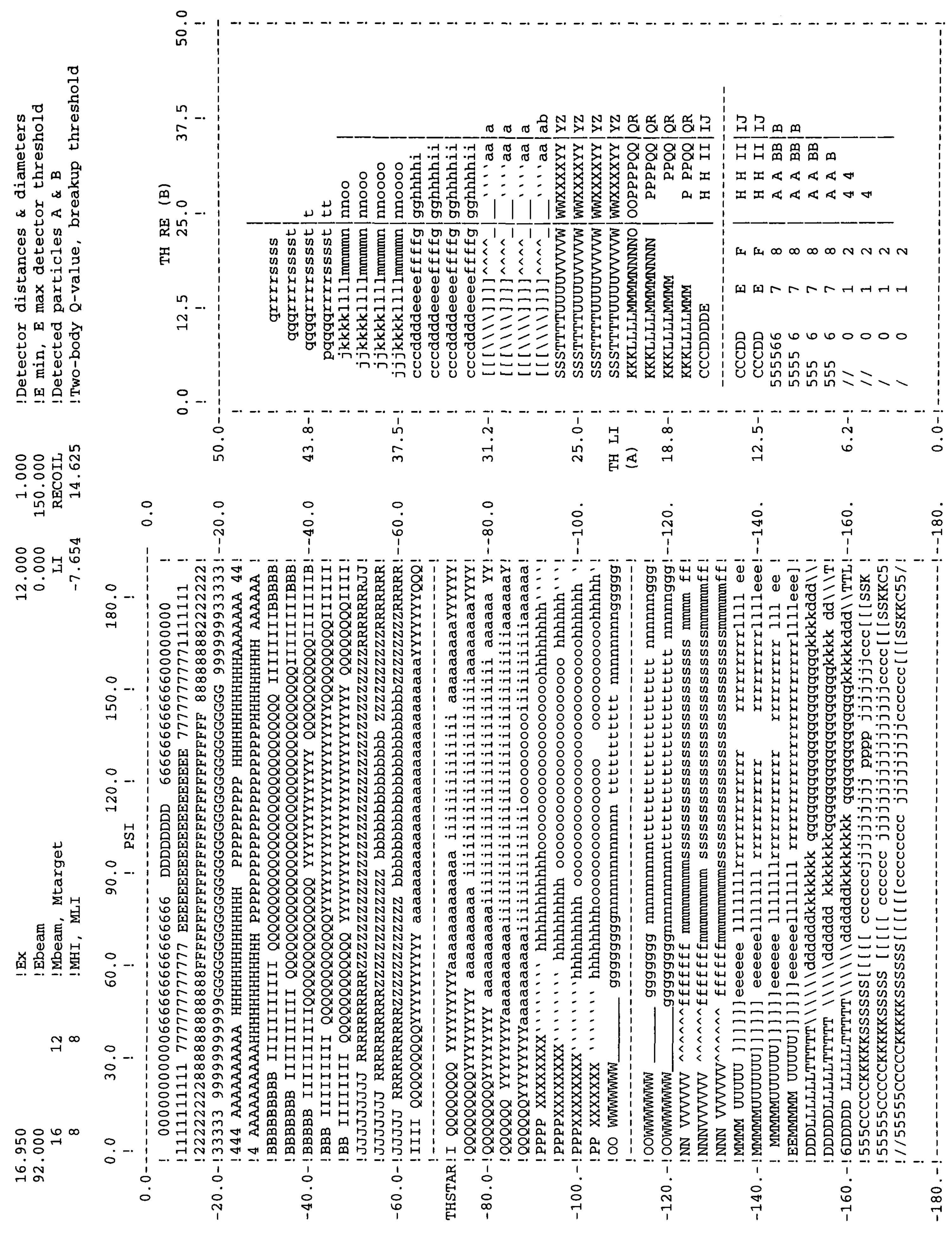

Figure 3.4: *An output from the program RPS at a laboratory energy of 92 MeV and a* ^{16}O *excitation energy of 16.95 MeV. The right hand graph plots the angle of one of the detected nuclei against the angle of the other, in the laboratory, for the regions denoted in the THSTAR-PSI plot (left hand graph). The symbols correspond to the same areas in each plot and are there to guide the eye. In the THLI(A)-THRE(B) plot, the dashed lines denote the detector coverage in the laboratory. In the THSTAR-PSI plot, they denote the THSTAR region of interest.*

When they are met, a signal is sent to an event manager, which controls the event processing. A GEC computer is used to read the events from the event manager and store them to tape. The GEC also allows all of the parameters within the event manager modules to be controlled. Additionally, a simple on-line analysis of the experiment can be made using this computer system. In Figure 3.5 an overview is given of the analogue and digital electronics, while the event manager is shown in Figure 3.8. The different sections of the electronics are covered separately below.

3.7.1 Analogue Electronics

The outputs from the detectors were taken out of the chamber using a connex feed through. Immediately outside the chamber each signal was amplified using a charge sensitive pre-amplifier, before being fed to the control room. Here the signals were re-amplified and then digitised. This section covers each of the modules in this process.

Pre-Amplification

The pre-amplifiers are placed as near as possible to the detectors to minimise capacitive loading of the detectors by long interconnecting cables. When using solid state detectors the capacitance of the detectors may change with the operating parameters, such as temperature and bias voltage. Since the detector is essentially a charge producing device, the height of the voltage pulse from an event will appear as a function of the capacitance of the detector. This is obviously undesirable. To avoid this situation, a charge sensitive pre-amplifier is used [Gil 70]. The charge sensitive pre-amplifier produces a tail pulse at the output, whose height is proportional to the total integrated charge of the pulse.

The pre-amplifier has two further inputs in addition to the signal input. The first of these, used to supply bias to the detector, has been described earlier in Section 3.6.2. The second input provides a test input for the system. The most significant sources of noise occur at this point in the electronics; noise introduced here, where the signal is smallest, will be amplified with the signal, whereas noise introduced after amplification is normally much smaller than the signal. The test input allows signals from a pulser to be passed through the electronics to measure the inherent electronic noise width. It also provides a simple check of the overall function of the system prior to an experiment.

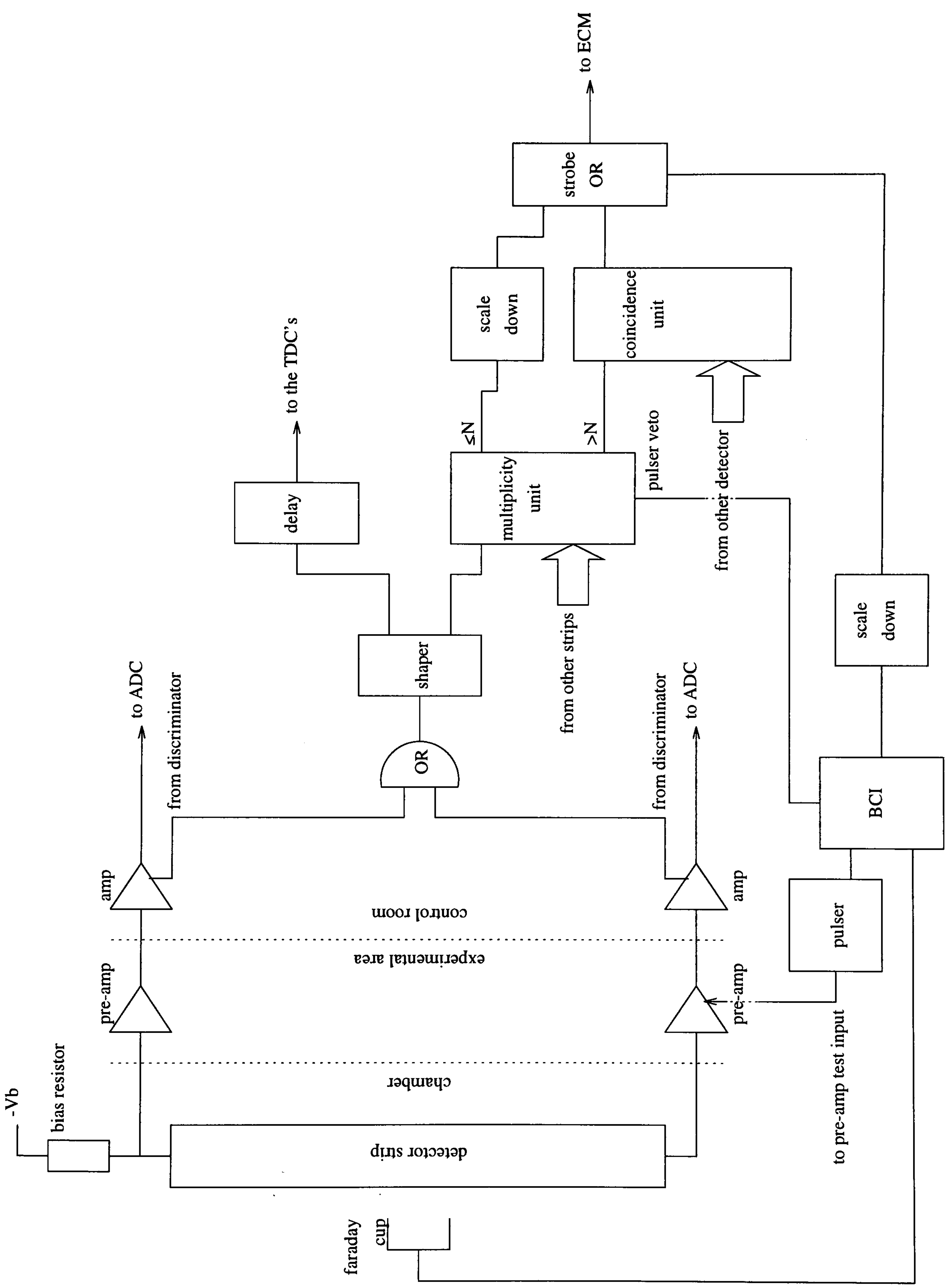

Figure 3.5: *An overview of the analogue and logic electronics.*

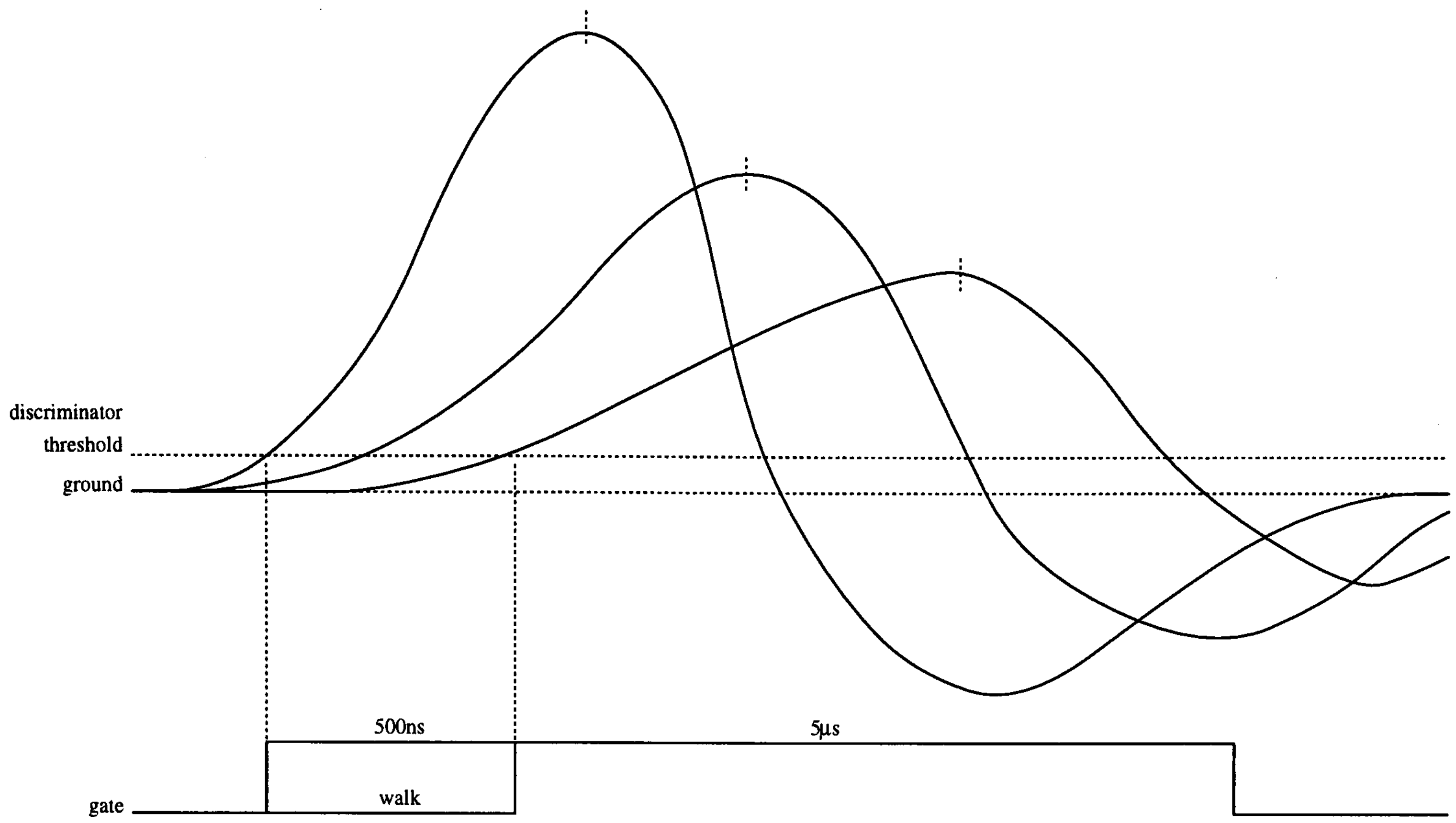

Figure 3.6: *The relationship between the ADC conversion window and the amplified signals.*

Amplification

The amplifier performs two functions. Firstly, it amplifies the tail pulse signals from the pre-amplifier and secondly, it provides pulse shaping. Several different pulse types are produced by the amplifiers, of which two were used during these experiments. A bipolar output was used as input to the Analogue to Digital Converter. The peak height of these pulses is proportional to the charge deposited in the detector. A second signal was taken from a discriminator within the amplifier. This discriminator produced an output (fast NIM) every time the leading edge of a signal pulse was detected, Figure 3.6. The discriminator pulses from each strip were used as inputs to the logic electronics.

The Analogue to Digital Converter

Standard Silena 4418 Analogue to Digital Converters (ADC's) were used to convert the peak height of the analogue signals from the amplifiers into a form that could be stored. The Silena 4418 takes eight input channels and processes them using a single ADC chip. The peak of the signal from the amplifiers is detected and this value is held using a sample and hold circuit. Then for each channel, the ADC uses a successive approximation technique to convert the signal to a digital form. After conversion, the digital value is stored in a data stack within the ADC.

Upper and lower thresholds can be set within the ADC. If the signal falls outside

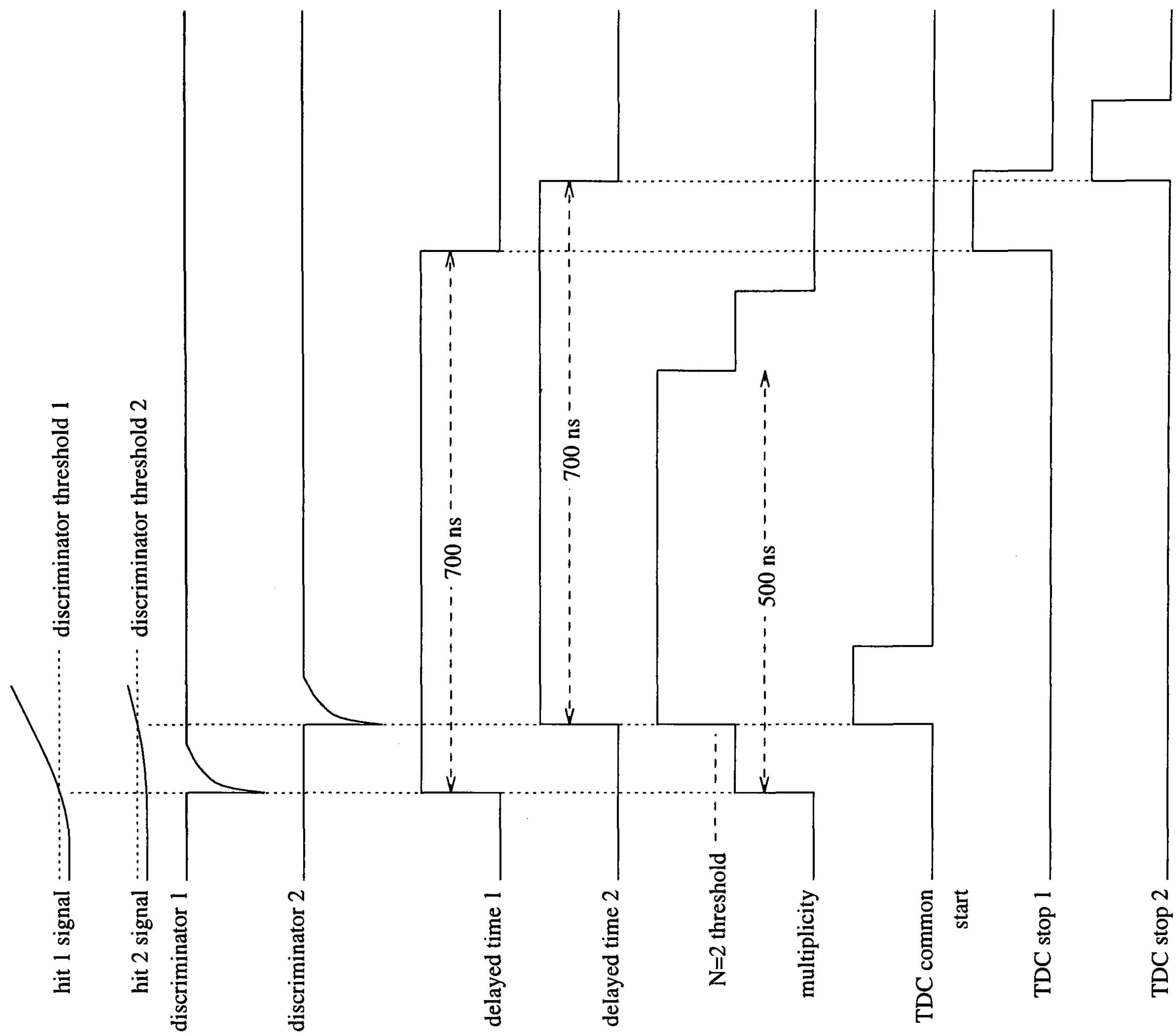

Figure 3.7: *The timing sequence followed for a typical event.*

these thresholds then that channel is marked, see Section 3.7.3.

The Time to Digital Converter

The Time to Digital Converters (TDC's) were LeCroy 4208's. They were started by a common start pulse and were stopped individually by the delayed discriminator pulse from each amplifier. The common start was produced by the logic electronics after it had determined that an event of interest was being seen. The timing sequence is shown in Figure 3.7.

The TDC's have a time window of 500 ns. Events arriving in coincidence were registered within the TDC, relative to the common start pulse. Random events generally arrived outside the time window, after the TDC had reset, and therefore the time for these events was registered as zero.

The time associated with each event was stored by the TDC on an internal data stack.

3.7.2 Logic Electronics

The logic electronics is used to signal to the Event Control Manager (ECM) that an event of interest is present. It takes as input the ADC discriminator pulses. Events can be of three types:

1. *Multiplicity Events:* These are the reaction events of interest. For each event the multiplicity (that is the number of individual alpha particles detected) within each detector is greater than a user defined threshold. The selection sequence followed for a typical event of this type is shown in Figure 3.7

   The discriminator pulses produced by the amplifiers for each end of each strip are OR'ed together, Figure 3.5. The result is a single discriminator pulse corresponding to each hit within a detector. This pulse is too short to be useful and is stretched to 500 ns before use elsewhere. 500 ns corresponds to the maximum walk time that is registered by the ADC discriminator between co-incident signals caused by their differing rise times, Figure 3.6. The stretched signals are input into a multiplicity unit, one for each detector. Here overlapping signals are counted. When the number of overlapping signals reaches a pre-defined limit, set by the user, an output signal is given.

   A co-incidence unit takes the output from each multiplicity unit and produces a strobe pulse, when both multiplicity units fire together. The strobe pulse is used to signal to the event manager that the current event should be stored on tape.

   At the NSF, the multiplicity condition was set to $N>1$ for each detector, to maximise the storage of ^{8}Be-^{8}Be events. At the ANU, the logic was changed slightly so that one of the multiplicity units and the co-incidence unit were removed. The signals from both detectors were input into a single multiplicity unit and the multiplicity requirement was set to $N>4$ for the whole event, to take predominantly events of type $^{12}C(0_2^+)+^{8}Be$.

2. *Singles Events:* The singles events corresponded to events that did not meet the full multiplicity criteria within one of the multiplicity units. This is signalled by the multiplicity unit through the $\leq N$ output. At the NSF, singles consisted of events, where, in one detector, the multiplicity was $N>1$, regardless of what the other detector contained, ie. the multiplicity criterium was met in one detector only. At the ANU, singles events corresponded to the

multiplicity condition N≤4 between both detectors. Singles events were taken as a calibration and normalisation check with a scale down of 1:1000.

3. *Pulser Events:* A Brookhaven Current Integrator (BCI) provided regular pulses through the electronics using mercury switch pulsers. The number of these pulses per second was regulated by the beam current. This provided an on-line check that the gains were not shifting and also provided a beam current indicator. The pulses were input through the test input of the pre-amps.

   The BCI was connected to the Faraday cup. It operates by producing 1000 pulses per second if the beam current at the Faraday cup corresponds to the full scale set on the BCI front panel. The full scale can be varied to take account of the beam intensity. The number of pulses going to tape was scaled down, usually in the ratio 1:400. As with the singles and multiplicity events above, each pulser event produced a strobe pulse. A veto was used on each multiplicity unit to prevent the pulser event producing a second strobe pulse through the logic electronics at the same time, by triggering the multiplicity units.

3.7.3 Event Manager

Each of the event types above produces a strobe pulse to indicate to the event manager that the event is of interest and should be stored. The modules comprising the event manager are shown in Figure 3.8. The main unit within the Event Manager is the Event Control Manager (ECM). As soon as the ECM receives the strobe pulse it initiates the ADC's. This was done by creating a 5 μs wide gate which is passed to each ADC, Figure 3.6. If the ADC detects a peak within the gate period then the peak height is held until it can be converted. The peak height must fall within user defined upper and lower height limits for the ADC to accept it. These limits are set within the ADC at startup. If the height of the peak falls outside these limits then this is signalled by raising bit 16 for that channel. The Silena 4418 ADC consists of 8 channels serviced by a single ADC chip. The conversion time for each signal is 4 μs, resulting in a total dead time of 32 μs within the ADC. When all of the ADC's have converted this is signalled to the ECM.

The ECM reads all ADC channels, regardless of their contents, using a Fera bus. The Fera bus consists of a daisy chain joining each ADC to its neighbour and to the ECM at each end. An enable signal is passed to each ADC in turn and its data is transferred to the ECM, at a rate of 100 ns per word.

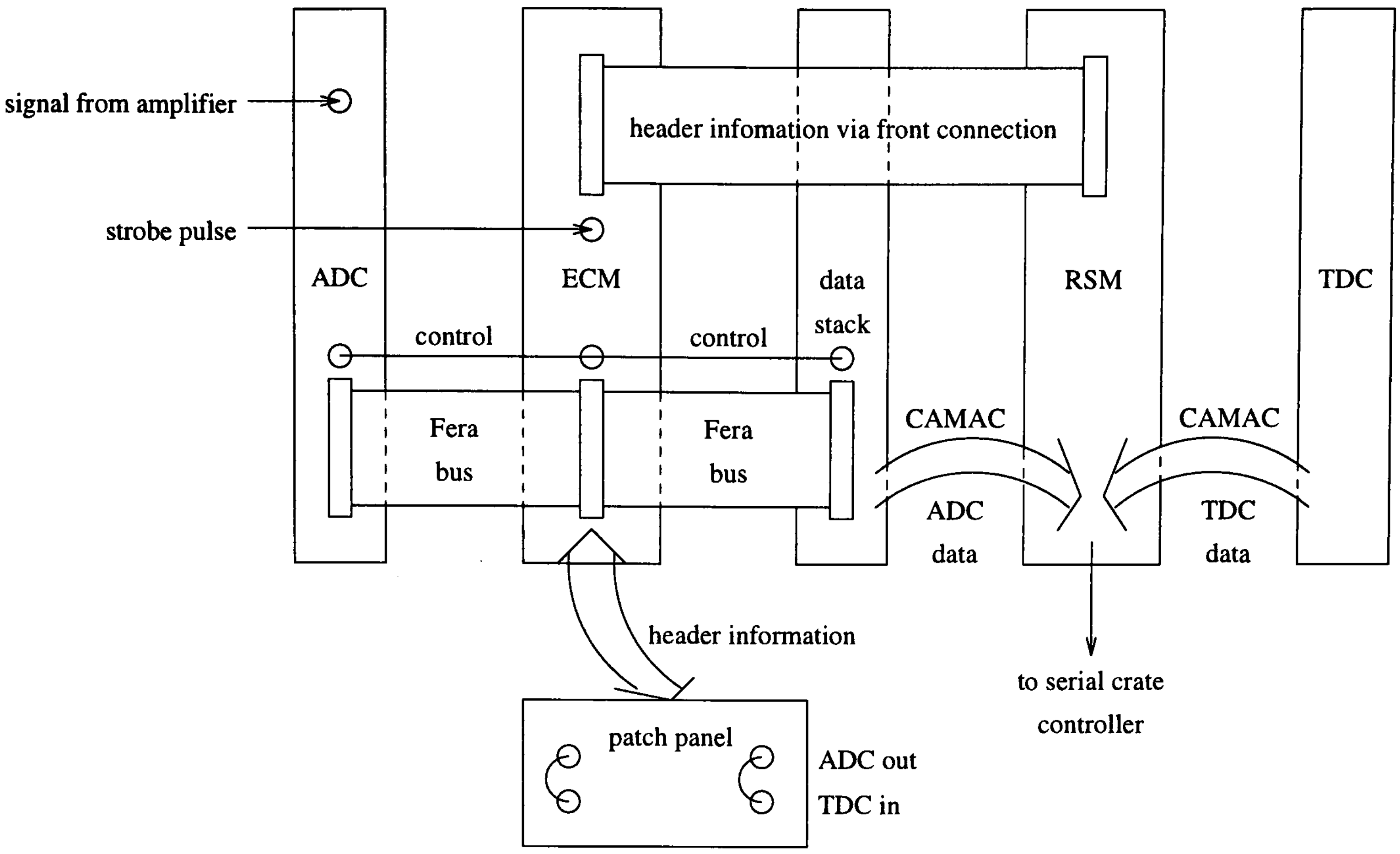

Figure 3.8: *A schematic diagram showing the connections between the event manager modules.*

Each channel is examined within the ECM and an ADC header is built up. For channels where bit 16 is not set and, additionally, are above another user defined threshold (whose level is common to all channels), a 1 is marked in the corresponding bit in the header. The data content of these marked channels is passed to the data stack. This continues until all of the ADC's have been read and all of the corresponding data is stored on the data stack.

The header words built up by the ECM form an address pattern with 1's corresponding to ADC's that contained data. They are written to a patch panel which links ADC's with their corresponding TDC's through links across the front panel. If an ADC channel contained data then the relevant TDC channels is marked through user defined connections. The full header indicating both the ADC and the TDC channels that contain data can now be constructed; this full header is returned to the ECM.

The ECM writes the header to the Read and Store Module (RSM) using a front connection. The RSM is essentially a large (2 kB) data stack within which the data from several events can be built up and stored. At the beginning of the experiment the address for each TDC and for the data stack are stored within the RSM. It now uses this information, together with the header, to construct the event as it will be stored on tape. The RSM uses CAMAC to transfer the data onto its stack. This process takes 2 μs per word. The address for the ADC data is always the data stack. For the TDC's the address is of the form X,A where X is the position of the TDC within the crate and A is the "A-code", the position of the data within the TDC. Only when all of the TDC data has been read is the system ready to be used again. The dead time for the whole system is typically 60 μs.

When the RSM stack is full, the data is passed one word at a time, using CAMAC, to the serial crate controller. The serial crate controller interfaces with a computer at the other end, passing all of the data down a serial link to be stored on tape. The RSM acquires data to a second stack while this process takes place.

Event Rates

Since the beam intensity can be chosen by the user, the main factor limiting the data taking rate is the electronic data collection system, see Figure 3.5. Within the electronics, there are several potential bottlenecks. The first of these occurs in the amplifiers. Each amplifier takes 10-20μs to process a hit. If a second particle is detected in the same strip within this time, then pile-up occurs and the information for both hits is lost. The second bottleneck is the digital electronics, including the ADC's, the ECM and the RSM. The serial transfer link also imposes a limit on the maximum rate since it takes a finite time to transfer the data for each event between the event manager and the computer. The dead time within the digital electronics and the serial transfer link can be broken down into a fixed part, independent of the event multiplicity, and a variable part, dependant on the event multiplicity. For the digital electronics, the fixed dead time includes 5 μs for the ADC gate, 32 μs for the ADC's to convert the data, $\sim$12 μs to transfer the data from the ADC's to the data stack and $\sim$16 μs to transfer the ADC hit pattern to the trigger interface and to read it back. In addition, the transfer of the data from the data stack to the RSM adds a variable factor of $\sim$0.8 μs per word. These combine to give a total of 65 μs fixed dead time, plus a variable contribution of 2.4 μs per hit.

The data stored within the RSM contains the header and hit words and the data. Between them, the header and hit words comprise 10 words, while the data constitutes three words for each hit, two corresponding to the signals at each end of the strip and one corresponding to the relative time of the hit. The serial link provides a transfer rate of 80 kB/s, or one word every 12.5 μs, thus in the transfer of one event there is a fixed overhead of 125 μs and the data adds 37.5 μs per hit.

Although from this analysis it would seem that the serial link severely limits the

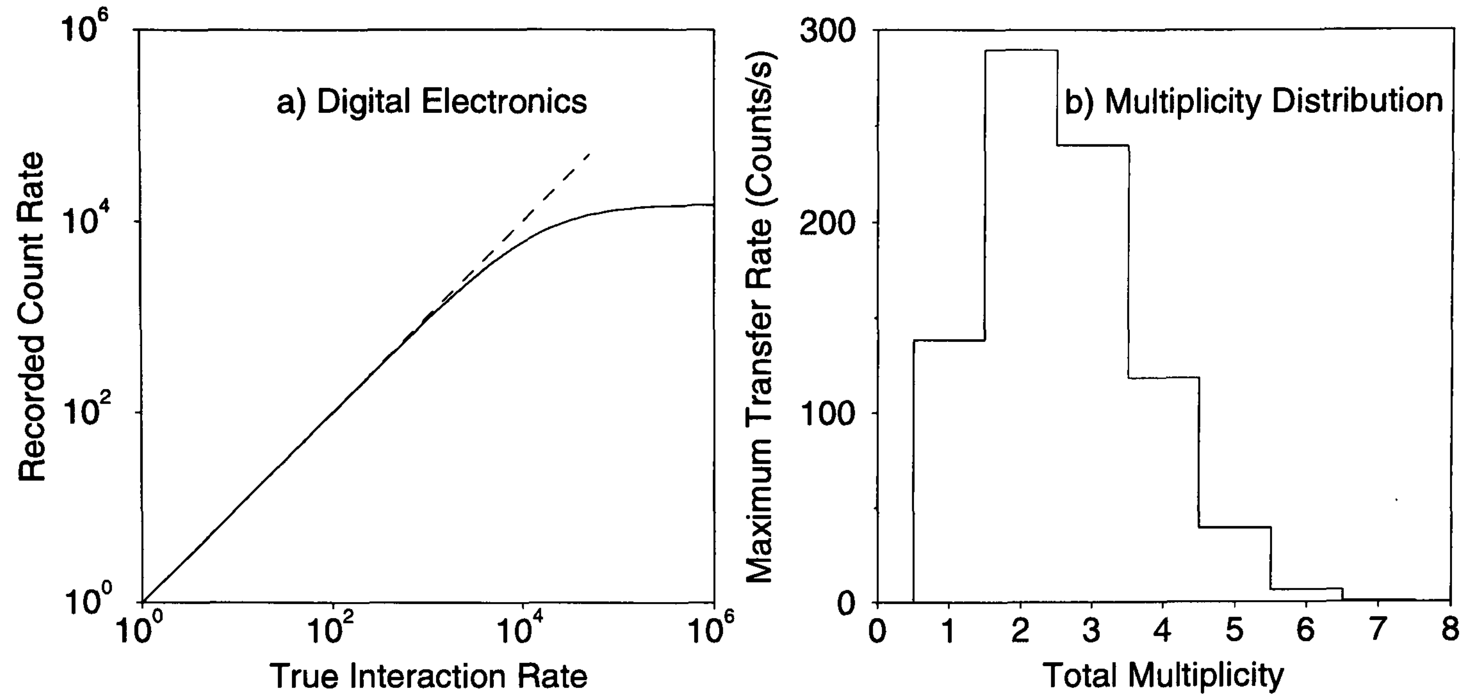

Figure 3.9: *a) The true count rate versus the recorded count rate for a dead time of 65 μs in the digital electronics. b) The multiplicity distribution for one of these experiments, after the rate for low multiplicity events has been scaled down.*

data taking rate, it should be remembered that the data rate through the analogue and digital electronics is random, while the buffers within the RSM are large enough to ensure that the output rate is smooth.

The maximum transfer rate via the serial link can be directly calculated as the inverse of the dead time. If the event rate is below this value then all events will be transferred, while above this rate, a backlog occurs as events are transferred more slowly than they arrive. For the analogue and digital electronics, the case is more complex. Due to the random nature of the hits, there is always some probability that a true event will be missed, because it occurs too soon after the preceding event. These losses can become severe when high count rates are used, making some dead time correction necessary. This correction is provided by the BCI pulsers, which are fed through the same electronics as the ordinary events, and therefore suffer the same dead time losses. If the electronics is dead for a time τ, then the recorded count rate, m can be written in terms of the true count rate, n, as:

$$m = \frac{n}{1 + n\tau} \tag{3.2}$$

Plotting n against m, shown in Figure 3.9a, it can be seen that losses become significant with a count rate greater than $\sim 10^3$.

During an experiment, the ideal count rate is one with which the maximum number of events of interest are being stored. As we have seen above, this is normally limited by the maximum transfer rate across the serial link. However, it is not always desirable to achieve the limit by varying the beam intensity alone, since the lowest multiplicity events will tend to have the highest count rates, and these are often not the events of most interest. Instead, a multiplicity unit is used to filter out and reject events whose multiplicity falls below a certain threshold, see Section 3.7.2, and hence reduce the load on the data gathering system. The beam intensity can now be varied to give the maximum event rate at the chosen multiplicity. If some low multiplicity events are required, then their rate can be reduced using a scale-down unit, see Figure 3.5. The resulting multiplicity distribution is shown in Figure 3.9.

3.7.4 Computer Controller

The event manager is controlled by a GEC 4080 computer (or VME emulator). The connection is via a serial link to the serial link controller in the event manager. During setup the GEC's functions include setting the upper and lower thresholds in each ADC, setting the threshold in the ECM and setting up the address map for the data stack and each TDC channel within the RSM. The last action of the GEC during setup is to enable the event manager so that it can take data.

As the GEC reads and stores the data it also processes a certain fraction through a user defined sort code. Typically the sort fraction is 10%. The sort code is similar to an off-line sort code, using a Fortran routine to process each event and produce histograms of the results. Each histogram can be displayed individually or compared with others. On-line sorting enabled each channel to be checked, to ensure that it was working correctly. Sorting was also used on-line to run a crude check that the reaction was being seen. This reaction sort is described in Section 4.3.2.

Chapter 4

Calibration

Calibration of the stored data forms one of the most important parts of the experimental analysis. The analogue electronics introduces offsets and gain shifts to the signals before they are stored. Off-line these effects must be corrected before any reaction data can be analysed. A number of different techniques are combined to provide a full correction of the data set; these techniques are described below.

4.1 Introduction

The PSSD's use a resistive readout method to obtain the position d and energy E of the incident particles, as shown in Figure 4.1. Readout is provided by an ohmic contact, in this case aluminium, which is evaporated onto the p^+ layer of the strip. Kalbitzer and Melzer have shown [Kal 67] that using this setup the PSSD has to be understood as a linear charge divider.

The charge collected at the contacts at either end of the strip is a linear function of the position d where the particle entered the detector. Thus, for a strip of unit length and unit resistance, the signals at each end will be

$$E \times d \quad \text{and} \quad E \times (1-d). \tag{4.1}$$

The analogue electronics amplifies the signals and introduces offsets so that they become:

$$AEd + \alpha \quad \text{and} \quad BE(1-d) + \beta \tag{4.2}$$

where A and B are multiplicative gain factors and α and β are the offsets.

In general the gain and offset of each channel is different, requiring that each channel be treated separately. In the sections below, the methods used to remove the offsets and to calibrate the signals are presented.

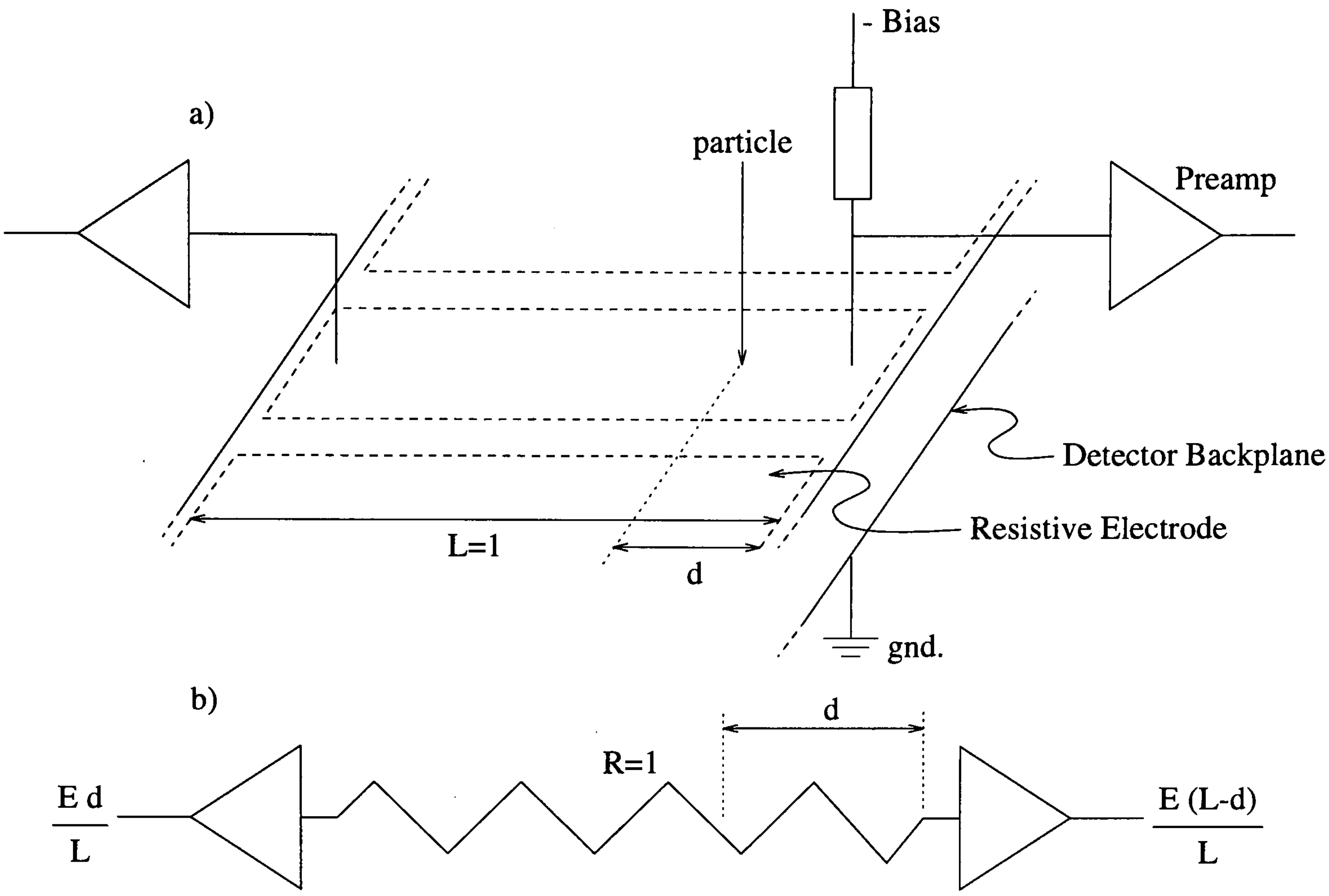

Figure 4.1: *a) Layout of part of a PSSD using resistive charge division and b) a simplified equivalent circuit.*

4.2 Pre-Run Calibration

4.2.1 The ADC Dispersion

In order to maximise the energy and position resolutions, the gain of each signal is set so that a particle with the maximum position$\times$energy signal expected for the reaction produces a voltage pulse corresponding to full range within the ADC. The ADC operating range is 0-10 V. Therefore the gain of each channel was set so that, when the most energetic particles were incident at one end of a strip, they produced a pulse of just less than 10 V at the ADC input. Calculations performed prior to the experiments showed that the maximum expected energy for the final state alpha particles was 30 MeV. Thus the ADC dispersion was set to 40 MeV full scale. Calibration was provided by a ^{241}Am source. This produced alpha particles with a mean energy of 5.6 MeV. The signals from each strip are a function of both energy and position, however, at the extreme ends, the signal is approximately equivalent to the total energy. The amplifier gain was varied until the alpha energy signal from the end of the strip had been shifted to channel $\frac{5.6}{40} \times 4096 = 575$.

Setting the dispersion for each channel results in a crude gain match between channels. The channels now only differ due to the effect of the offsets.

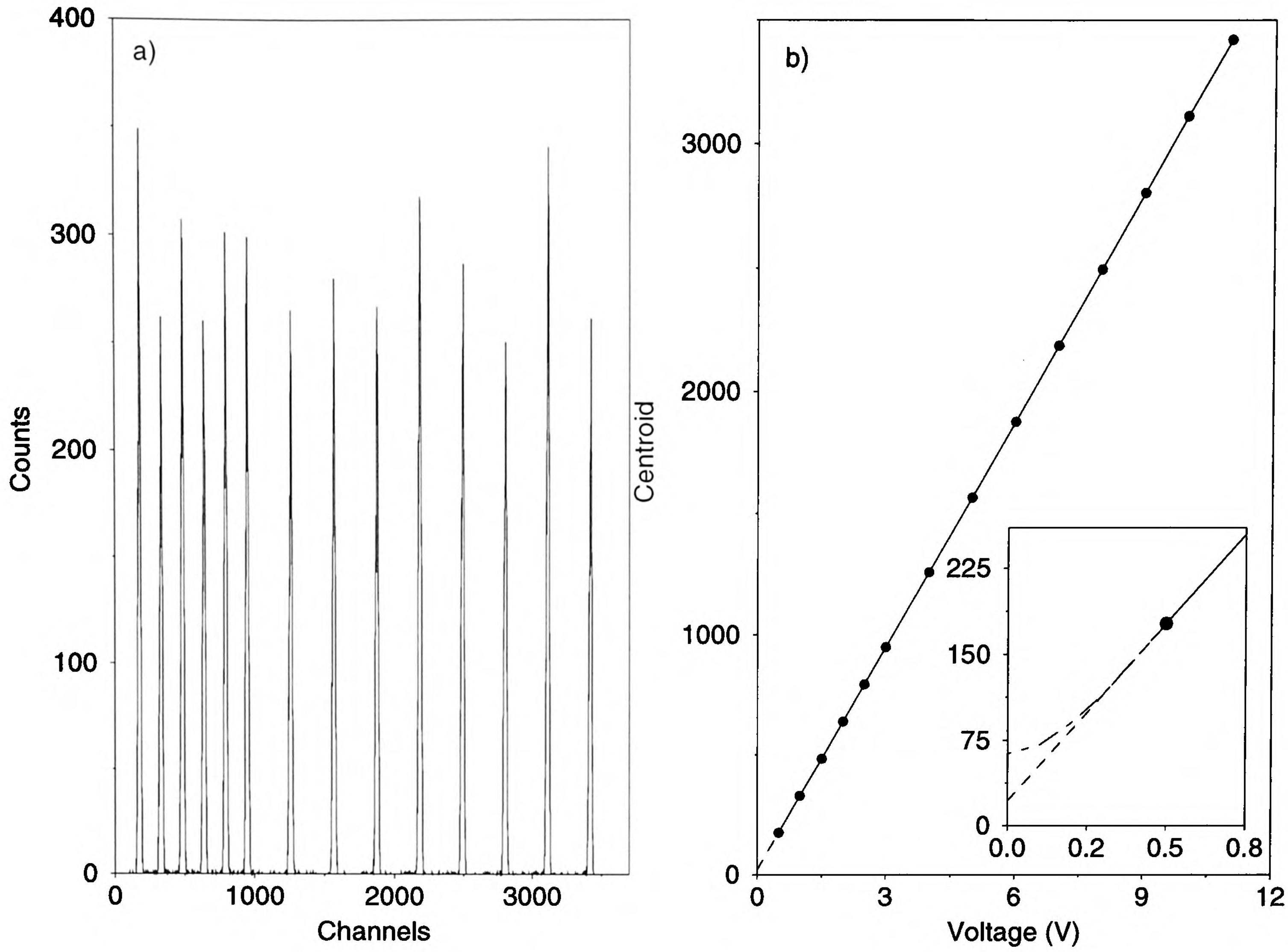

Figure 4.2: *The peaks resulting from a pulser walk through plotted a) against the channel in which the pulse appeared and b) against the input voltage. The extra peaks at low energy were to give better coverage in this region in case of non-linearities. The inset in b) is discussed later, in Section 4.4.2.*

4.2.2 Pulser Walk Through and Offset Removal

A small offset is often introduced by the ADC as the signal is converted. This offset is typically in the range 2 - 20 channels out of 4096 channels (5 to 50 mV). These offsets, α and β in equation 4.2, result in position - energy correlations and must be removed before the energy and position can be calculated correctly.

A pulser method is used. A series of accurate, regularly spaced voltage steps are produced using an Ortec 448 Research Pulser. The result is a series of peaks in the energy spectrum which are shown plotted in a histogram in Figure 4.2a. If the centroid of each peak is plotted against the voltage from the pulser then a straight line results, see Figure 4.2b. By linear regression, the offset can be read off as the y intercept. This offset can now be subtracted from the signals.

4.3 On-Line Checks

4.3.1 BCI Pulser

Throughout the experiment, a BCI provided regular pulses through the electronics at a rate dependant upon the beam intensity, see Section 3.7.2. The channels corresponding to the pulser centroids were noted, at regular intervals in time, to check for gain shifts. The width of the peaks gave an indication of the change in resolution. No gain shifts were observed during any of the experiments and the resolution was found to deteriorate only slowly with time.

4.3.2 The ^{8}Be-^{16}O-α Reaction

During the analysis of the first experiment, peaks were seen in the $^{12}C(0_2^+)$-^{8}Be-^{8}Be final state whose energy was apparently more positive than the seven-alpha breakup Q-value. It was found, Section 5.2.1, that these events were kinematically complete (that is, that all of the nuclei had been detected) and corresponded to events from the ^{8}Be-^{16}O*-α decay channel. The ^{16}O* and α stopped in one detector and effectively mocked up the second ^{8}Be, they could not be distinguished from it kinematically. Since these events were kinematically complete, this reaction was relatively straight forward to analyse on-line. In subsequent experiments they were used to check for gain shifts and to provide feedback on the reaction rates.

The energy difference between two alpha particles from the decay of ^{8}Be is approximately zero. This also happens to be the case for these ^{16}O-α events discussed. If the energy difference is plotted for any two particles detected within a single detector, Figure 4.3a, then events from the breakup of the ^{8}Be and from the ^{16}O*-α are clearly seen as a peak around zero.

The full ^{8}Be-^{16}O*-α final state can be selected by requiring that the energy difference between the two particles in each detector falls within the energy difference peak around 0 MeV. A Q_{tot} spectrum can be constructed by summing the energies of the four detected particles and is shown in Figure 4.3b. Since the ^{8}Be and the alpha particle are both in their ground states, the Q_{tot} spectrum only contains peaks corresponding to levels in the ^{16}O nucleus. Two peaks are seen. These are the ground-state peak and the unresolved doublets at 6.1 MeV and 7.0 MeV.

The width of the peaks gave a rough indication of the resolution, while their strength relative to the background and to the BCI pulser gave an indication of the reaction rate. It was found that the cross-section for this reaction drops rapidly with in-

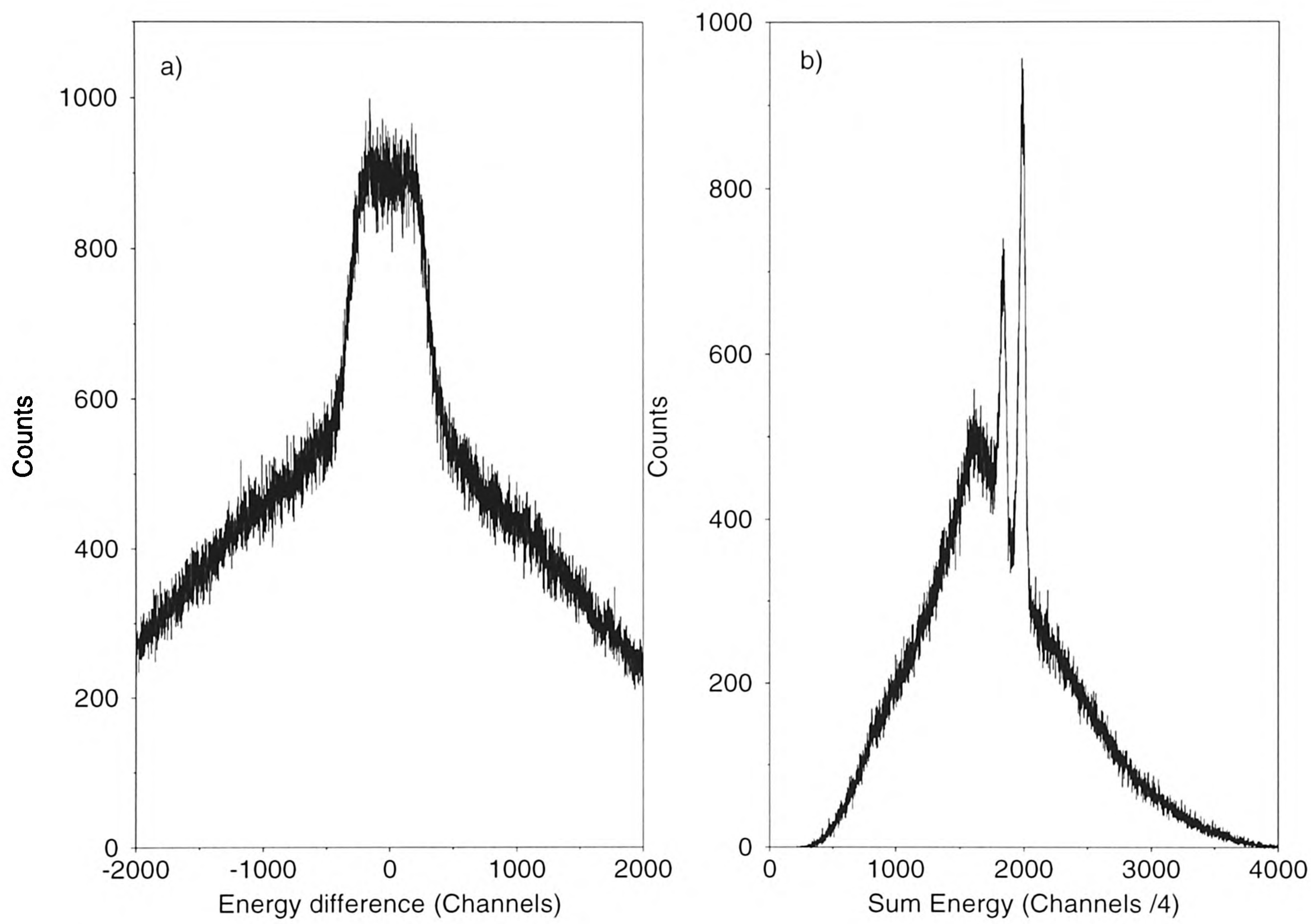

Figure 4.3: *a) The energy difference resulting from two particles hitting a single detector and b) the sum energy of all of the particles when the energy difference between the two particles in each detector is approximately zero. This figure was taken from the on-line sort used at ANU at a beam energy of 88 MeV.*

creasing energy with the highest cross-section for detection at a beam energy of 88 MeV.

4.4 Off-Line Calibration

At the start of every experiment elastically scattered ^{16}O nuclei were measured from a variety of targets. This provided data off-line to enable an accurate calibration of the detectors to be made. The beam energies were 35 MeV (at the NSF) and 32 MeV (at the ANU). At the NSF the targets were a 200 $\mu g/cm^2$ ^{197}Au foil and a 90 $\mu g/cm^2$ natural carbon foil. An additional target of 150 $\mu g/cm^2$ of ^{27}Al was used at the ANU. This section describes the method by which these data were used off-line to provide an accurate calibration of the detectors.

4.4.1 Energy and Position

The signals stored from each end of a strip as a result of the detection of a particle of energy E at position d are given in equation 4.2. If these signals are denoted σ_1 and σ_2 then, after gain and offset correction have been made, the energy can be determined as $\sigma_1 + \sigma_2$ and the position as $\frac{\sigma_1 - \sigma_2}{\sigma_1 + \sigma_2}$ giving:

$$E_m = BE + [(A - B)Ed + \alpha + \beta] \tag{4.3}$$

and

$$P_m = \frac{(A + B)d - B + \left[\frac{\alpha - \beta}{E}\right]}{B + \left[(A - B)d + \frac{\alpha + \beta}{E}\right]}, \tag{4.4}$$

where E_m and P_m are the measured energy and position. The square brackets contain the position / energy dependance that is to be removed by the gain matching and offset removal. It can be seen that, to remove these dependencies requires that the gains A and B are made equal, and the offsets α and β are removed by subtraction.

4.4.2 Offset Fitting and Offset Removal

In Section 4.2.2, a method was described to measure the offsets α and β. After they have been calculated, the offsets can be subtracted from the signals to remove the energy dependance of the position. During the analysis of the first experiment it was found that this correction did not work. Plotting measured energy against measured position, Figure 4.4a, it can be seen that the position still has strong dependencies on the energy. The correlated effects are largest for the very low energy particles, while the use of the resistive division strip detector exacerbated the problem because, for a particle at one end of the strip, the signal at the other end is already very low, see equation 4.1.

This was a new effect which only showed up when detecting low energy alpha particles. It was traced to non-linearities at very low energies (see inset in Figure 4.2b). Tests showed that these non-linearities were introduced when the ADC converted signals at the lower end of its working range. Since no data had been taken at these low energies during the pulser walk-through, it was necessary to correct for the effect numerically. This was achieved by fitting the curves in Figure 4.4a using equations 4.3 and 4.4. When these new offsets were subtracted from the signals all dependencies of the position on the energy were seen to be removed, Figure 4.4b.

In the two subsequent experiments the problems of non-linearities for low energy signals caused by particles detected near the ends of the strips was solved by the addition of 470 Ω resistors at each end of each strip. These resistors effectively added an additional offset to the signal at each end of the strip, so that the signals became

$$\frac{AE(d+r_1)}{1+r_1+r_2}+\alpha \quad \text{and} \quad \frac{BE(1-d+r_2)}{1+r_1+r_2}+\beta \tag{4.5}$$

where r_1 and r_2 are the resistances relative to the resistance of the strip, which is taken to have unit resistance. Energy and position can be calculated as before.

4.4.3 Software Calibration

After the offsets have been removed there may still be a dependance of the energy on the position across the detector. This can be removed by better matching of the gains A and B using multiplicative factors, C and D, such that AC=BD. Then the measured energy E_m becomes

$$E_m = (BD)E \tag{4.6}$$

and the position becomes

$$P_m = 2 \times d - 1 \tag{4.7}$$

In addition, both the energy and the position must be accurately calibrated. The method used to match the gains and to calibrate the detectors was changed between the experiments at the NSF and the ANU. Both methods are described below.

Calibrating with Masks

The standard method for calibrating the position signals from the detectors is to use a mask. This is placed in front of the strip detector during the calibration runs. It

a)

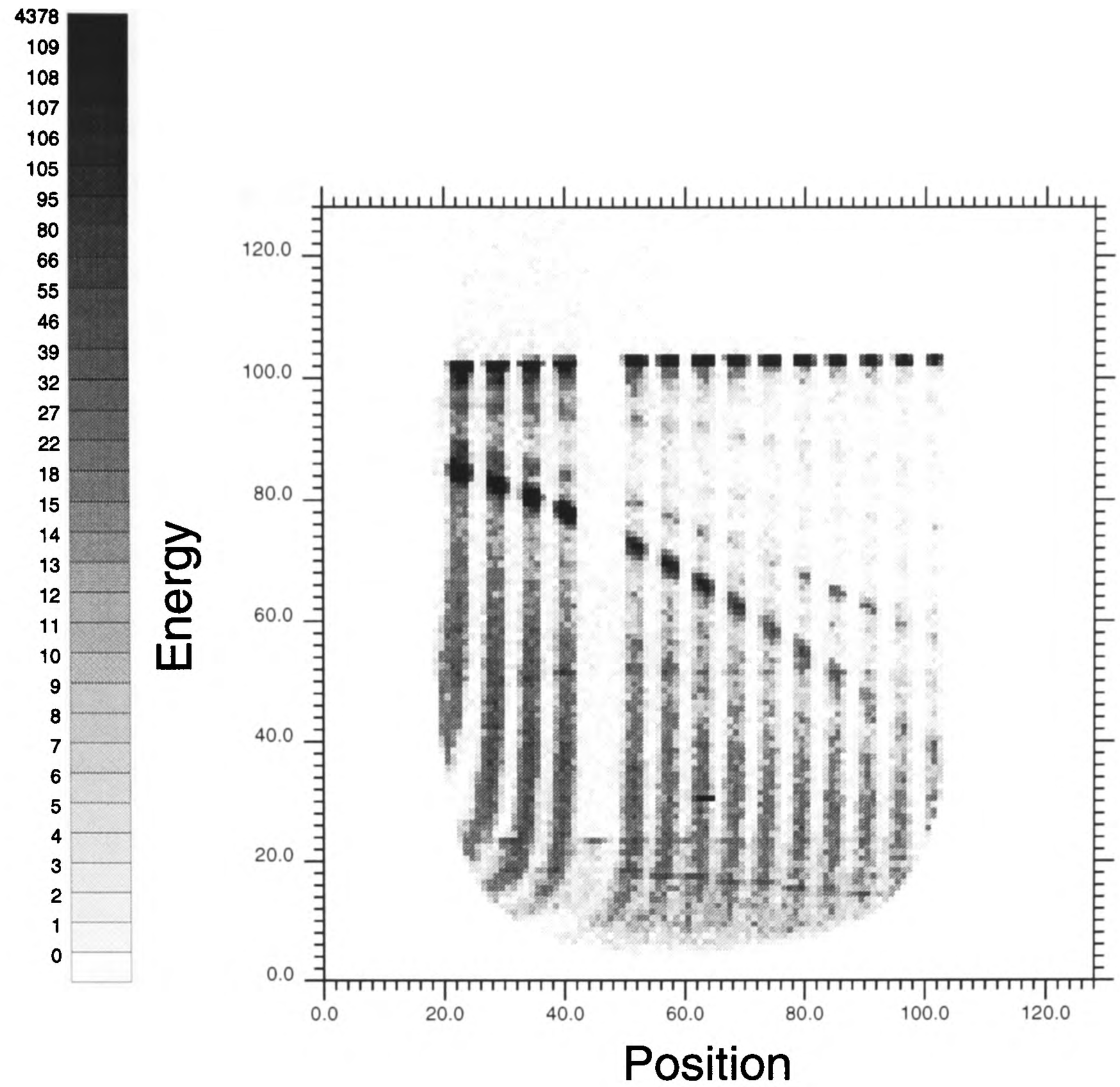

b)

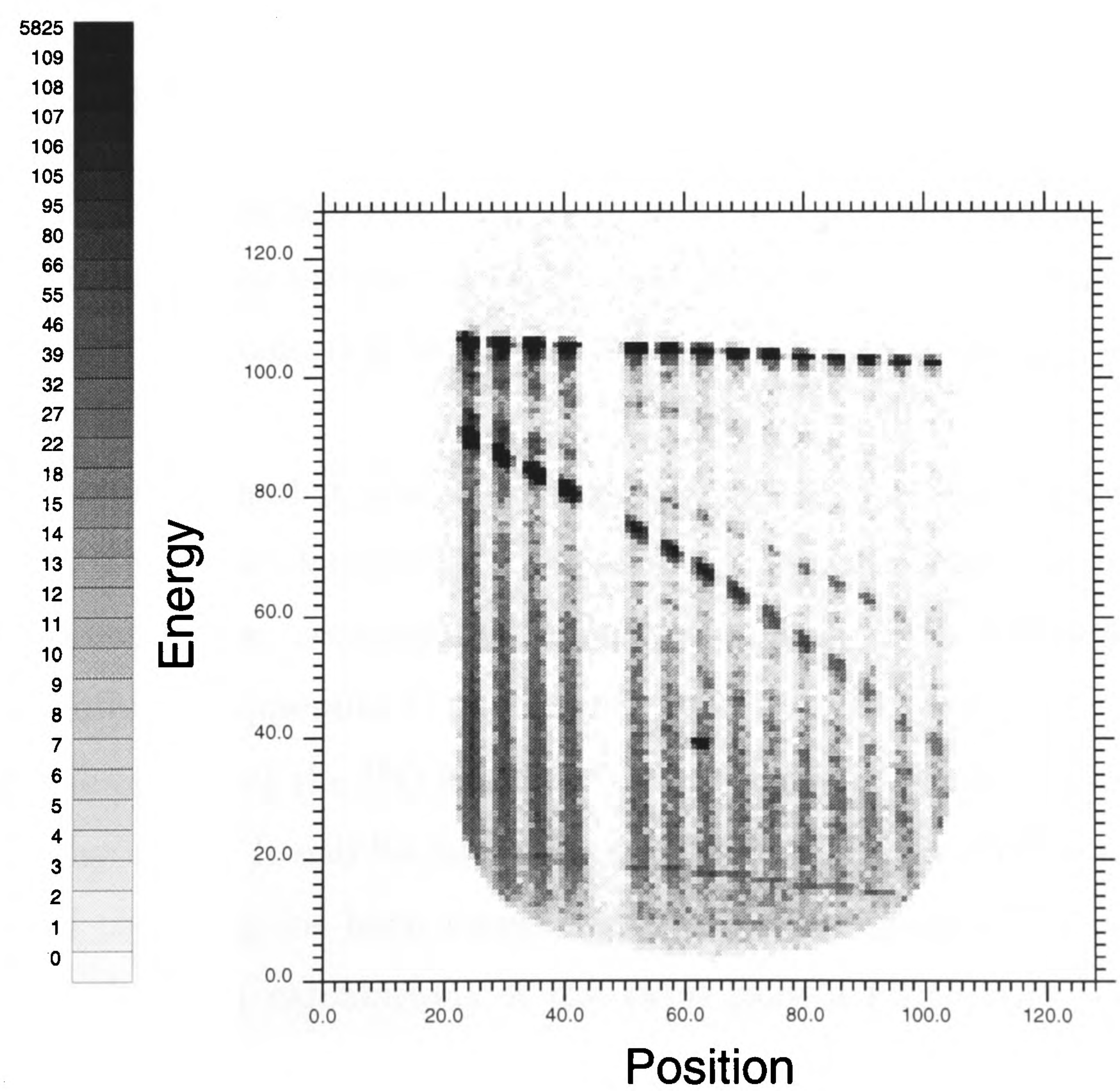

Figure 4.4: *Energy plotted against position for elastically scattered events a) before and b) after offset correction.*

consists of 14 vertical slots 1.5 mm wide and on a 3 mm pitch. One slot was blanked off to enable the orientation of the detector to be determined unambiguously off-line. The mask was calibrated by measuring the angle of each edge of each slot from behind using a telescope aligned with the beam line. With the detectors at their running angles, the low energy ^{16}O beam was used to produce elastic scattering data from a ^{197}Au target and a natural carbon target. A typical energy versus position plot from one strip, containing the combined data from both targets is shown in Figure 4.4. The effect of the grid can clearly be seen as the vertical stripes in the spectra. The measured position, P_m of the edges of the slits can be related to the measured angle using a spline fit. If the angle at any point is known, then the energy of the elastically scattered ^{16}O ions at that position can also be calculated using a kinematics program. This enables the measured energy, E_m to be corrected using a multiplicative correction at each edge of each slot. A spline fit is again used to give the correction at any point across the whole detector. The end result of this fitting process is two spline functions which, when applied to the measured energy and position of a particle, provide a calibrated output corresponding to the real energy and position.

Calibrating without Masks

At the ends of the calibration runs, the grids must be removed from in front of the detectors. The long time interval necessary between successive evacuations of the chamber at the ANU made this impracticable. Instead it was decided to calibrate without grids.

With the previous method it was only necessary to use one set of elastic scattering data to calibrate the detectors, as the grids provide the angular information. Without grids it becomes necessary to use two data sets. This calibration method is covered in detail in Appendix C and is only briefly covered here.

The ratio of the energy of the ^{16}O ions elastically scattered off two different targets is unique for any angle. It will be independent of the gain since this is a multiplicative factor and the same for both targets. Hence, by comparing this ratio for the measured particles with calculations of the ratio from a kinematics program, the angle can be determined.

After the angle has been determined, the kinematics program can also give the energies of the scattered particles from each target. If these calculations are performed at the ends of the strip (where d=0 or 1) they provide enough information to allow the calculation of all of the unknowns, A, B, r_1 and r_2.

Now by inverting these results, a correction can be obtained that relates the measured energy and position of any detected particle to the real energy and angle of that particle for a hit anywhere on the detector.

Calibration Check

During each experiment, data was taken from one more target than was actually needed for the calibration process. In each case this was the data from a natural carbon target. This data was used as an independent check that the calibration was correct.

Using the Q-value equation 2.12, the Q value for the elastic scattering reaction $^{16}O+^{12}C \rightarrow ^{16}O+^{12}C$ can be found for the calibrated data. If the calibration is correct then a plot of the Q-value as a function of position along the strip yields a horizontal line at 0 MeV ie. Q=0 MeV for elastic scattering. The results of this Q-value check for a typical strip from the ANU experiment are shown in Figure 4.5 for each target type. The additional lines in these spectra are the result of impurities in the target.

4.4.4 Timing

The timing response of the strip detectors has been widely studied, see for example [Ben 92]. At the edges of a strip the timing signal is prompt and almost independent of energy, however towards the centre of a strip, the timing signal becomes increasingly retarded, and the leading edge nature of the amplifier discriminator leads to a strong dependance with particle energy.

Bennett et al. [Ben 92] found that a correction was needed for each strip. This correction needed to be a function of both position and energy. For these experiments it took the form

$$t_c = t_m - f(P_m, E_m) = t_m - \frac{A}{E_m} - \frac{B}{C - P_m} - \frac{D}{E - P_m} - offset \qquad (4.8)$$

where t_m and t_c are the measured and corrected times respectively. A, B, C, D and E are constants determined for each strip and the offset simply shifts the time relative to the time for other strips and the timing in the other detector. Two position terms were needed to enable a fit to both ends of a strip.

Time corrections can only be made using data which involve coincidences, that is using particles that have been detected in an event with a multiplicity greater than

a)

b)

c)

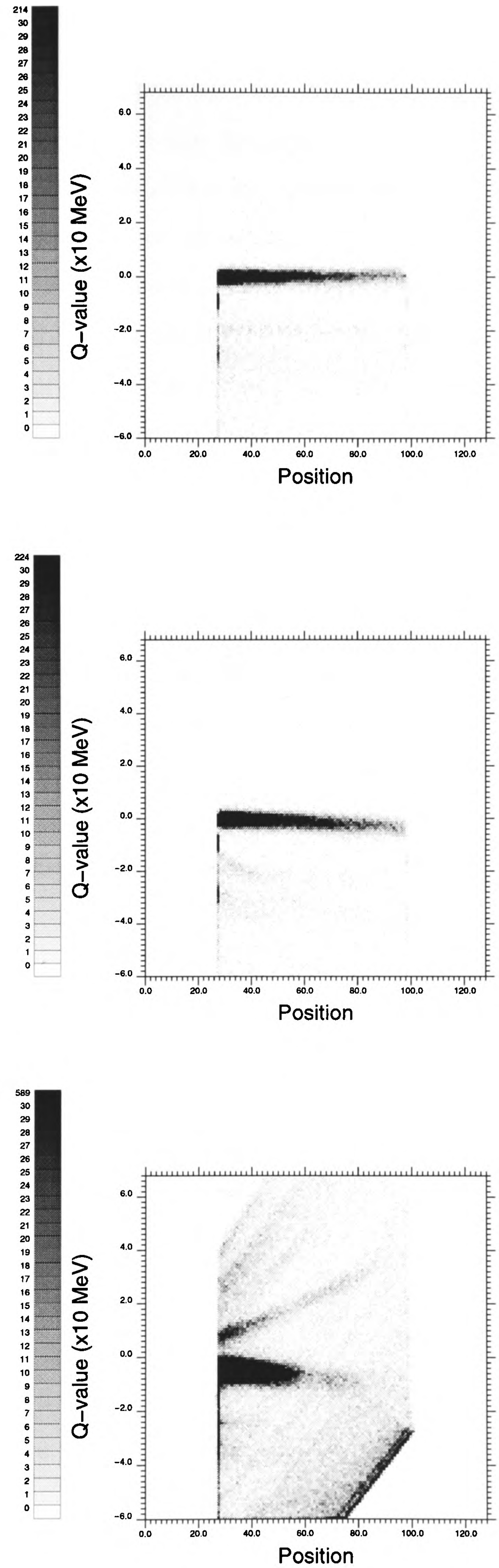

Figure 4.5: *The Q-value plotted for elastic* ^{16}O *scattered beam off a) gold, b) aluminium and c) natural carbon targets. The additional strong line in c) was produced by elastic scattering off* ^{16}O *impurities in the target.*

1, so that the common start pulse can come from a different source to the stop pulse. For these events, the time difference between the two hits is plotted against the energy and against the position for each hit, Figure 4.6a and b. In each case the relevant part of equation 4.8 can be used to fit the curves, giving all of the variables A to E. The offset is found by demanding that for a multiplicity two event, $time_1$-$time_2 \approx 0$ for any combination of strips.

A typical time spectrum after correction is shown in Figure 4.7. The time is plotted as t_{start}-t_c. Events of interest lie mainly within the peak around 540 ns, however low energy events may produce time straggling which results in a long tail below the peak and therefore this background may also contain many events of interest.

The ADC window was 5 μs wide, while the time window was only 500 ns wide. This difference meant that a large number of events were detected within the ADC window that were unconnected with the rest of the event. They were essentially of random origin and it was desirable to remove them. If the TDC is not stopped within its window then it over-runs and resets to zero. Therefore to remove these random events, gates would normally be put around the peak in the TDC spectrum. However it was found that any tight gate also removed many events that corresponded to valid data. Instead a single gate was used at channel 100. Events above this were accepted, while events below were assumed to be of random origin and were rejected.

a)

b)

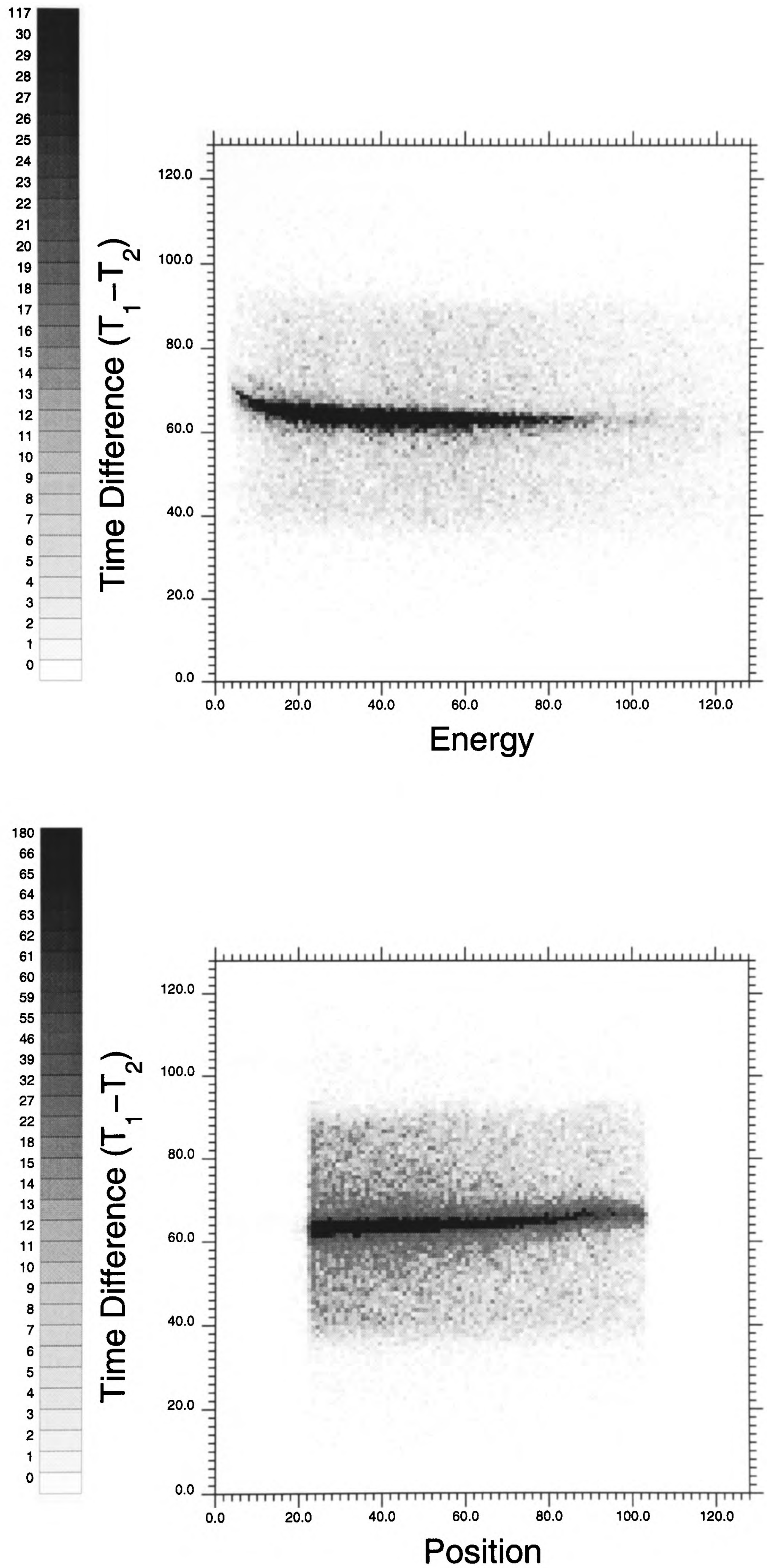

Figure 4.6: *Time difference spectra plotted against a) energy and b) position before correction.*

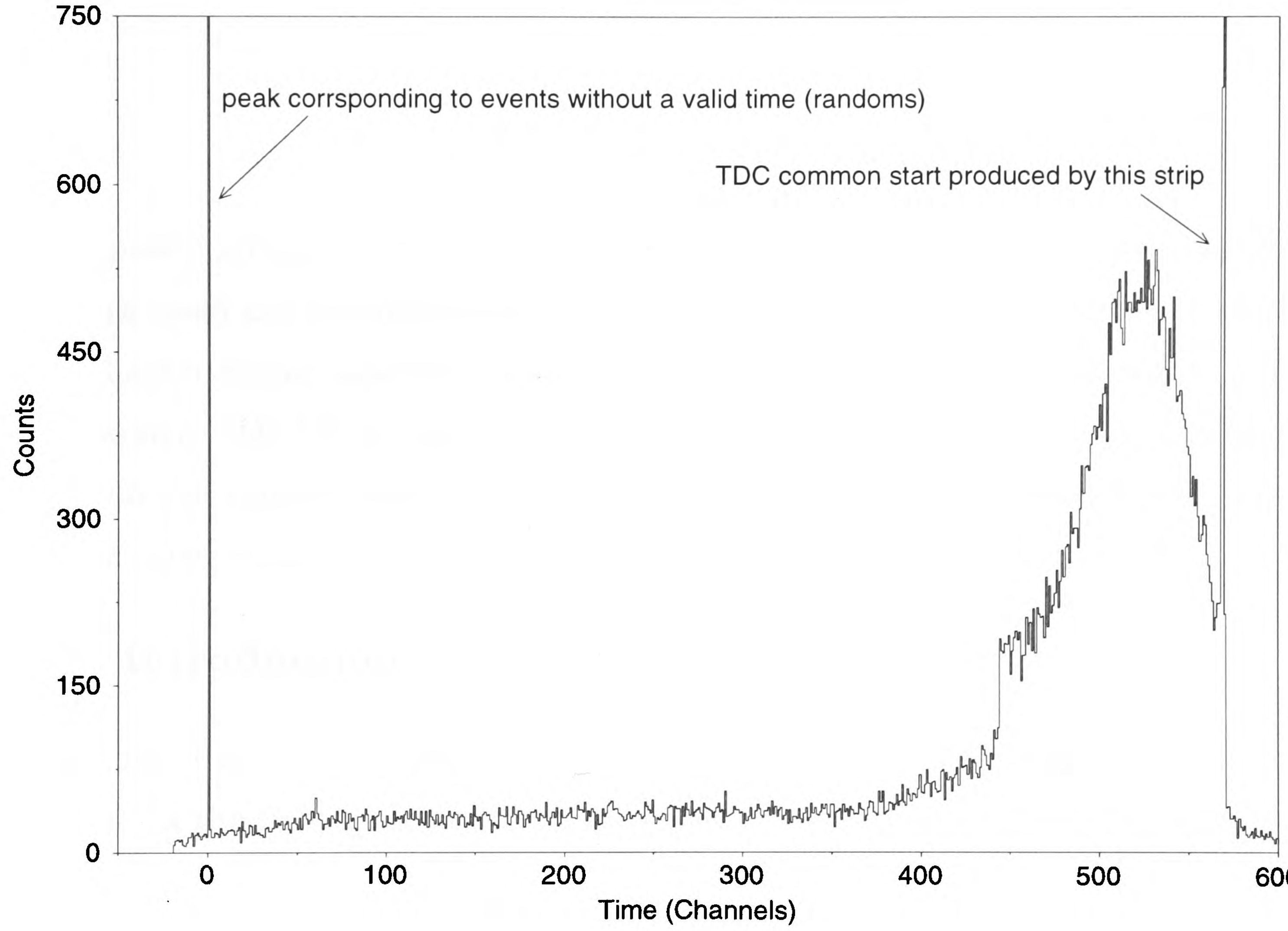

Figure 4.7: *A typical time histogram after the energy and position corrections have been made.*

Chapter 5

Results

In the previous chapters the decay properties that a ^{28}Si chain is expected to exhibit were discussed and a possible method for the detection of such a state was presented. This chapter brings together these ideas to present the results of this search using the reaction ^{16}O+^{12}C in the centre of mass energy range 37.7 MeV to 51.4 MeV. Two different types of final state have been studied during these experiments. They are presented separately below.

5.1 Introduction

In Chapter 1 it has been seen that chain states are predicted by a variety of nuclear models. In the lighter alpha conjugate nuclei, these predictions have a strong experimental backing. With the recent introduction of large two-dimensional PSSD's it has now become technologically possible to look for chain states in heavier alpha conjugate nuclei. The experiment to look for a six alpha chain in ^{24}Mg was reported by a group from Argonne in 1992 [Wuo 92] and has since been the source of much discussion. In this experiment they observed a resonance in the reaction ^{12}C+^{12}C $\rightarrow$ ^{12}C(0_2^+)+^{12}C(0_2^+) at a centre of mass energy of 32.5 MeV. This was within a few MeV of the prediction by Marsh and Rae of a six alpha chain state in ^{24}Mg [Mar 86]. In addition, a strong enhancement of the angular distribution at θ^*_{cm}=90° was observed on resonance in the ^{12}C(0_2^+)+^{12}C(0_2^+) breakup channel, this has been shown to be consistent with the possible chain state assignment to this resonance. In the first half of this chapter, the results of a similar search using the ^{16}O+^{12}C reaction to look for a seven alpha chain state in ^{28}Si are described. The analysis relied on kinematic techniques to simplify the seven-body final state.

Since the announcement of the observation of this resonance, several groups have performed experiments to study other breakup channels in the $^{12}C+^{12}C$ reaction in the same centre of mass energy region. The observation of this resonance has now been reported for the final states $^{8}Be_{(g.s.)}+^{16}O_{(g.s.)}$ [Ali 94], $^{12}C(0_2^+)$-$^{12}C(3^-)$ [Cha 95a] and α-$^{20}Ne^*$ [Mir 94] at the same centre of mass energy. Aliotta and Chappell also report that the angular distributions for these channels contain the same characteristic enhancement at θ^*_{cm}=90°. This suggests that other channels in the $^{16}O+^{12}C$ reaction may also contain the signature for a chain state. Some of these other channels have been examined and the results of this work are presented in the second half of this chapter.

5.2 The $^{12}C(^{16}O,n\alpha)$ Reactions

We have seen in Chapter 1 that the expected decay mode for a seven alpha chain is by splitting into shorter chains. Of these chains only the lightest, $^{8}Be_{g.s.}$, $^{12}C(0_2^+)$ and $^{16}O^*$ are well known and can be identified. Therefore these experiments were optimised to detect the breakup proceeding via chain states in these lighter nuclei. The final state consists of seven alpha particles. The efficiency for detecting all seven of these particles is very small, so that in general not all of the alpha particles will be detected. However using the methods and formalism of Resonant Particle Spectroscopy, Section 2.2, it has been shown that the undetected nuclei can be treated together as the third body in a quasi-three-body final state. The other two bodies correspond to the nuclei rebuilt from the alpha particles detected in each detector. The kinematic properties of the undetected nucleus must be inferred using conservation of momentum and energy. Unfortunately this leads to ambiguities. In all three of the multiplicity conditions examined, [$^{8}Be_{(g.s.)}$-$^{8}Be_{(g.s.)}$]-$^{12}C^*$, [$^{8}Be_{(g.s.)}$-$^{12}C(0_2^+)$]-$^{8}Be_{(g.s.)}$ and [$^{12}C(0_2^+)$-$^{12}C(0_2^+)$]-α[1], the ambiguity is in the choice between which two nuclei constitute the decay products of the resonant particle and hence between which two nuclei the relative energy should be calculated. The relative energy gives information on the state of the resonant nucleus. In practice this problem cannot be resolved and the relative energy is calculated between each pair of particles in turn.

At each energy the peaks in the Q_3 spectrum corresponding to each reaction channel were integrated. The normalised yield could then be calculated by dividing by the number of BCI counts. The BCI gives a correction for beam exposure and also for

[1] the square brackets denote the detected nuclei

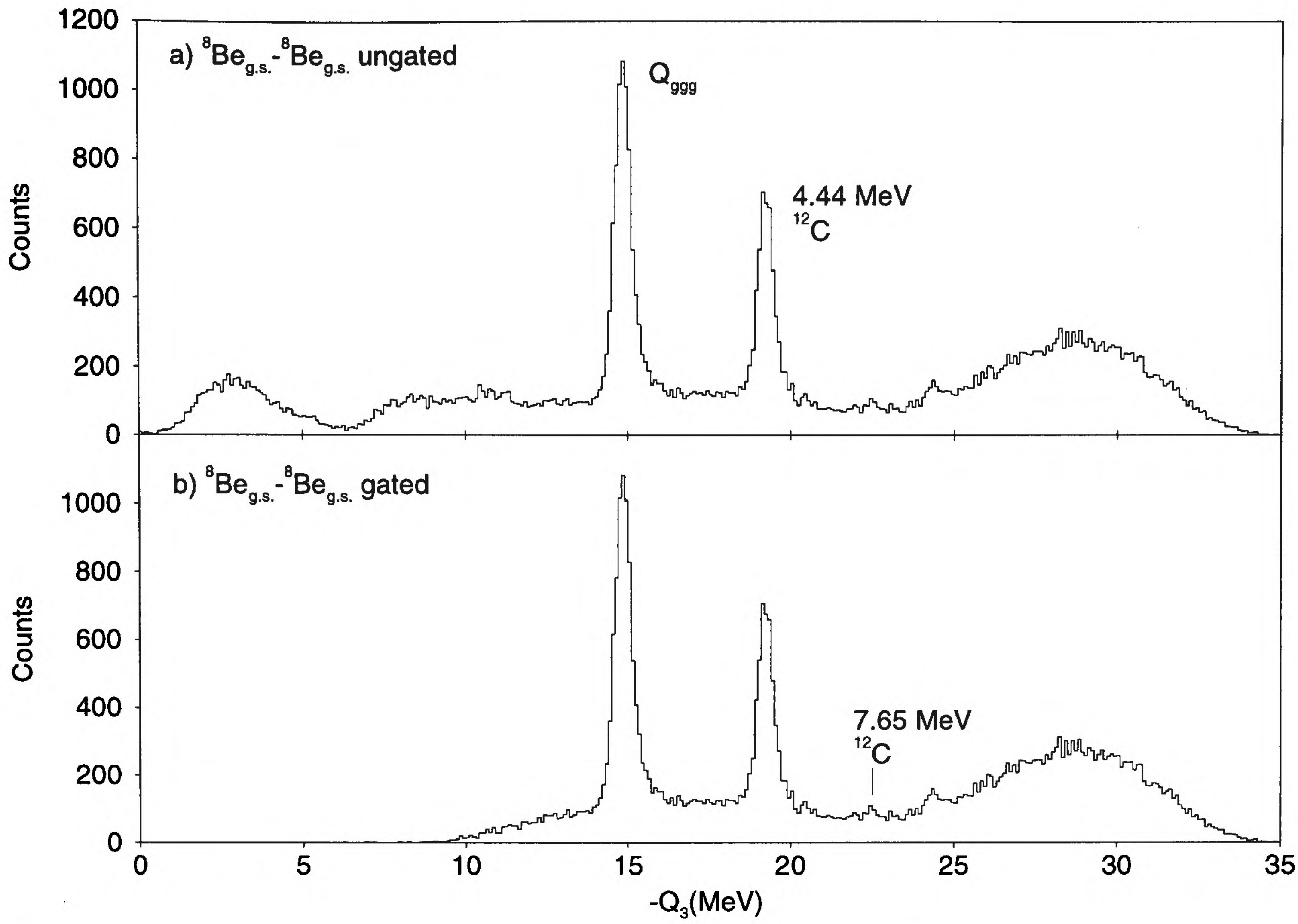

Figure 5.1: *The a) ungated and b) gated Q_3 spectra at $E_{c.m.}$=37.7 MeV from the detection of $^8Be_{(g.s.)}$-$^8Be_{(g.s.)}$.*

dead-time within the electronics. If the yield in each final state is plotted against energy then the signature of a chain state in ^{28}Si would be an enhancement of the yield over a particular centre of mass energy range.

5.2.1 [^{8}Be$_{(g.s.)}$-^{8}Be$_{(g.s.)}$]-^{12}C*

These events corresponded to the detection of two alpha particles in each detector. Each pair of alpha particles was identified as the breakup products from the decay of an ^{8}Be nucleus using the two body rebuilding method described in Section 2.4.1. For these events the Q_3-value is calculated and the results plotted in a histogram, Figure 5.1a. The undetected nucleus is ^{12}C*. The observed states in the histogram correspond to its ground state, Q_{ggg} and first excited state (2^+, 4.44 MeV). The 0_2^+ (7.65 MeV) at Q_3=-22.5 MeV is difficult to identify above the high background.
In addition to the events corresponding to ^{8}Be-^{8}Be-^{12}C*, there are also some events observed that have a Q-value which is apparently more positive than the seven-alpha breakup Q-value. These are events that have been misidentified and are not seven alpha events. Their identification and removal is covered below. The Q_3 spectrum after this background has been removed is shown in Figure 5.1b.

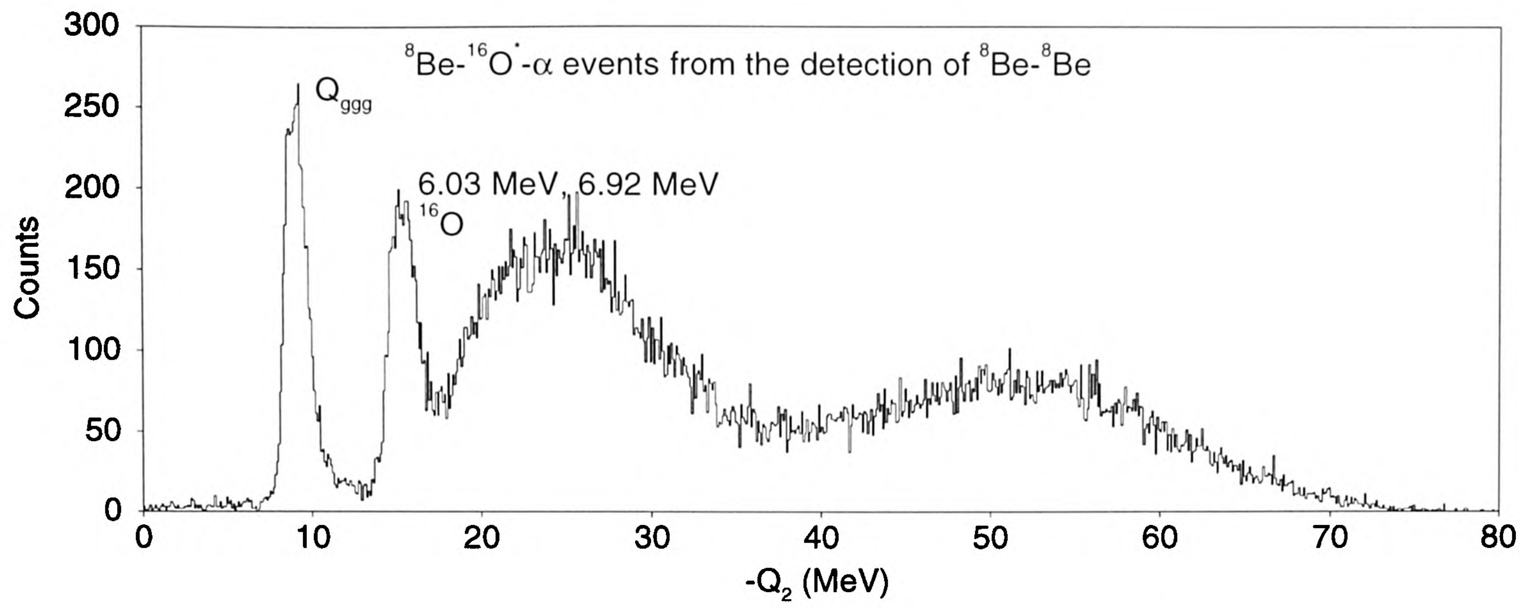

Figure 5.2: *The $^{8}Be_{(g.s.)}$-$^{8}Be_{(g.s.)}$ data at $E_{c.m.}$=37.7 MeV, plotted assuming all particles have been detected.*

Background Removal

These background events were used on-line to provide a measure of the reaction rates and the energy resolution and have already been mentioned in Section 4.3.2. If the Q-value is plotted assuming that all of the nuclei have been detected then the resulting Q_2-spectrum, shown in Figure 5.2, is seen to contain two sharp peaks from the background data. These peaks correspond to the ground state and the 6.050 MeV (0^+) and 6.919 MeV (2^+) states in ^{16}O. The 6.050 MeV and 6.919 MeV excited states cannot be individually resolved. From these excited states we can deduce that these events contain an excited ^{16}O nucleus.

It is thought that $^{16}O^*$-α events are being detected in coincidence in one detector and are mocking up one of the ^{8}Be's. Without particle identification they are essentially indistinguishable from a real ^{8}Be event and cannot be removed by gating within the $\alpha - \alpha$ relative energy spectrum. To remove these background events, a gate can be placed just above the two peaks in the Q_2 spectrum. Any events with a Q-value more positive than this gate are removed. This has the effect of removing any contamination from ^{8}Be-$^{16}O^*$-α reactions where the ^{16}O has an excitation energy of less than 7 MeV, shown in Figure 5.1b. However, it can be seen that this cut has no effect on the background below the peaks in this spectrum. Moreover, there is evidence that channels containing higher excited states in ^{16}O, in the excitation energy range 10 MeV to 14 MeV, may also be contributing to the background, see Section 5.3.2. These events would contribute to the background in the ^{8}Be-^{8}Be-$^{12}C^*$ Q_3 spectrum below the ground state peak. The two body kinematics for the background events, assuming ^{8}Be-^{20}Ne, indicate that the maximum scattering angle of the ^{20}Ne is 27°. Therefore, at angles greater than 27°, only the ^{8}Be-^{8}Be events should be detected. By rejecting events where the re-built nucleus on one side was at less than 27°, an enhancement of the $^{12}C(0_2^+)$ peak relative to the background was achieved. However, this enhancement was not enough to allow measurements to be performed on this state.

Relative Energies and Yields

In order to try to resolve the ambiguity in the choice of the resonant particle and hence to determine the decay channel through which the ^{8}Be-^{8}Be-$^{12}C^*$ final state is reached, the relative energy between the two ^{8}Be's and between each ^{8}Be and the $^{12}C^*$ is calculated for each excited state in ^{12}C. The results have been histogrammed and are shown in Figure 5.3. There is evidence for possible states in the ^{8}Be-$^{12}C_{g.s.}$ relative energy spectrum that would correspond to excited states in ^{20}Ne at 17.8 MeV and 19.2 MeV. A possible state can also be identified in the ^{8}Be-^{12}C (4.44 MeV) relative energy spectrum at 22.1 MeV. The high background and poor statistics prevented further analysis of these peaks to determine whether they are real, but they do seem to indicate that the reaction may proceed via states in ^{20}Ne. No structure is seen in any of the corresponding ^{8}Be-^{8}Be relative energy spectra.

The yields of all states seen for this multiplicity requirement have been measured as a function of energy. They are shown in Figures 5.4a and b. Overall the excitation functions from all three experiments are smooth and vary only slowly with energy, however a sharp peak is observed in the ANU data in all channels at $E_{c.m.}$=37.7 MeV. There are a number of effects that may account for this peak. If it is a resonance resulting from the excitation of a chain state, then an enhancement of the angular distribution at $\theta^*_{c.m.}$=90° is expected. No enhancement is seen, and in addition, no significant changes are observed between the angular distributions at $E_{c.m.}$=37.7 MeV and 39 MeV. Unfortunately, no data was taken below $E_{c.m.}$=37.7 MeV to examine this feature in more detail, however comparison with experiments looking at the ^{8}Be-^{20}Ne decay channel, indicate that the cross-section falls rapidly in this energy region. This may account for the peak, if the decay is proceeding through states in ^{20}Ne. The disagreement between the ANU data and the NSF experiments at this energy suggests that this peak may be an artifact of the experimental setup. A similar effect has been observed in the $^{12}C^*$ singles channels and the effect is discussed in more detail there, see Section 5.3.2. The lack of any other enhancement indicates that no resonances are being seen in these channels with a width greater

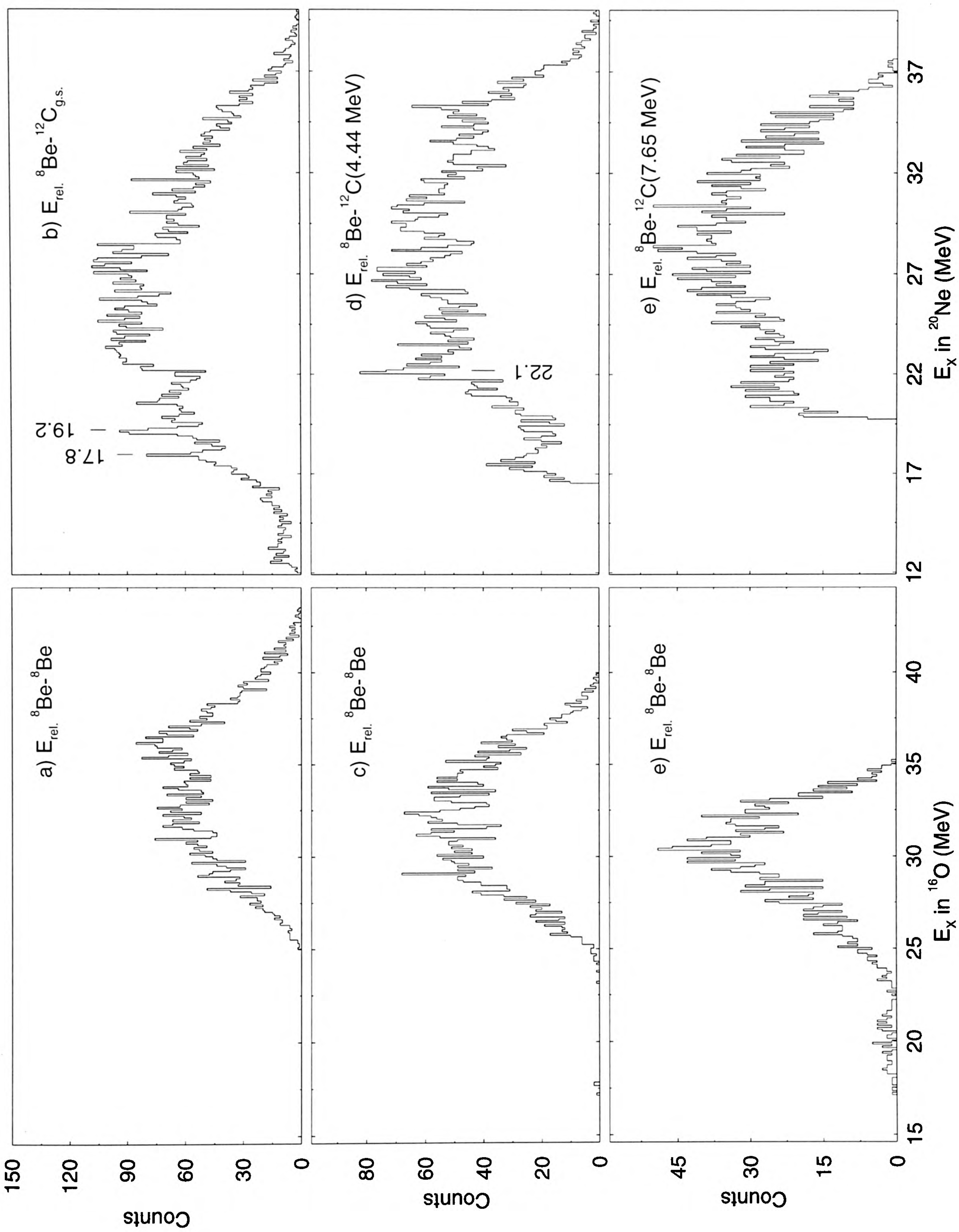

Figure 5.3: *The excitation energy of the resonant nucleus, calculated from the relative energies between the three final state nuclei ^8Be, ^8Be and $^{12}C^*$ for ^{12}C in its a) and b) ground state, c) and d) 4.44 MeV and e) and f) 7.65 MeV states, at a centre of mass energy of 37.7 MeV.*

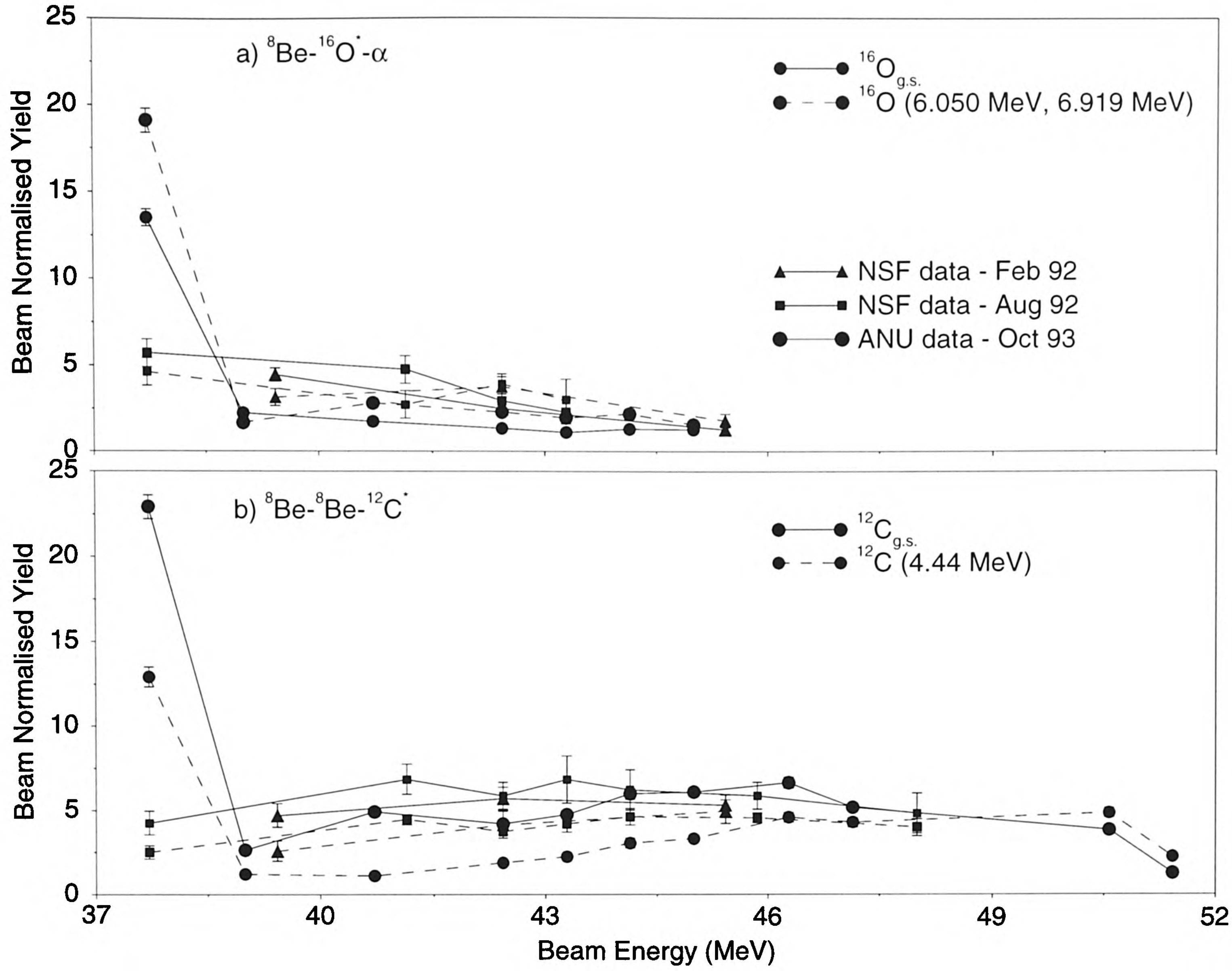

Figure 5.4: *The beam normalised yield for the excited states seen in the detection of a) ^{8}Be-$^{16}O^{*}$-α and b) in the undetected particle from the detection of ^{8}Be-^{8}Be.*

than approximately 4 MeV in the centre of mass and hence that there is no ^{28}Si signature observed in these final state channels.

5.2.2 $[^{8}\mathbf{Be}_{(g.s.)}$-$^{12}\mathbf{C}(0_2^+)]$-$^{8}\mathbf{Be}_{(g.s.)}$

These events correspond to the detection of two alpha particles from the breakup of the ^{8}Be in one detector and three alpha particles from the breakup of $^{12}C(0_2^+)$, through the $^{8}Be+\alpha$ channel, in the other detector. Once again the two body event rebuilding method described in Section 2.4.1 was used to re-build the nuclei in each detector. A histogram of the calculated Q_3 for these events is shown in Figure 5.5a. A single peak is seen at 22.5 MeV corresponding to the $^{28}Si \rightarrow 7$ alpha breakup Q-value. This peak sits on a background resulting from the continuum $\alpha - \alpha$ states. As before, events are seen whose Q-value is apparently more positive than the seven-alpha breakup Q value; they are discussed below.

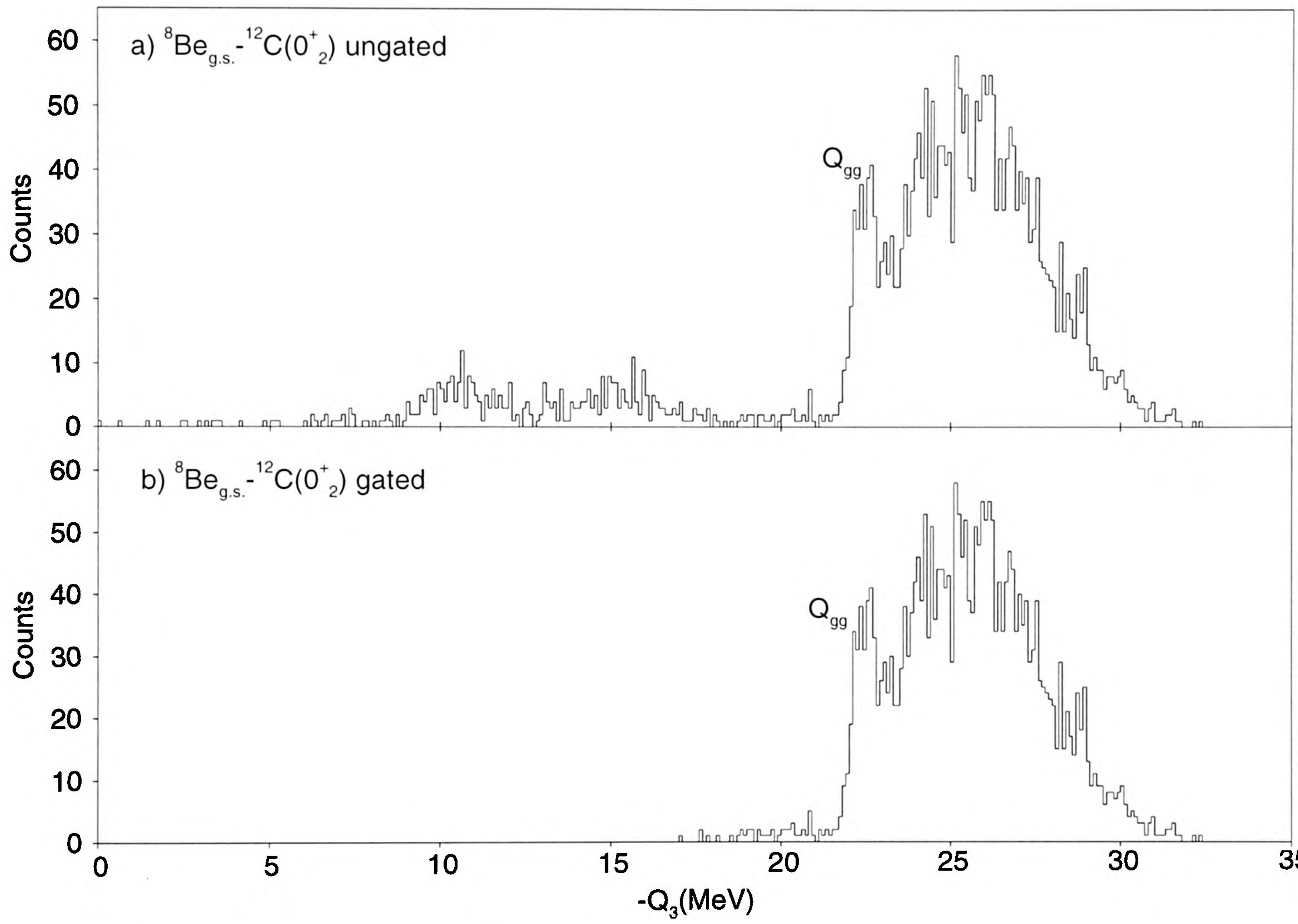

Figure 5.5: *The a) ungated and b) gated Q_3 spectra at $E_{c.m.}$=37.7 MeV from the detection of* $^8Be_{(g.s.)}$-$^{12}C(0_2^+)$.

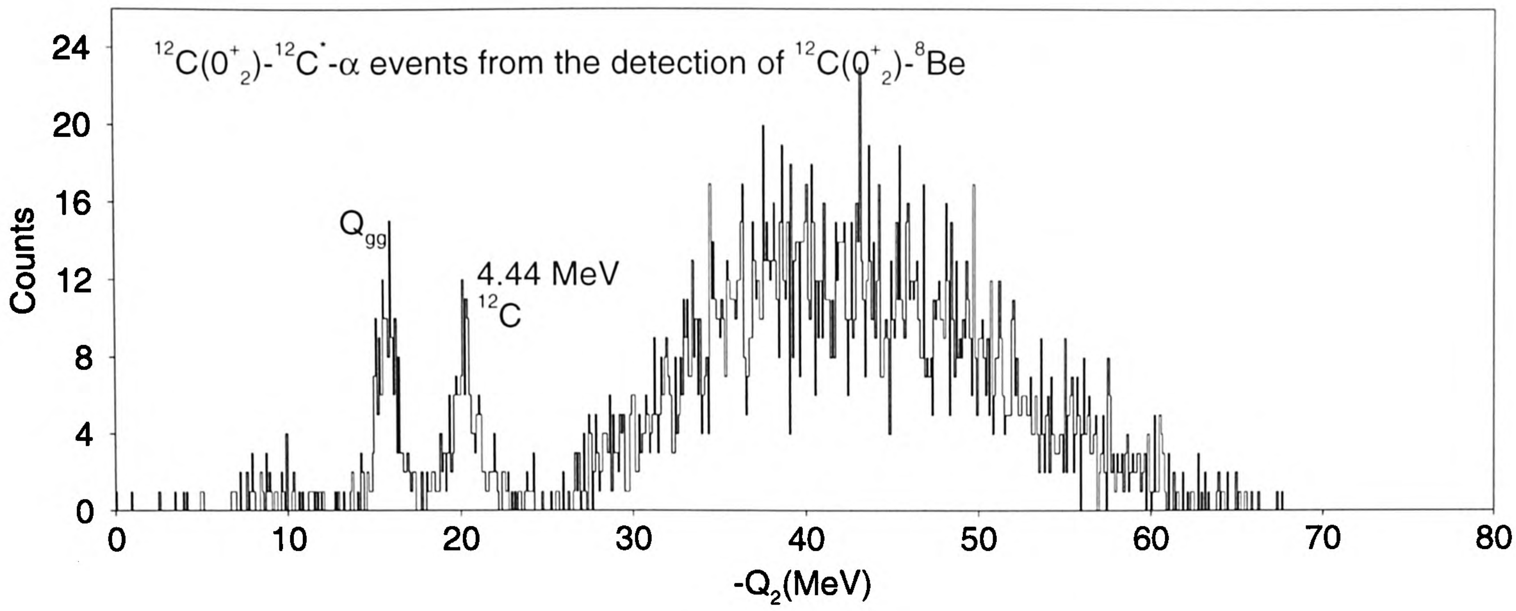

Figure 5.6: *The $^{8}Be_{(g.s.)}$-$^{12}C(0_2^+)$ data at $E_{c.m.}$=37.7 MeV, plotted assuming all particles have been detected.*

Background Removal

If the Q-value is plotted for these events, assuming that all of the particles in this breakup channel have been detected, then the resulting Q_2-spectrum, shown in Figure 5.6, contains two peaks. These correspond to the ground state and the first excited (2^+ 4.44 MeV) state in ^{12}C. They are thought to be the result of $^{12}C^*$-α events mocking up the ^{8}Be. They are essentially kinematically identical to real ^{8}Be events and cannot be distinguished from them by using the $\alpha - \alpha$ relative energy. This background is gated out by placing a gate just above the two peaks in the $^{12}C(0_2^+)$-$^{12}C^*$-α Q_2 spectrum. The resulting Q_3 spectrum for $^{12}C(0_2^+)$-^{8}Be-^{8}Be is shown in Figure 5.5b. Additional higher energy states in ^{12}C such as the state at 7.65 MeV are not expected to contribute strongly to the remaining background, Section ??.

Relative Energies and Yields

There are two possible resonant particles and hence two possible decay channels that could be represented by this detection configuration. These are ^{8}Be-$^{12}C(0_2^+)$ and ^{8}Be-^{8}Be, corresponding to states in ^{20}Ne and ^{16}O respectively. In order to try to identify the resonant particle, the relative energies have been calculated and histogrammed for the different possibilities. The ^{8}Be-$^{12}C(0_2^+)$ relative energy is calculated and plotted twice; once between the $^{12}C(0_2^+)$ and the detected ^{8}Be and once between the $^{12}C(0_2^+)$ and the undetected ^{8}Be. These relative energy spectra are shown in Figure 5.7. Although the statistics are poor, there does seem to be a peak at 20 MeV in the ^{8}Be-^{8}Be relative energy spectrum. The most likely explanation

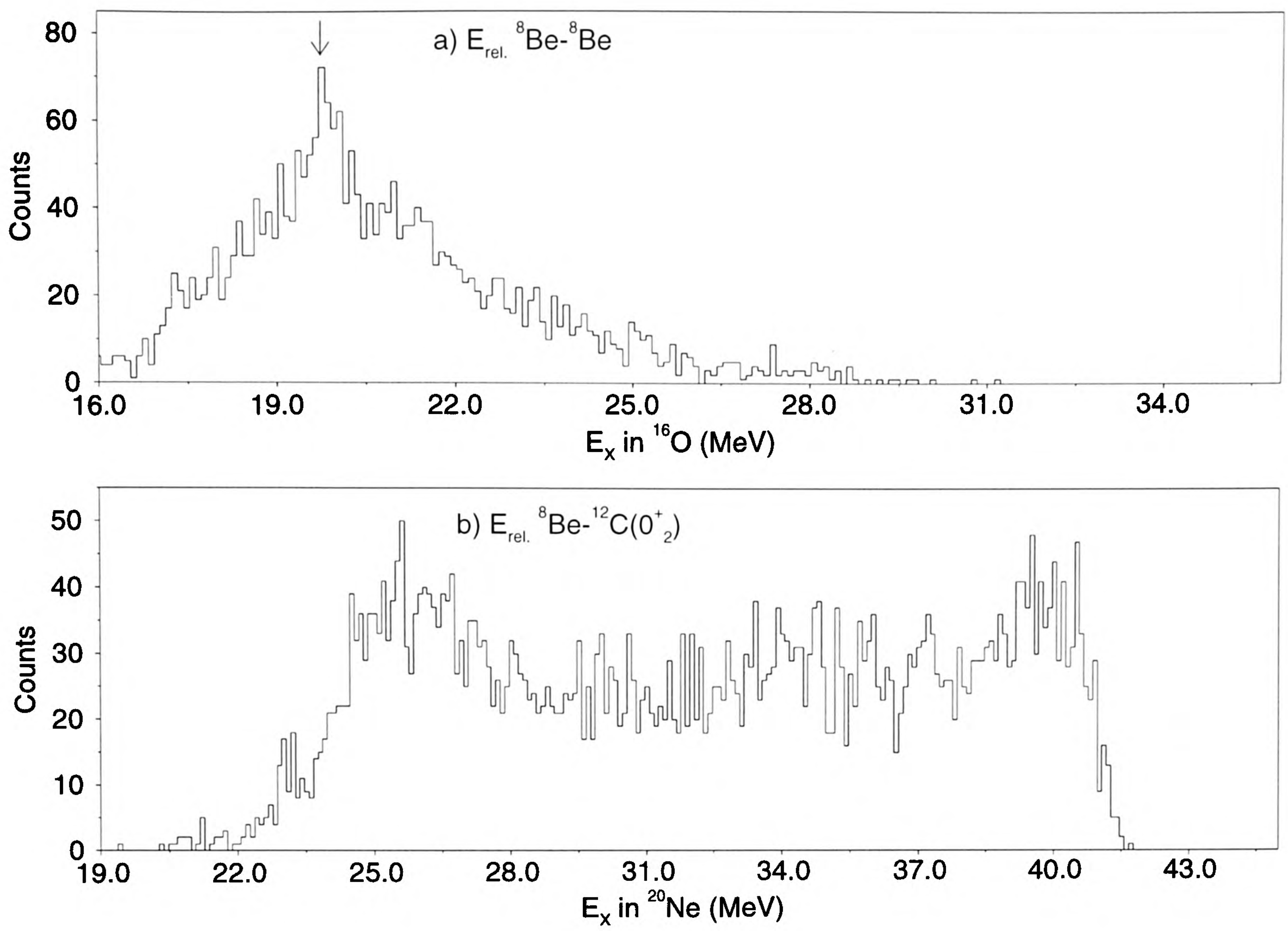

Figure 5.7: *The excitation energy of the resonant nucleus, calculated from the relative energies between the three final state nuclei ^8Be, ^8Be and $^{12}C(0_2^+)$. a) corresponds to ^8Be-^8Be and b) to ^8Be-$^{12}C(0_2^+)$, at a centre of mass energy 37.7 MeV.*

for this peak is that it is due to the enhanced efficiency at this relative energy. No structure is seen in the ^{8}Be-^{12}C(0_2^+) relative energy spectrum.

The yields for all states observed with this multiplicity condition are plotted in Figure 5.8. The poor energy resolution obtained during the second run at the NSF meant that no peaks could be resolved in either the Q_3 spectrum or the Q_2 spectrum. Similarly the resolution from the first run at the NSF was not good enough to resolve the peak at Q_3=-22.5 MeV in the ^{8}Be-^{12}C(0_2^+)-^{8}Be final state. The error bars shown on the ^{8}Be-^{12}C(0_2^+)-^{8}Be data from the ANU are probably an underestimate, since the Q_3=-22.5 MeV peak appears as a shoulder on the background, shown in Figure 5.5b, so that accurate peak integration relies on a good fit to the background at a point where its level is changing rapidly.

All of the yields vary only smoothly with energy and contain no structure. An enhancement of the yield would be expected, at a centre of mass energy of 43.0 MeV, if a chain was being observed. This enhancement is not seen.

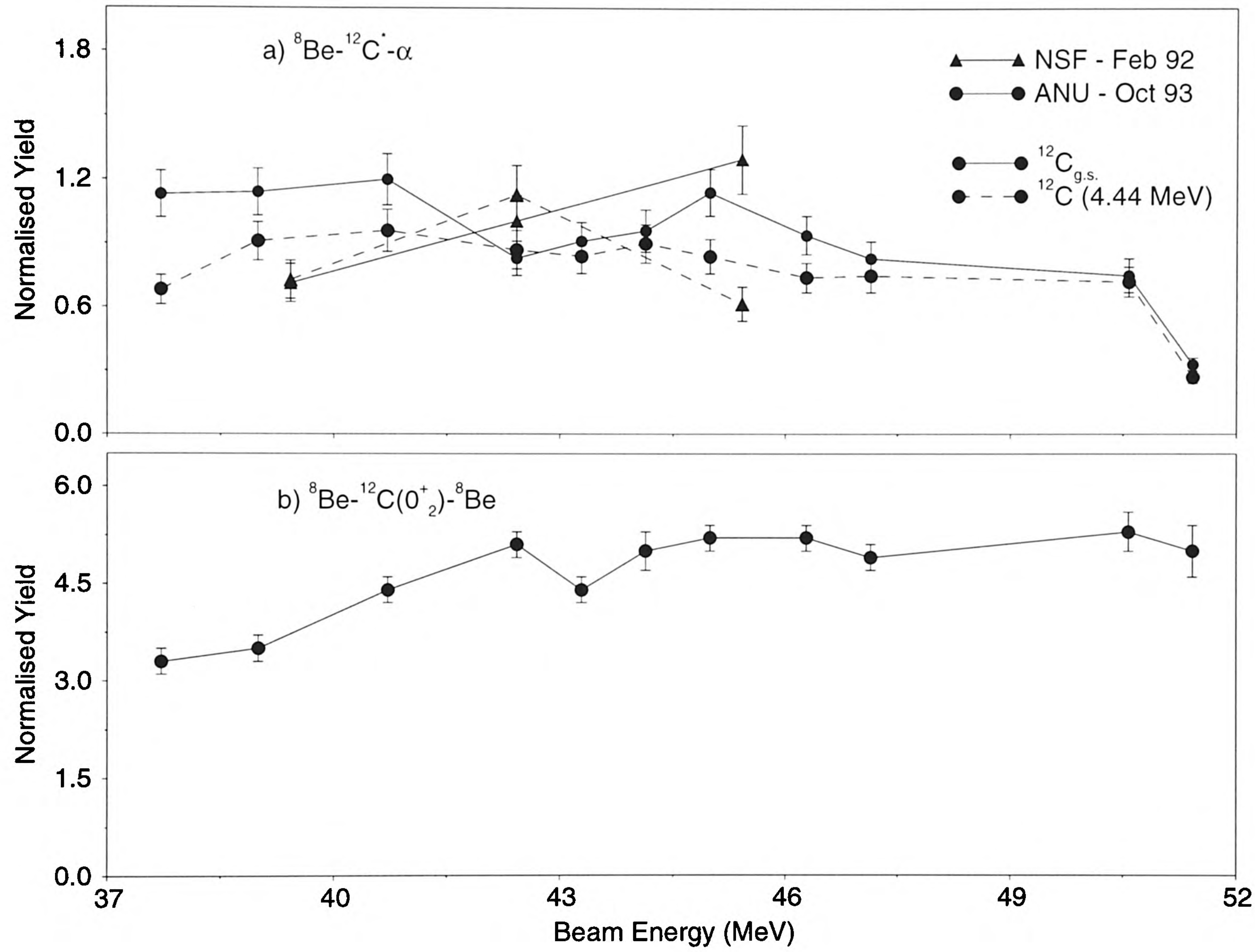

Figure 5.8: *The beam normalised yield for the excited states seen in the detection of a)* $^{12}C(0_2^+)$-$^{12}C^*$-α *and b) in the undetected nucleus from the detection of* $^{12}C(0_2^+)$-^{8}Be.

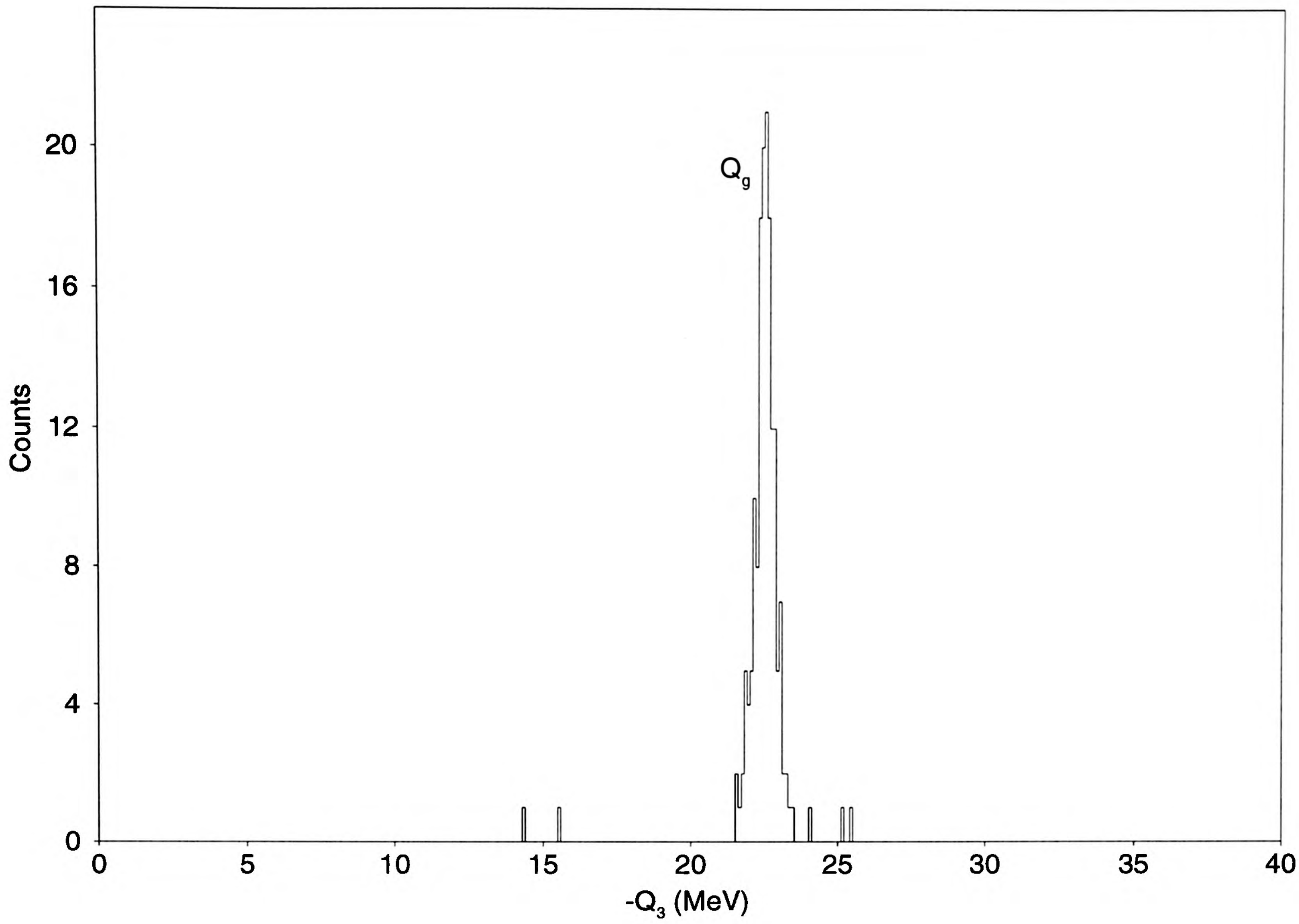

Figure 5.9: *The Q_3 spectrum at $E_{c.m.}$=37.7 MeV from the detection of $^{12}C(0_2^+)$-$^{12}C(0_2^+)$.*

5.2.3 [^{12}C(0_2^+)-^{12}C(0_2^+)]-α

These events arise from of the detection of three alpha particles in each detector. The ^{12}C(0_2^+) nuclei are re-built using the two body re-construction technique, Section 2.4.1. Plotting the Q_3 for these events, shown in Figure 5.9, it is found that although the statistics are low, no background subtraction is needed.

As before there are two possible resonant particles that could result in this final state. These are ^{12}C(0_2^+)-α and ^{12}C(0_2^+)-^{12}C(0_2^+), corresponding to ^{16}O* and ^{24}Mg* respectively. The relative energy spectra calculated for these two possibilities are shown in Figure 5.10. The ^{12}C(0_2^+)-α relative energy is plotted for each ^{12}C(0_2^+) since it is not possible to distinguish between them. The sharp cutoff in the ^{12}C(0_2^+)-^{12}C(0_2^+) relative energy spectrum at high energy is due to a kinematic effect, the level of this cut-off is seen to increase as the beam energy increases.

No peaks are observed in either spectrum. However a comparison between the ^{12}C(0_2^+)-^{12}C(0_2^+) relative energy spectrum and the excitation function from the reaction ^{12}C+^{12}C $\rightarrow$ ^{12}C(0_2^+)+^{12}C(0_2^+) in the excitation energy region around 46.4 MeV in ^{24}Mg [Wuo 92], Figure 5.10b, shows some similarities. These similarities may be evidence that a ^{28}Si chain state is being observed decaying through the ^{24}Mg chain.

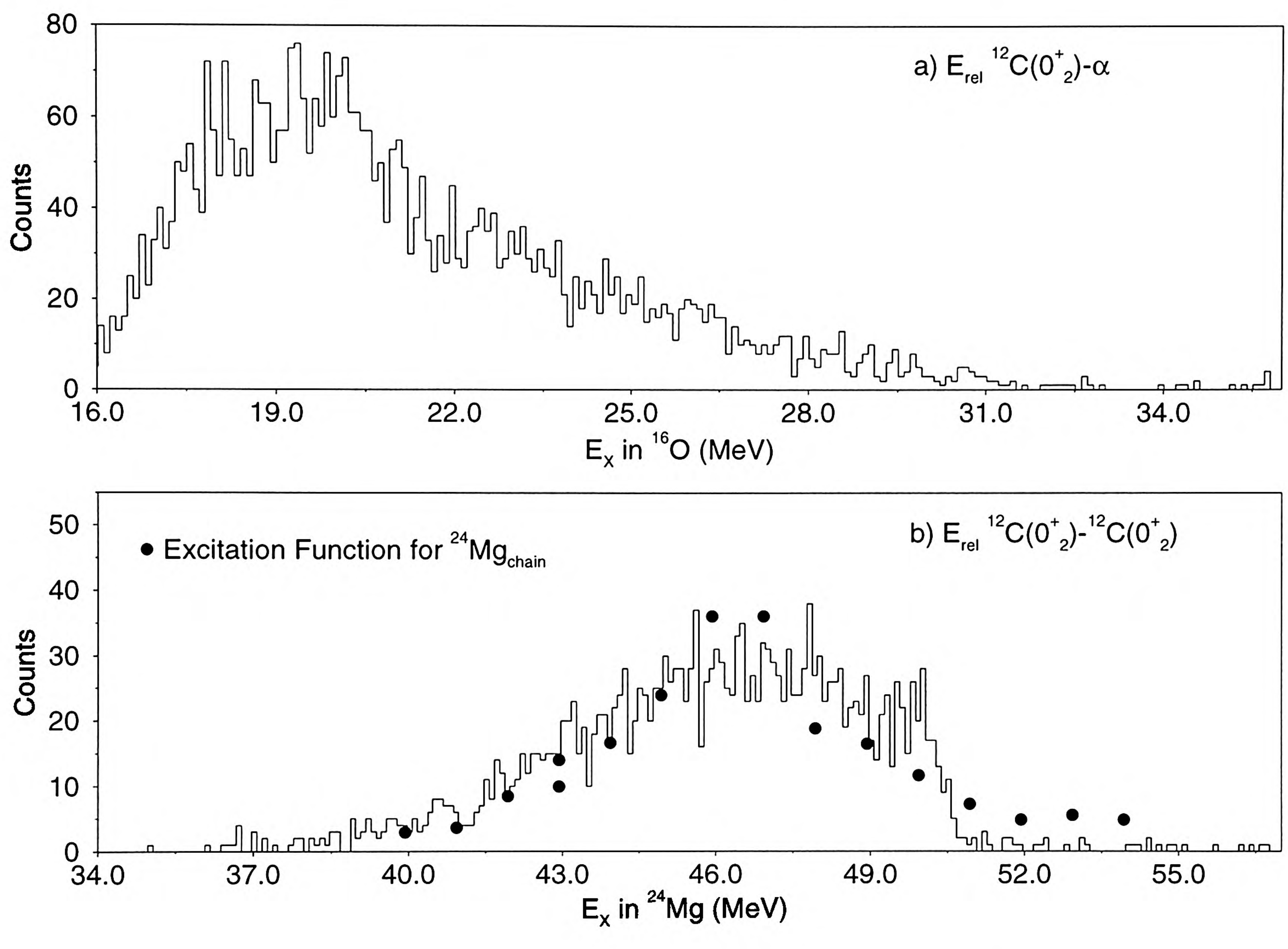

Figure 5.10: *The excitation energy of the resonant nucleus calculated at $E_{c.m.}$=37.7 MeV, assuming the resonant particle decay fragments to be either a) $^{12}C(0_2^+)$-α or b) $^{12}C(0_2^+)$-$^{12}C(0_2^+)$, for $^{12}C(0_2^+)$-$^{12}C(0_2^+)$ events. The excitation energy assuming a ^{24}Mg resonant particle, calculated from the $^{12}C(0_2^+)$-$^{12}C(0_2^+)$ relative energy, is compared with the excitation energy function for the ^{24}Mg chain state, from Reference [Wuo 92].*

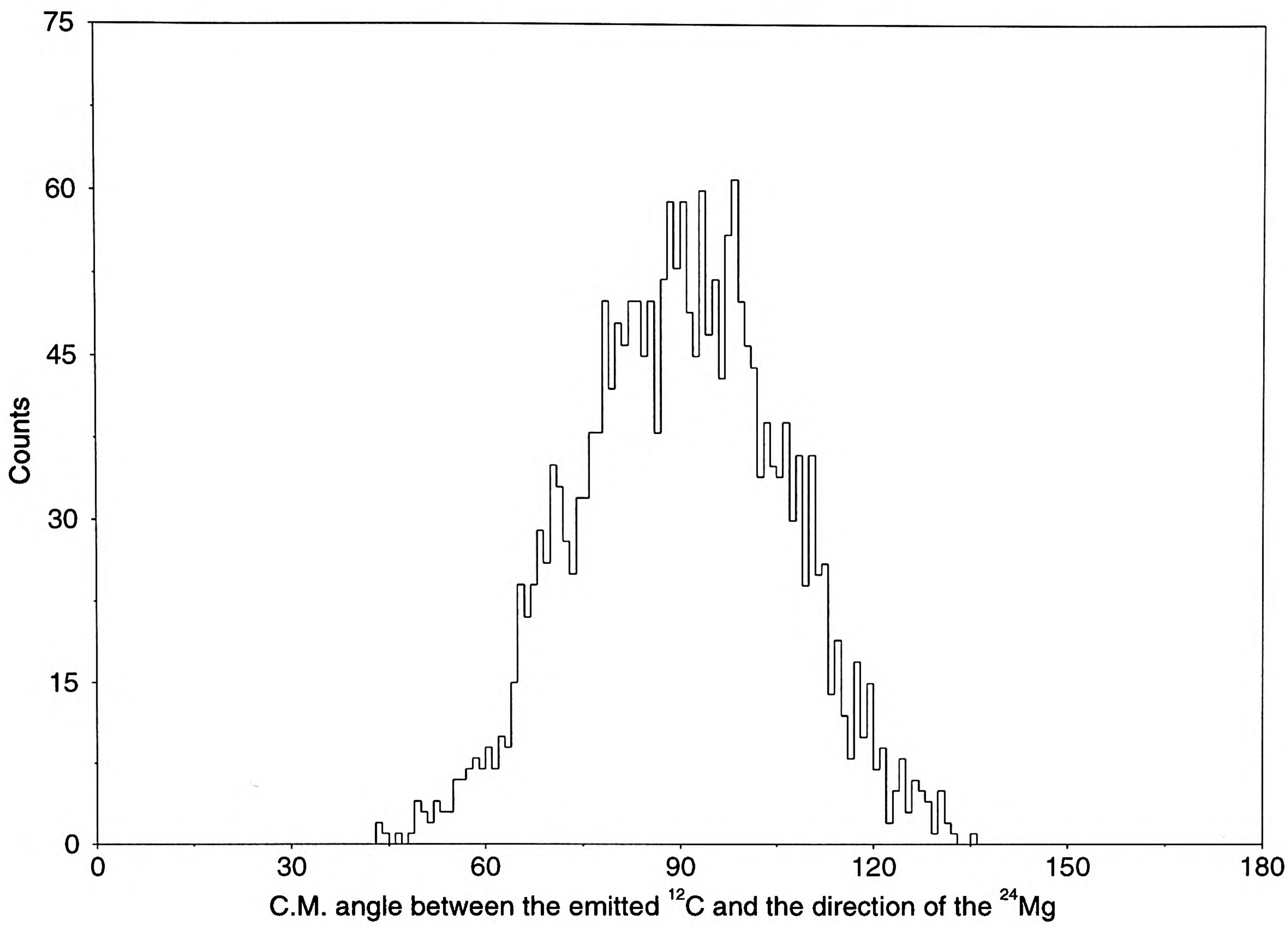

Figure 5.11: *The angle between either of the emitted ^{12}C nuclei relative to the decaying ^{24}Mg, in the centre of mass.*

This effect may arise because the undetected alpha particle effectively produces a sweep across many energies so that the whole ^{24}Mg excitation function in this region is sampled at the same time. To further test this hypothesis, the angle of breakup of the two ^{12}C's relative to the direction of their parent nucleus in the centre of mass was calculated for each event and histogrammed, see Figure 5.11. Again by comparison with the ^{12}C+^{12}C scattering data, we expect a sharp peak at $\theta^*=90°$. Instead the angular distribution contains only a broad peak at $\theta^*=90°$ whose width is too large to be associated with the ^{24}Mg chain state.

The yield for the $^{12}C(0_2^+)$-$^{12}C(0_2^+)$-α final state is shown in Figure 5.12 from each experiment. They have been normalised at $E_{c.m.}$=44.1 MeV. Overall it can be seen that the excitation functions are smooth, rising only slowly with energy. However, there are some significant discrepancies between the experiments. Both the experiments performed at the NSF contain enhancements of the yield at $E_{c.m.}$=43.3 MeV. In addition there is disagreement between the NSF and ANU experiments towards lower energy. It can be seen that the enhancement at $E_{c.m.}$=43.3 MeV observed in the NSF data would not be significant without the accompanying sharp drop off at lower energy and would be consistent with the ANU results. Therefore it is this low

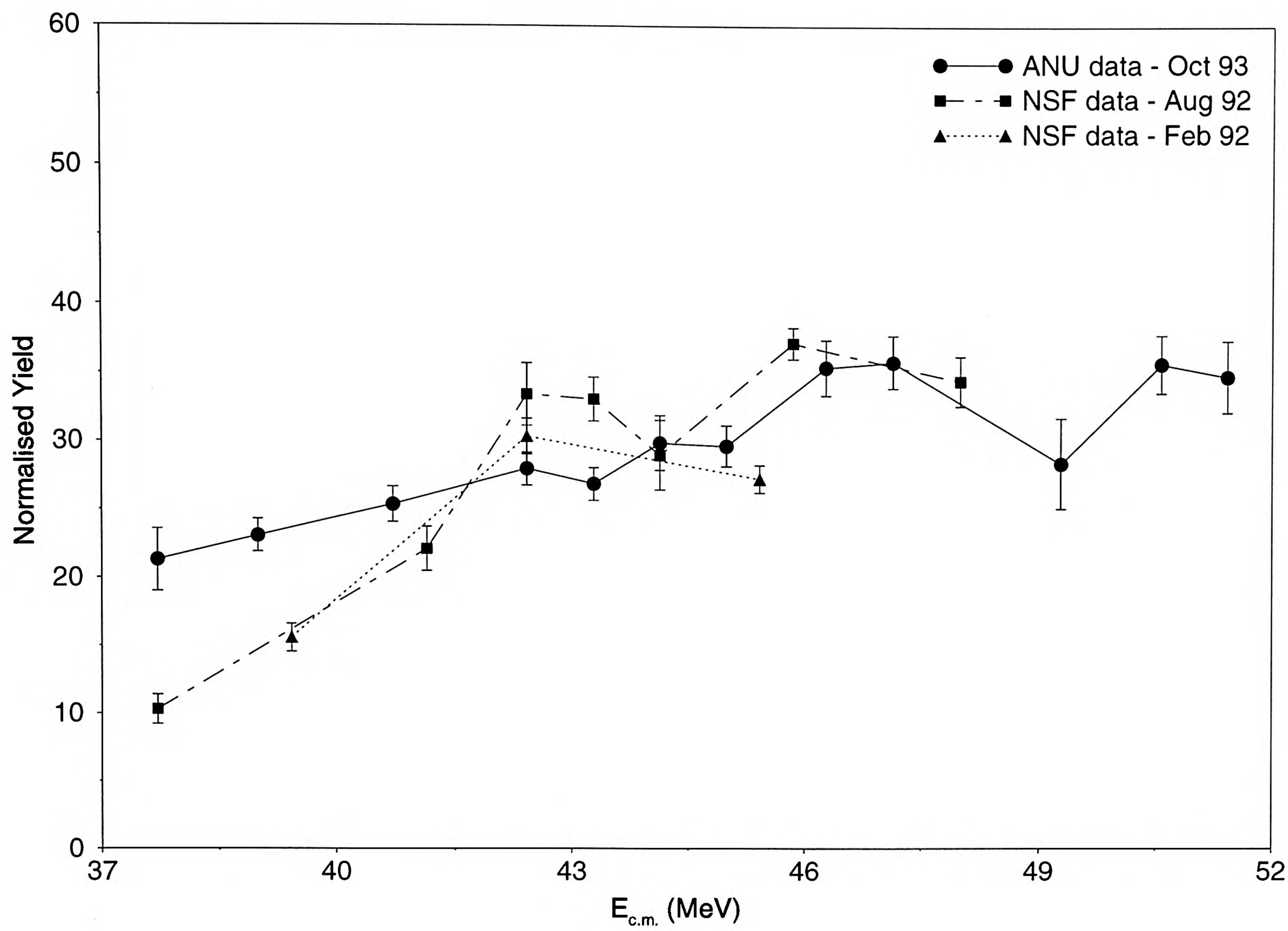

Figure 5.12: *The $^{12}C(0_2^+)$-$^{12}C(0_2^+)$ yield as a function of energy.*

energy discrepancy that has been examined in more detail.

All of the differences that could be identified between the experiments performed at the NSF and at the ANU have been examined. Within the chamber, the main difference was the distance between the detectors and the target. It was necessary to place the detectors further from the target at the ANU and this resulted in a smaller solid angle coverage. To compensate for this in the off-line analysis, the detector coverage in the NSF experiments was reduced using software gates. This had no effect on the slope of the excitation functions. The energy thresholds for each strip on each detector were compared to ensure that they were the same for all experiments. Plotting θ^* against ψ for each experiment found them to have the same θ^*-ψ coverage. In addition, the ANU data has been independently analysed by M. Freer [Fre 94] in an attempt to trace this systematic error. His analysis agrees with these described herein.

It is therefore thought that the higher yield at low energy at the ANU is a result of the change in the trigger logic. In the second experiment at the NSF the trigger logic was changed during the experiment to examine this effect. The multiplicity condition was changed from m=2 in each detector to m=4 between both detectors. The resulting variation in the yield is shown in Figure 5.13. It can be seen that with

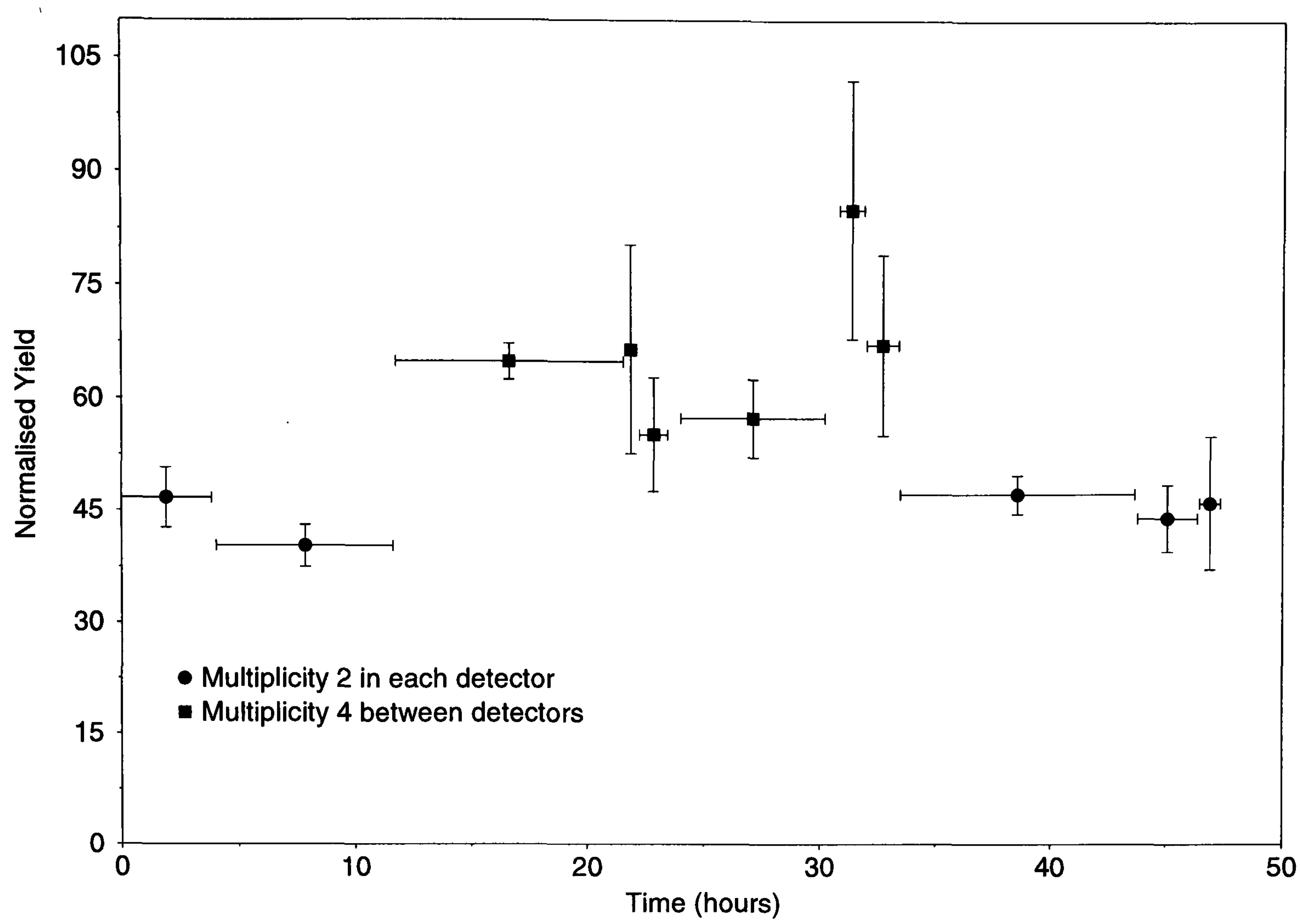

Figure 5.13: *The $^{12}C(0_2^+)$-$^{12}C(0_2^+)$ yield for two different multiplicity conditions at $E_{c.m.}$=43.3 MeV. The horizontal bars denote the length of each run.*

the multiplicity set to m=4 between both detectors the yield rises. This is as we would expect from comparisons between the NSF and the ANU data. Unfortunately this effect was only tested at one energy, $E_{c.m.}$=43.3 MeV, so that it is not known whether the size of the effect changes with energy. Since it is therefore likely that the effect that is seen between experiments is a trigger error, then this can only deplete events - it cannot create them. This increases the trust placed in the ANU data.

Accordingly, the better statistics and higher resolution from the ANU data lead us to conclude that the observation of an enhancement in the NSF data was not significant.

5.2.4 Efficiency Corrections and Differential Cross-Sections

In order to compare these data with the data from other reactions, the differential cross-sections must calculated. This has been performed for the Q_3=-22.5 MeV peak seen with the detection configurations [^{8}Be-^{12}C(0_2^+)]-^{8}Be and [^{12}C(0_2^+)-^{12}C(0_2^+)]-α. First the efficiencies for the detection of the ^{8}Be and the ^{12}C(0_2^+) were calculated and folded into the Q_3 spectra using the method described in Section 2.5.2 and

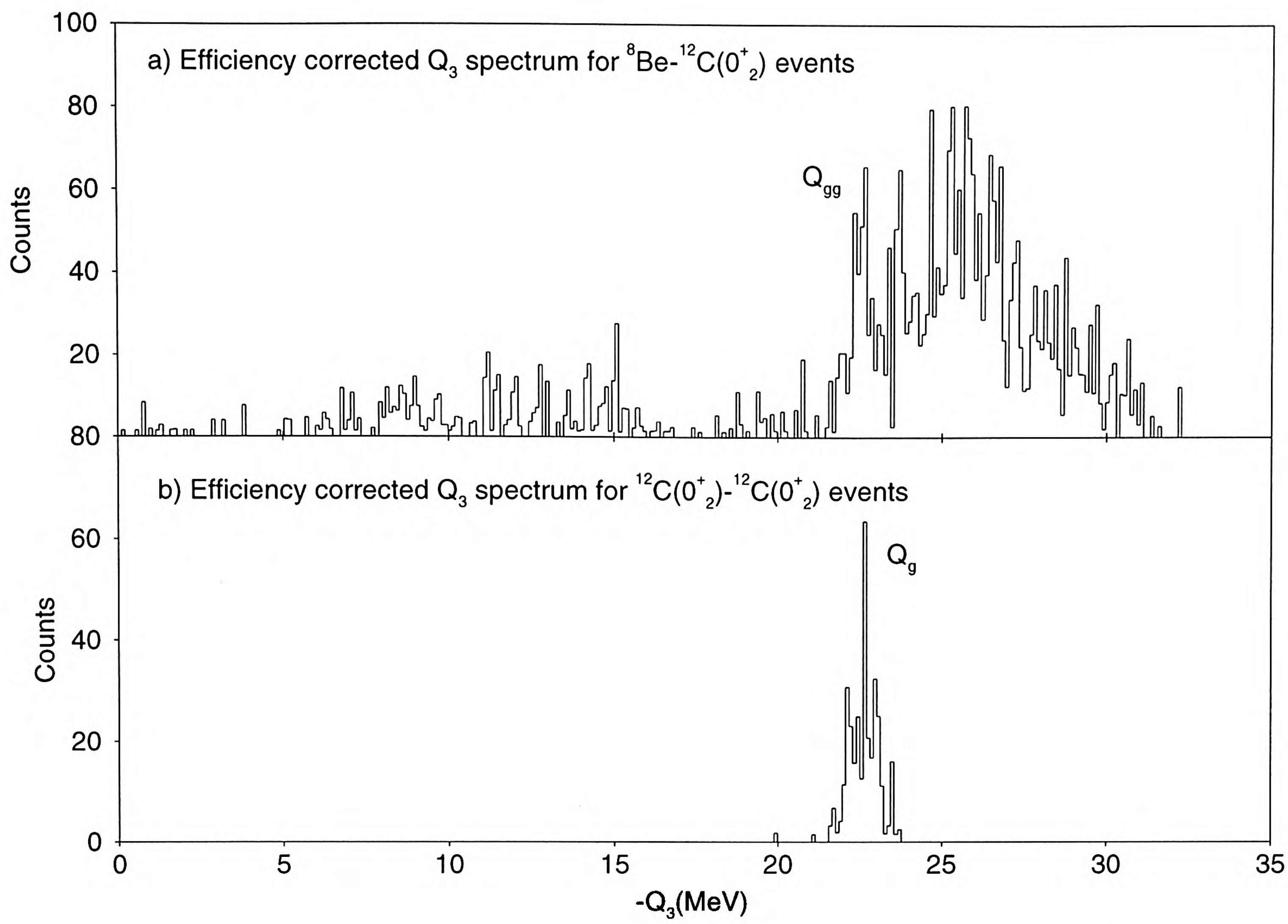

Figure 5.14: *The efficiency corrected Q_3 spectra at $E_{c.m.}$=37.7 MeV for a) ^{8}Be-^{12}C(0_2^+) and b) ^{12}C(0_2^+)-^{12}C(0_2^+) events.*

Appendix A. Particles hitting the detector at positions where the efficiency for their detection had been calculated to be less than 0.1 were discarded. The resulting efficiency corrected Q_3 spectra are shown in Figure 5.14.

The Q_3=-22.5 MeV peak in these spectra was integrated for both final states at each energy. The resulting efficiency corrected yields were then converted in to cross-sections using equation 2.15. The cross-sections are shown in Figure 5.15 for the ANU data only. It can be seen that as expected the efficiency corrections make no difference to the overall shape of the excitation functions. The cross-section for the ^{8}Be-^{12}C(0_2^+)-^{8}Be final state is calculated without background subtraction. Comparing these cross-sections with those for the ^{24}Mg chain state [Wuo 92], shown in Figure 1.2, it can be seen that the cross-sections for the final states from this reaction are an order of magnitude lower.

5.3 Other Final States in the ^{16}O+^{12}C Reaction

In the previous section the results from the search for a seven-alpha chain state decaying to a seven body final state were presented. Although the absence of par-

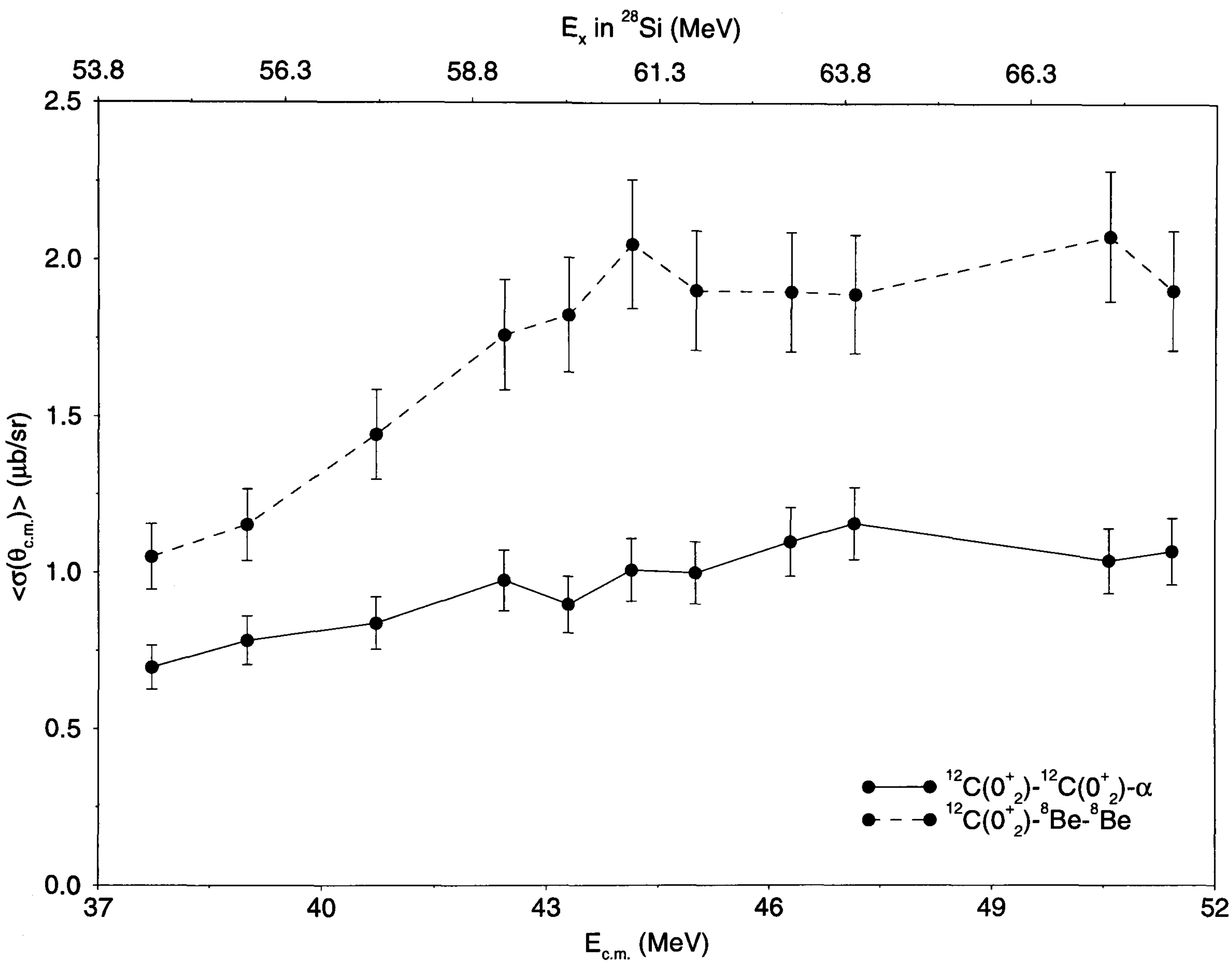

Figure 5.15: *The cross-sections for the detection of $^{12}C(0_2^+)$-$^{12}C(0_2^+)$ and ^8Be-$^{12}C(0_2^+)$.*

ticle identification precludes the examination of most other final states, it does not exclude them all. In these experiments nuclei can only be identified from their breakup fragments, when these breakup fragments consist only of alpha particles. If these alpha particles are detected in only one detector, with nothing detected in the other detector, then this is referred to as a singles event. From Section 2.4.2 we have seen that in this case the kinematic properties of the undetected nucleus can be calculated. In this manner several other reaction channels can be studied. These channels take the form [^{8}Be]-^{20}Ne*, [^{12}C*]-^{16}O* and [^{16}O*]-^{12}C*, where the square brackets identify the detected nucleus. The detected nuclei decay to alpha particle final states. These channels are analogous to the ^{8}Be$_{(g.s.)}$+^{16}O$_{(g.s.)}$ [Ali 94], ^{12}C(0_2^+)-^{12}C(3^-) [Cha 95a] and α-^{20}Ne* [Mir 94] final state channels studied in ^{12}C-^{12}C scattering which are seen to have similar characteristics to the ^{12}C(0_2^+)-^{12}C(0_2^+) resonance that has been associated with the ^{24}Mg chain state [Mar 86, Wuo 92]. It might therefore be expected that, if a ^{28}Si chain is being observed, then its signature should be seen in these singles channels. These final states have been analysed and the results are presented below. It will be noticed that the Q-value resolution is significantly better than for the seven-alpha final state. This is because there are fewer nuclei detected in a singles event and therefore fewer factors contributing to the error.

5.3.1 [^{8}Be]-^{20}Ne*

Analysis of these channels involves the detection in a single detector of the two alpha particles resulting from the decay of an ^{8}Be. The ^{8}Be is re-built using the Q-value method described in Section 2.4.2. Now, knowing all of the kinematic properties of the ^{8}Be, the kinematic properties of the undetected nucleus can be calculated. The excitation energy of the undetected nucleus will in general be below the threshold for particle decay and therefore any excitation levels observed can be attributed to ^{20}Ne. The calculated excitation spectrum is given in Figure 5.16 for a centre of mass energy of 37.7 MeV. In all, 14 excited states plus the ground-state can be identified at excitation energies up to 22 MeV. Table 5.1 lists the measured energies for each state and their measured differential cross-sections. It also lists the most likely energy and spin assignments for these states in ^{20}Ne from [Ajz 70].

Several other studies of the reaction ^{12}C(^{16}O,^{8}Be)^{20}Ne* have been made of which the most closely related to this study is that by M.A. Eswaran et al. [Esw 93] at the Bhabha Atomic Research Centre, Bombay, India. They studied the reaction up to

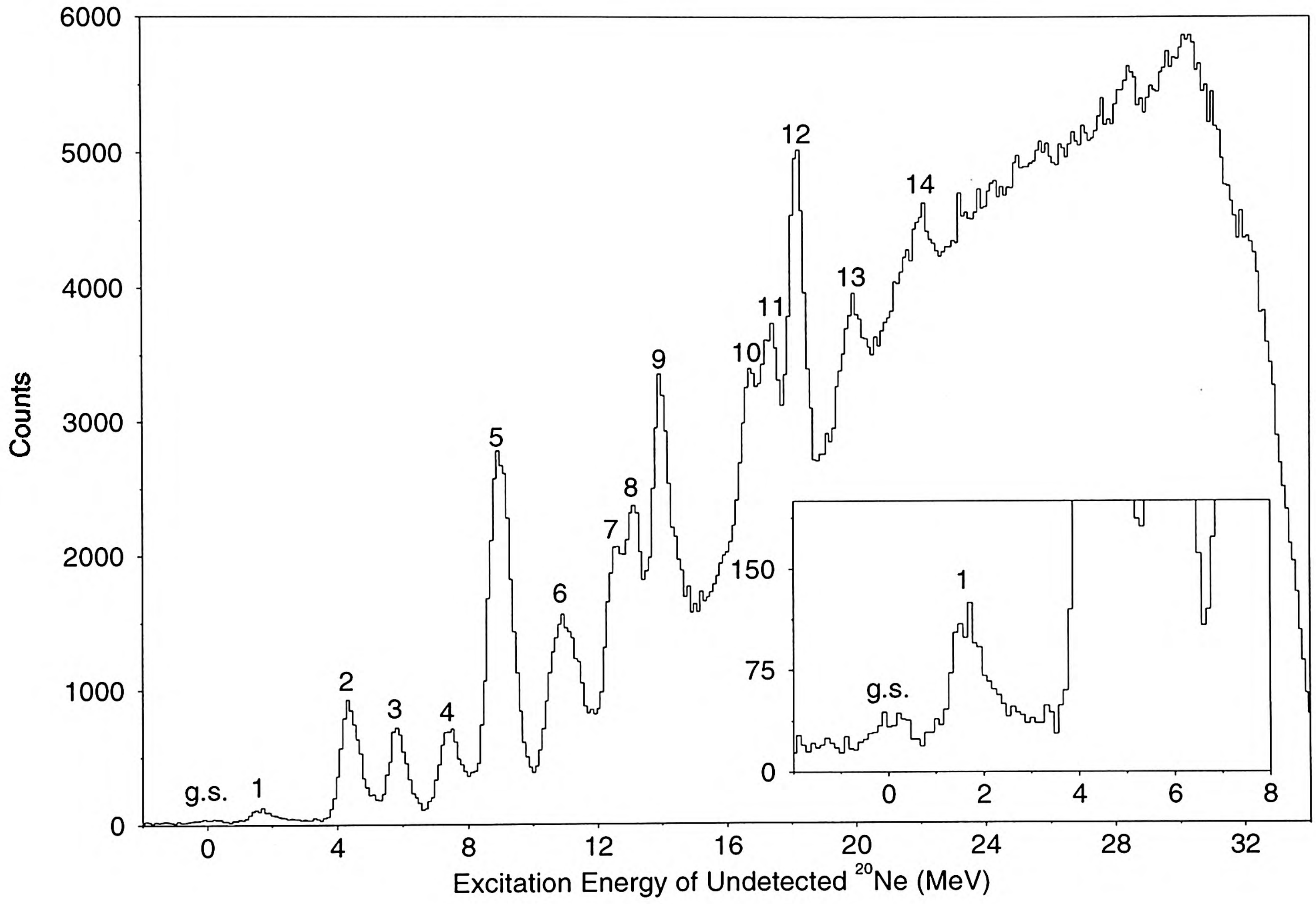

Figure 5.16: *The excitation energy spectrum at* $E_{c.m.}$*=37.7 MeV for the undetected* ^{20}*Ne in the* $^{12}C(^{16}O,^{8}Be)^{20}Ne$ *reaction. The energies of the levels are given in Table 5.1.*

Peak Number	Measured Centroid (MeV±keV)	Level in ^{20}Ne (MeV±keV)	Spin Assignment	Differential Cross-Section (μb/sr)
g.s.	0.0 ± 63	0.0	0^+	3.5 ± 0.7
1	1.641 ± 84	1.633674 ± 0.015	2^+	12 ± 4
2	4.225 ± 67	4.2477 ± 1.1	4^+	52 ± 7
3	5.793 ± 69	5.7877 ± 2.6	1^-	38 ± 7
4	7.165 ± 70	7.1563 ± 0.5	3^-	36 ± 10
5	8.943 ± 66	8.7776 ± 2.2	6^+	178 ± 37
6	10.509 ± 72	10.262 ± 5	5^-	96 ± 24
7	12.063 ± 78	11.951 ± 4	8^+	49 ± 10
8	12.624 ± 79	12.585 ± 5	6^+	49 ± 10
9	13.906 ± 77	13.928 ± 5	6^+	105 ± 21
10	16.111 ± 88	15.874 ± 9	8^+	80 ± 16
11	16.750 ± 86	16.581 ± 15	7^-	64 ± 13
12	17.719 ± 72	17.295 ± 15	8^+	123 ± 25
13	19.799 ± 81	19.884 ± 40	7^-	36 ± 8
14	21.778 ± 98	21.062 ± 6	9^-	34 ± 7

Table 5.1: *The energies and assigned levels for the numbered peaks in Figure 5.16. The differential cross-sections were measured at* $E_{c.m.}$*=37.7 MeV.*

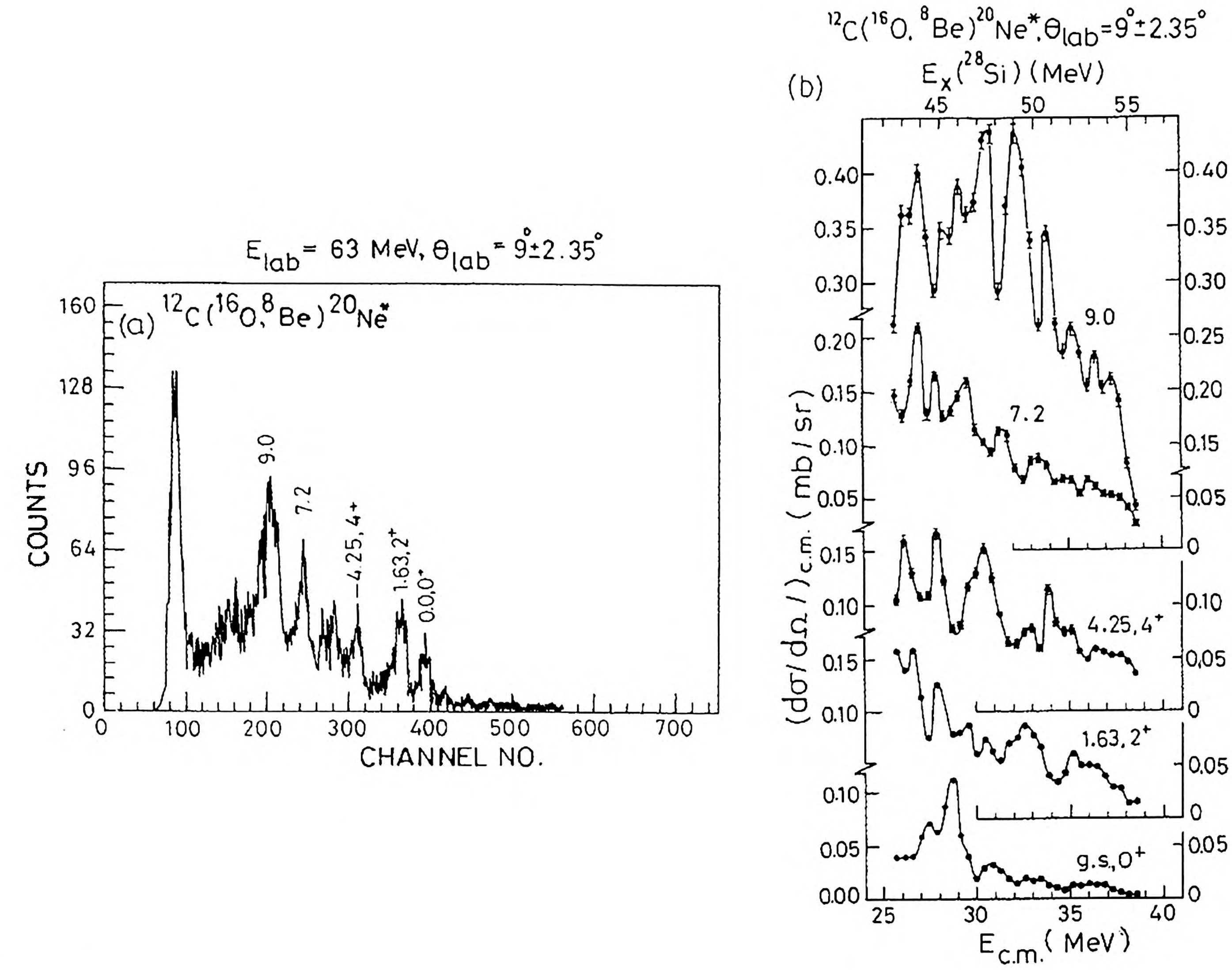

Figure 5.17: *a) The excitation energies and b) excitation functions for the reaction* $^{12}C(^{16}O,^{8}Be)^{20}Ne$ *taken from [Esw 93].*

a centre of mass energy of 38.6 MeV, thus overlapping with this experiment. They found ^{8}Be groups leading to $^{20}Ne_{g.s.}$, 1.63 MeV (2^+), 4.25 MeV (4^+), 7.2 MeV and 9 MeV however their resolution was poor, see Figure 5.17a. They were able to measure the excitation function for these states over the energy range $E_{c.m.}$=25.7 MeV to 38.6 MeV, shown in Figure 5.17b, and found evidence for structure throughout this energy range. They observed a sharp drop in the cross-section towards the higher energies where their study overlaps with our data.

Cross-sections have been calculated for all of the ^{8}Be-^{20}Ne* final state channels seen in this experiment. As well as extending the knowledge of these excitation functions up in energy, these measurements also provide a normalisation check for other cross-sections calculated. In order to calculate the cross-sections, the value for the ^{8}Be detection efficiency was taken to be 0.75. The rapidly falling cross-sections in these channels meant that it was not possible to measure the cross-section over the whole energy range and indeed in some channels it was only possible to measure the cross-sections at $E_{c.m.}$=37.7 MeV. The differential cross-sections for all excitation energies at $E_{c.m.}$=37.7 MeV are given in the last column of Table 5.1. The excitation functions for the six lowest excited states in ^{20}Ne are plotted in Figure 5.18.

Comparing the cross-sections from this experiment with those obtained by M.A. Eswaran et al., shown in Figure 5.17b, it can be seen that the agreement is very good. This gives more confidence that the cross-sections for the seven-alpha channels, calculated in Section 5.2.4, are accurate. The sharp fall in the cross-sections between the centre of mass energies 37.7 MeV and 39 MeV in the ANU data seems to correspond to a similar fall in the cross-sections measured by M.A. Eswaran et al. Otherwise no significant structure is seen in these channels.

5.3.2 [^{12}C*]-^{16}O*

These final state channels involve the detection of the ^{12}C in either the 0_2^+ state at 7.65 MeV or the 3^- state at 9.6 MeV. Both of these states decay via ^{8}Be+α resulting in a three alpha final state. The three alpha particles are detected in a single detector and rebuilt using the method described in Section 2.4.2. The kinematic properties of the undetected ^{16}O can be calculated and its excitation energy histogrammed. One of the resulting spectra is shown in Figure 5.19.

Three peaks are observed above the ground-state peak. These lie at ~6.5 MeV, ~10.8 MeV and ~15.3 MeV. Although no other ^{12}C(^{16}O,^{12}C*)^{16}O* experiments have been performed, the identification of these states may be aided by the comparison with the data from the ^{12}C(^{16}O,^{12}C)^{16}O* reaction performed by K. Katori et al. [Kat 80] using the 12UD Pelletron at the University of Tsukabu, Japan. Their energy resolution was about 70 keV on a self supporting natural carbon foil of 29 μg/cm^2 thickness. This resolution was sufficient to separate the transitions within the peaks we see at 6.5 MeV and 10.8 MeV. They identified transitions to the states at 6.049 MeV (0^+), 6.131 MeV (3^-), 6.919 MeV (2^+) and 7.117 MeV (1^-) within the region around 6.5 MeV and to states at 10.353 MeV (4^+) and 11.095 MeV (4^+) in the 10.8 MeV region. The higher energy region was not examined. These observations agree well with this current data, suggesting that the transitions seen are the same between the two experiments.

There is no data with which to compare the 15.3 MeV peak. There are a number of possible candidates in this excitation energy region with spin assignments of 6^+ and 5^- [Til 93]. All of these assignments are summarised in Table 5.2.

There have been no ^{12}C(^{16}O,^{12}C*)^{16}O* experiments with which the cross-sections for these final state channels may be compared. Therefore only the beam normalised yields have been calculated for these channels, these are shown in Fig-

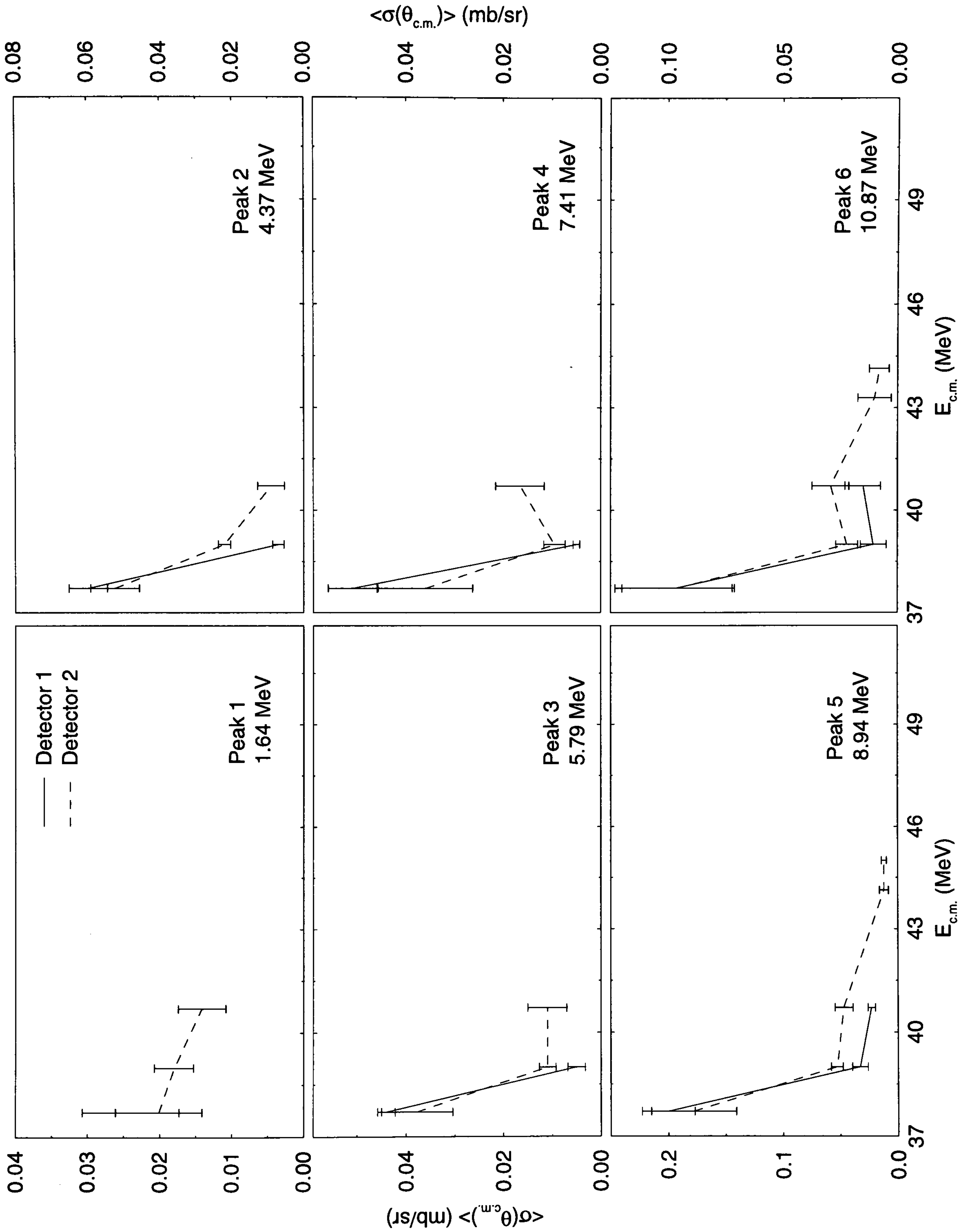

Figure 5.18: *Cross-sections for some of the final state channels in the $^{12}C(^{16}O,^{8}Be)^{20}Ne^{*}$ reaction.*

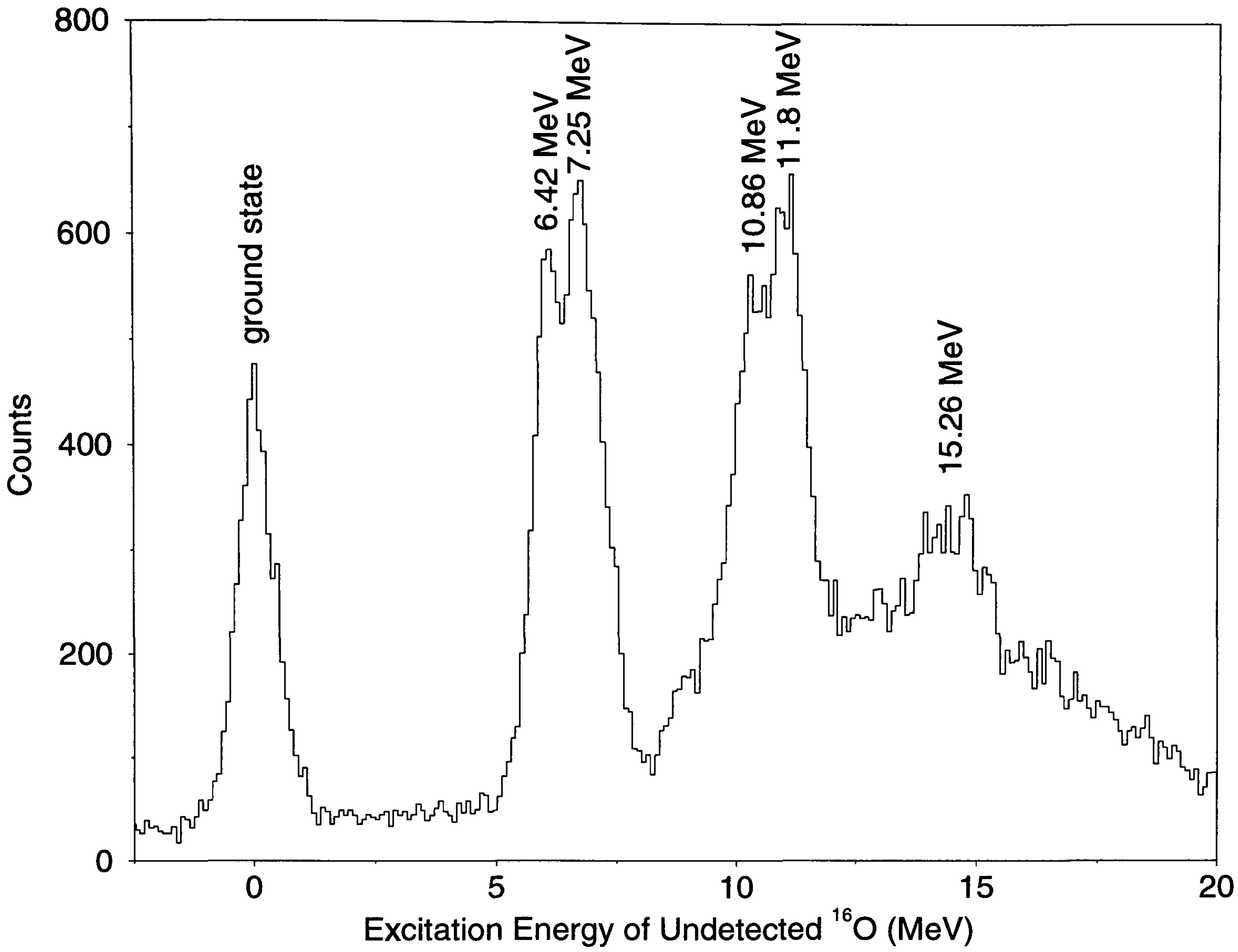

Figure 5.19: *The excitation energy spectrum at $E_{c.m.}$=37.7MeV for the undetected ^{16}O nucleus in the $^{12}C(^{16}O,^{12}C^*)^{16}O^*$ reaction.*

Measured Centroid (MeV)	Assigned Level in ^{16}O (MeV±keV)	Spin Assignments from Reference [Til 93]
0.0 ± 0.03	0.0	0^+
6.418 ± 0.062	6.0502 ± 1.0, 6.13066 ± 0.18	0^+, 3^-
7.245 ± 0.073	6.9188 ± 0.6, 7.11867 ± 0.35	2^+, 1^-
10.857 ± 0.086	10.353 ± 4	4^+
11.78 ± 0.076	11.096 ± 3	4^+
15.422 ± 0.077	14.7 ± 11, 14.8 ± 2, 16.3 ± 7	(5^-, 6^+, 6^+)

Table 5.2: *The transitions calculated for the undetected ^{16}O. See the text for a full discussion of these assignments.*

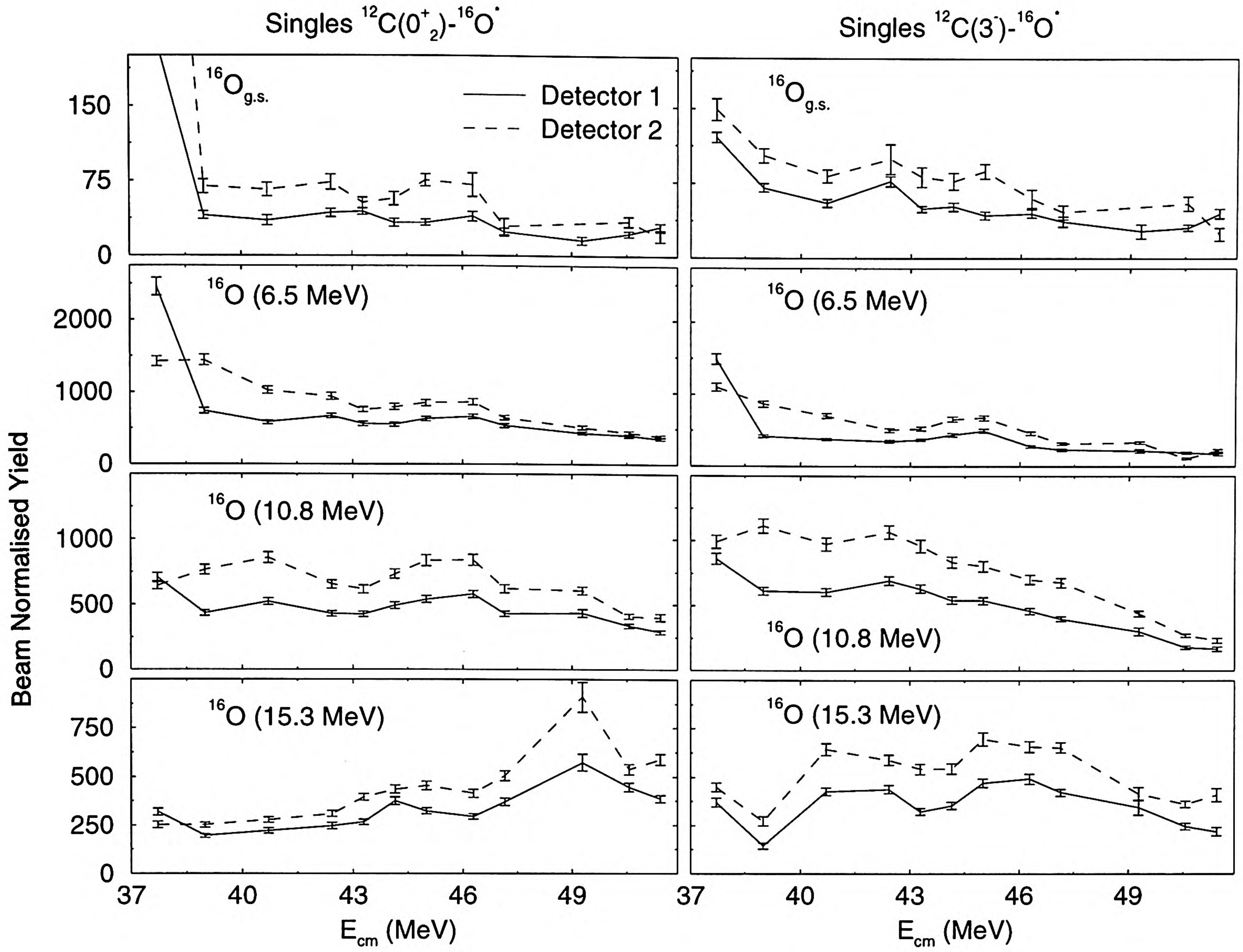

Figure 5.20: *The beam normalised yields for the final state channels observed in the* $^{12}C(^{16}O,^{12}C^*)^{16}O^*$ *reaction.*

ure 5.20. Generally the yield in all channels is constant with energy. The higher yield from detector 2 is a result of that detector being closer to the target and therefore subtending a larger solid angle. The enhancement of the yield in the $^{12}C(0^+_2)$-^{16}O(15.3 MeV) final state channels at a centre of mass energy of 49 MeV probably results from a statistical fluctuation. Much of the data at this energy was lost due to a tape being erased in transit. The small amount of data remaining at this energy results in very poor statistics.

There is a sharp rise in the yield at a centre of mass energy of 37.5 MeV for the $^{12}C(0^+_2)$-$^{16}O_{g.s.}$ final state and to a lesser extent in the $^{12}C(0^+_2)$-^{16}O (6.050 MeV, 0^+) final state yield. Only a small effect is seen in the corresponding 3^- channels and no effect is seen in the reaction channels in which the ^{16}O is at a higher excitation energy. The angular distributions at this energy have been calculated, and do not contain the expected enhancement at $\theta^*_{c.m.}$=90°, indicating that this rise cannot be attributed to the excitation of the chain state. The possibility that this rise forms part of a strong resonance cannot be ruled out due to the absence of data below this energy, however it seems more likely that this is a kinematic effect caused by the ADC energy threshold at 40 MeV. Computer simulations have shown that the energies of the alpha particles from the decay of the ^{12}C nuclei are very close to the upper energy threshold within the ADC. At the higher beam energies this threshold prevents the detection of one or more of the alpha particles that result from the breakup of the $^{12}C^*$, hence causing a sharp drop in the detected yield. This effect would not be present in the seven alpha data because in that case the alpha particles are of a much lower energy, well below this energy threshold.

Overall the excitation functions for these final state channels are flat. They contain no signature for a ^{28}Si chain state.

5.3.3 [$^{16}O^*$]-$^{12}C^*$

At first sight, these final state channels would seem to be the same as the ones above. However now, because the detected particles must be alpha particles, these states in ^{16}O are at much higher energies, above the threshold for particle breakup. The Q-value re-construction method, described in Section 2.4.2, is used to rebuild all multiplicity 4 singles events. It is not necessary to differentiate between alpha particles from the ^8Be-^8Be and $^{12}C(0_2^+)$-α decay channels using this method. The resulting ^{16}O excitation spectrum is shown in Figure 5.21a. Unlike the re-constructed ^8Be and ^{12}C nuclei, no structure is seen in this spectrum.

The excitation energy of the undetected nucleus can be calculated and histogrammed for each event, shown in Figure 5.21b. Contributions are observed from the ^{12}C ground state and the 4.44 MeV (2^+) state, as well as a strong contribution from other, unidentified, events. The efficiency for detection of all four alpha particles from the decay of the $^{16}O^*$ is low and a method is required to extract these events from the high background. Since there is no particle identification, the only identifiable ^{16}O decay channels are ^8Be-^8Be and $^{12}C(0_2^+)$-α. The two body event rebuilding technique described in Section 2.4.1 can be applied to all multiplicity four events, in order to identify nuclei from these decay channels. The results of this analysis are given in Table 5.3 for a typical run at $E_{c.m.}$=43.2 MeV.

It can be seen that the majority of multiplicity four events contain either no identifiable nuclei, or a single ^8Be. Many of these events are thought to contain particles lighter than the alpha particle. Of the remaining events, about equal numbers were identified as containing either ^8Be+^8Be or $^{12}C(0_2^+)+\alpha$. For these events, the ^{16}O excitation energy and the excitation energy of the undetected nucleus can be calculated. The resulting spectra are shown in Figure 5.22 from the detection of

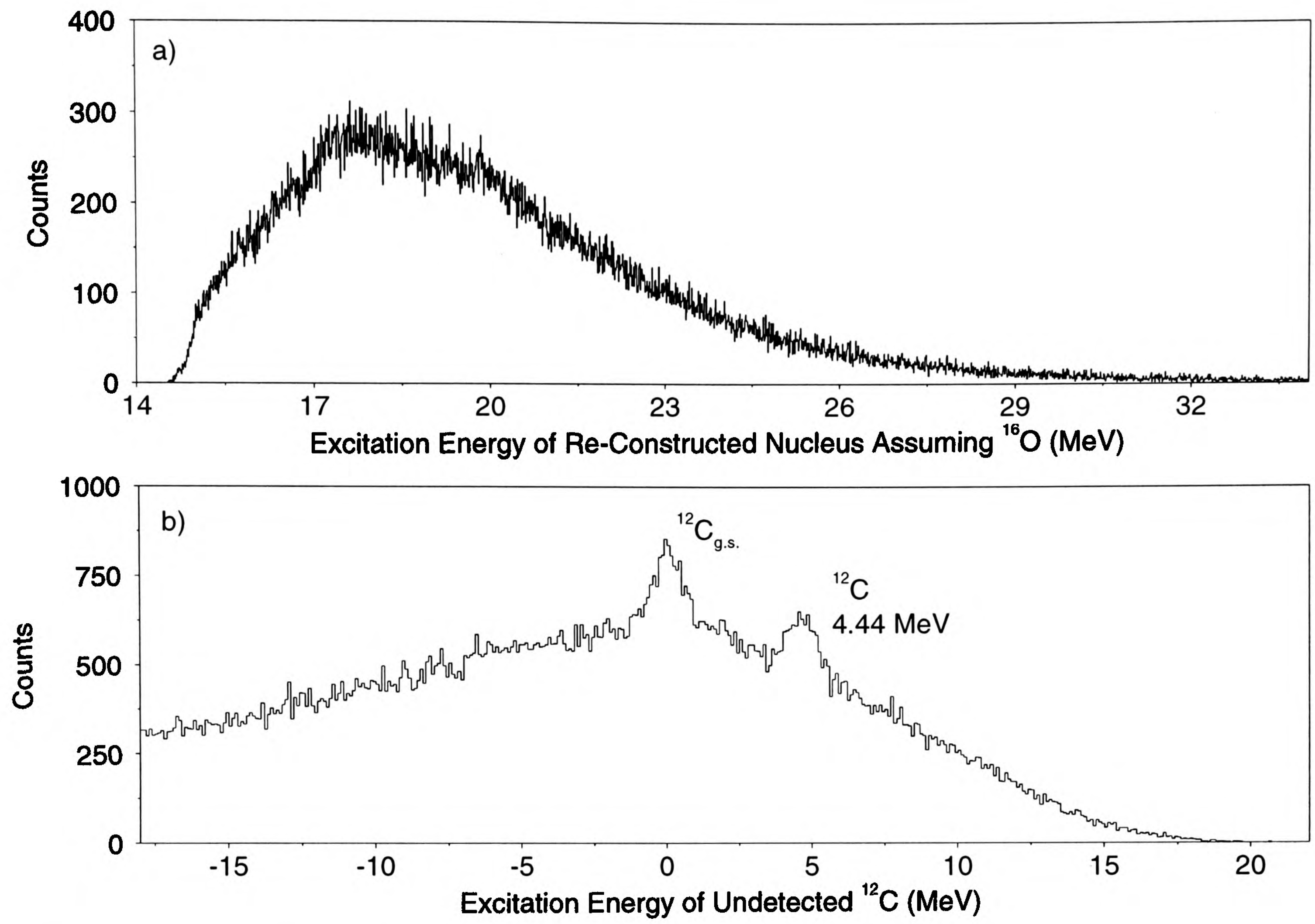

Figure 5.21: *a) The excitation energy spectrum at $E_{c.m.}$=43.3 MeV for multiplicity 4 singles events and b) the excitation energy of the undetected nucleus.*

Number in Event	Count	
	^{8}Be	^{12}C(0_2^+)
0	28596	53021
1	24477	3698
2	3646	-

Table 5.3: *The number of identified ^{8}Be and $^{12}C(0_2^+)$ nuclei from the multiplicity four data at $E_{c.m.}$=43.2 MeV.*

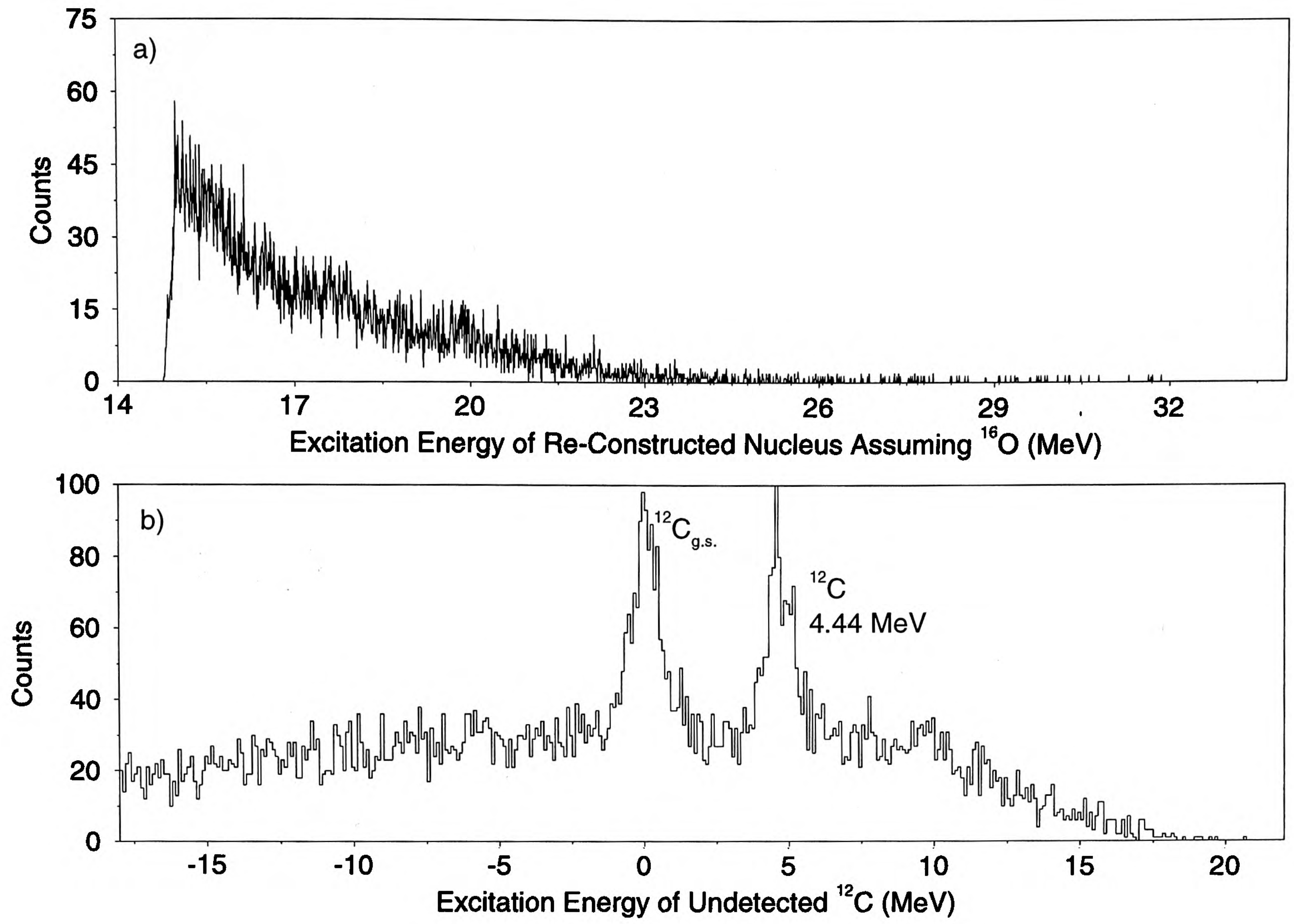

Figure 5.22: *a) The excitation energy spectrum at* $E_{c.m.}$*=43.3 MeV for* $^{12}C(0_2^+)$*-*α *events and b) the excitation energy of the undetected nucleus.*

^{12}C(0_2^+)-α.

The contributions from the undetected ^{12}C nucleus are now much enhanced relative to the background. For each of the ^{12}C levels, the corresponding ^{16}O excitation energies can be calculated and histogrammed. These spectra are shown in Figure 5.23 for the cases $^{16}O^*\rightarrow^{12}C(0_2^+)+\alpha$ and $^{16}O^*\rightarrow^{8}Be+^{8}Be$. Although the statistics are low, there is tentative evidence for levels at 17 MeV and 20 MeV.

A similar experiment has been performed by M. Freer et al. [Fre 95] specifically to look at these channels in ^{16}O+^{12}C scattering. In that experiment the efficiency for detection of the four particles from the decay of the ^{16}O was enhanced by using two PSSD's positioned adjacent to each other on one side of the beam. This resulted in a significant reduction in the background and a much greater efficiency for the detection of the $^{12}C_{g.s.}$-$^{16}O^*$ and $^{12}C(0_2^+)$-$^{16}O^*$ channels. The ^{16}O nuclei were observed to decay through the ^{8}Be-^{8}Be and $^{12}C(2^+)$-α channels from levels at similar energies to those observed in these experiments. However, although those observations are in agreement with the current data, the lack of statistics prevents a better comparison. The variation of the yield with energy has been measured for these channels and is shown in Figure 5.24. In all cases the yield rises with energy, but contains no

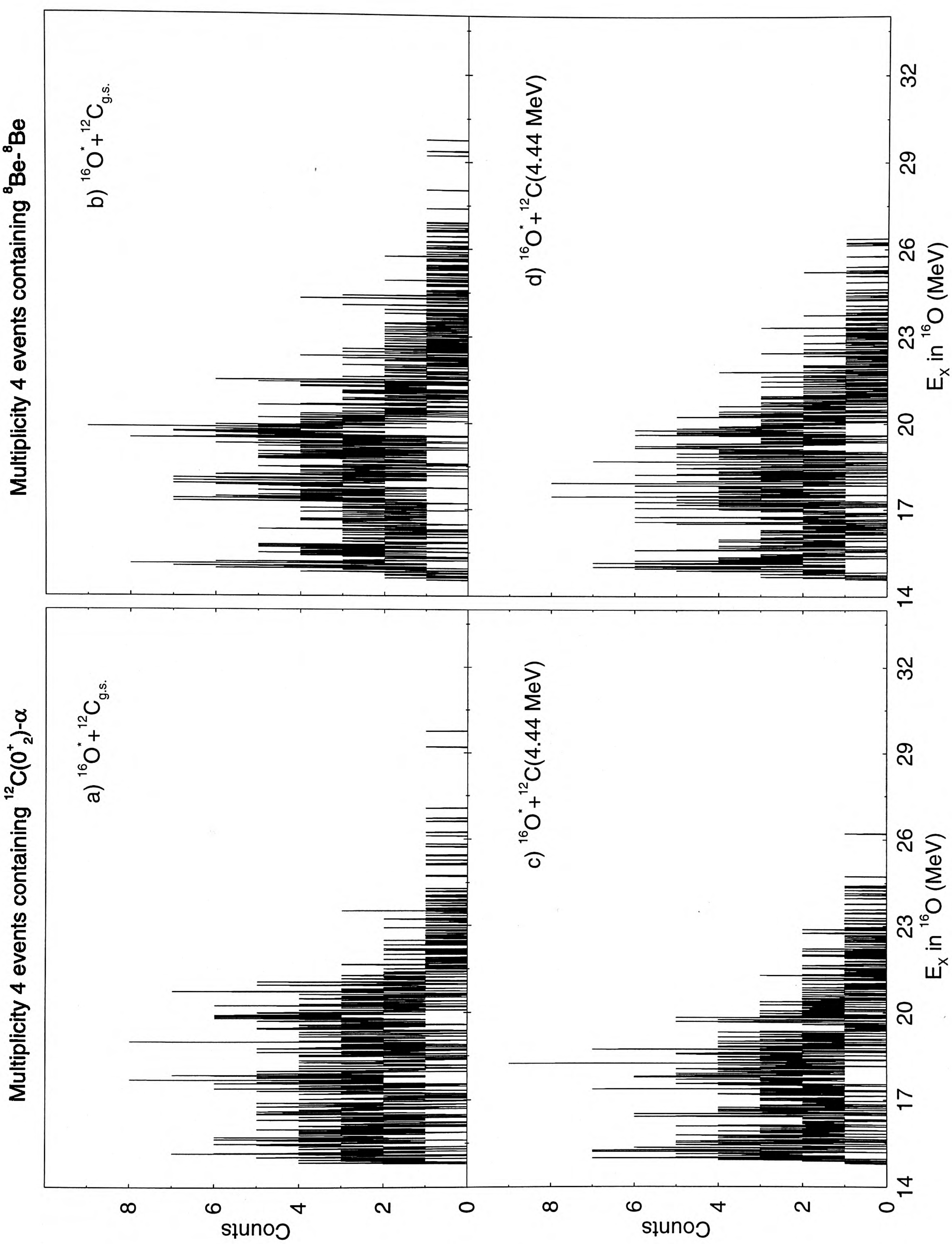

Figure 5.23: *The* ^{16}O *excitation energy spectra from the detection of a) and c)* $^{12}C(0_2^+)$*-*α *and b) and d)* ^{8}Be*-*^{8}Be*, when the undetected* ^{12}C *is in its a) and b) ground state and c) and d)* 2^+ *state.*

significant structure. The rise is most pronounced for the 2^+ level. At the highest energies there was also evidence that the higher excited states in ^{12}C at 7.65 MeV and 9.6 MeV were being excited, however the counts in these channels was too low to allow a measurement of their yields. Thus measurements of the multiplicity four events contain no signature for a seven alpha chain state decaying through $^{16}O^*+^{12}C^*$.

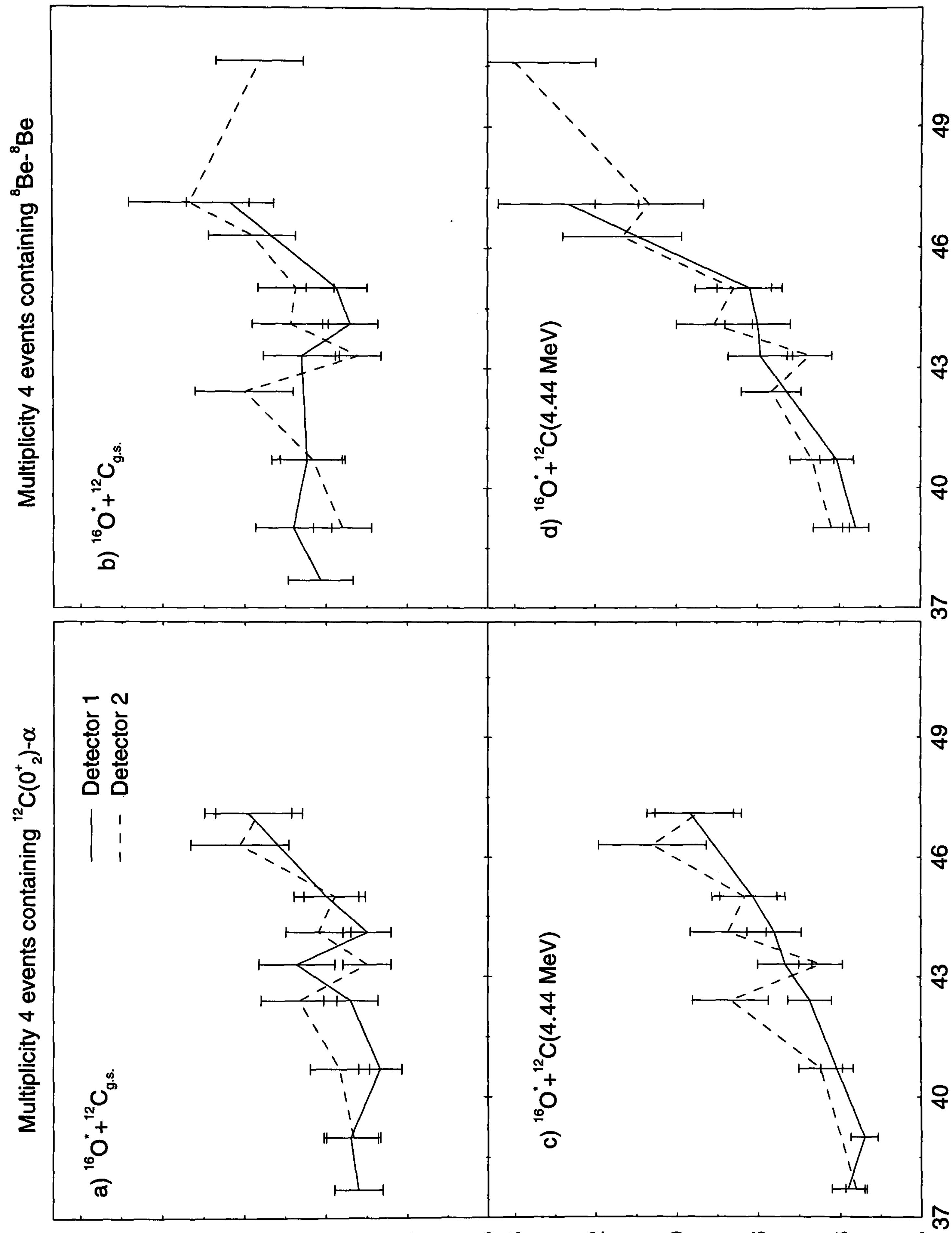

Figure 5.24: *The beam normalised yields for the final state channels observed in the* $^{12}C(^{16}O,^{16}O^*)^{12}C^*$ *reaction.*

Chapter 6

Discussion and Conclusion

In this chapter, the new results obtained from the three experiments will be discussed. A comparison with other investigations will be made in order to see how this new information fits into the overall picture of chain states, which has been developing since this investigation was started. The first sections present an overview of the results obtained from these experiments. Subsequent sections relate these results to the ^{24}Mg chain state data and to theoretical work on chain states.

6.1 Interpretation of the Present Work

This section gives an overview of the work presented in this thesis. It first covers the excitation functions for the various channels observed and then identifies and interprets some of the excited states seen in the singles channels.

6.1.1 Excitation Functions

These three experiments examined the excitation region in ^{28}Si between 54.5 MeV and 68.2 MeV, using the ^{16}O+^{12}C reaction in the search for a seven alpha chain state. The primary identification of a seven alpha chain was expected to be provided by the excitation functions from the final state channels. In particular an enhancement of the yield was expected at an excitation energy of 60.2 MeV [Mer 92] with a width of ~4 MeV in the centre of mass.

The Yield From the $^{12}C(0_2^+)$-$^{16}O_{chain}$ Final State Channel

The experiments were optimised to detect the breakup of the ^{28}Si chain through the $^{12}C(0_2^+)$-$^{16}O_{chain}$ channel with the expectation that this would be the most strongly populated decay channel. Two preliminary experiments were performed at the NSF. Both contained a significant enhancement of the yield at E_x=59.5 MeV in this decay channel, however the statistics were low and the resolution was poor, so that angular distribution measurements could not be made.

A third experiment, performed at the ANU, was expected to provide angular distribution information. However no enhancement of the $^{12}C(0_2^+)$-$^{16}O_{chain}$ final state yield was observed. In addition a significant discrepancy was found in the yield at low energies between the three experiments. The yield from the first two experiments was seen to fall-off sharply while the data from the ANU contained no drop. Without this fall-off in the NSF data, the enhancement at 59.5 MeV was not statistically significant. It is thought that the low energy fall-off arose due to an error in the trigger during the NSF experiments. It was therefore concluded that the yield from the NSF data also contained no significant structure.

These results indicate that no evidence has been found for any resonances in the $^{12}C(0_2^+)$-$^{12}C(0_2^+)$-α or $^{12}C(0_2^+)$-^8Be-^8Be final states with a width in the centre of mass of between 2 MeV and 5 MeV and hence that no evidence for a chain state has been detected decaying through these channels. There is an ambiguity in the choice of the resonant particle in both of these final states, therefore all of the possible combinations in these quasi-three body final states were examined. No evidence was found for excited levels from any of the combinations.

Other Decay Channels

In ^{24}Mg, the cranked alpha-cluster model, used by Marsh and Rae [Mar 86] to predict the six alpha chain state, also predicts a crossing at E_x=46 MeV and L=16 of different bands, built on different bandhead configurations. So it is *a priori* possible that different structures, not necessarily deformed, may contribute to the reaction. Experiments have been performed to examine the $^8Be_{(gs)}+^{16}O_{(gs)}$ [Ali 94], $^{12}C(0_2^+)$-$^{12}C(3^-)$ [Cha 95a] and α-$^{20}Ne^*$ [Mir 94] final state channels. They are all observed to resonate at the same excitation energy as the $^{12}C(0_2^+)$-$^{12}C(0_2^+)$ final state. Angular distributions have been measured for the $^8Be_{(gs)}+^{16}O_{(gs)}$ and $^{12}C(0_2^+)$-$^{12}C(3^-)$ final states and are seen to contain the characteristic enhancement at θ^*_{cm}=90° on resonance.

Similar band crossings are also predicted in ^{28}Si. These occur at L=8, 12, 18 and 20 and $E_x \approx$60 MeV, for different rotational axes of the 2-dimensional alpha-cluster configurations predicted by Zhang and Rae [Zha 93]. It was therefore of interest to

examine other final state channels in $^{16}O+^{12}C$ scattering. The channels examined were ^{8}Be-$^{20}Ne^{*}$, $^{12}C^{*}$-$^{16}O^{*}$ and $^{16}O^{*}$-$^{12}C^{*}$. In addition to probing for a chain state, the cross-sections for ^{8}Be-$^{20}Ne^{*}$ final states have been measured elsewhere [Esw 93] and provide a check on the measured cross-sections for other channels observed.
A number of excited levels were identified in both ^{20}Ne and ^{16}O. The yields for these channels were measured as a function of energy and found to contain no structure. A sharp rise in the yield at 88 MeV beam energy in the $^{12}C(0_2^+)$-$^{16}O_{g.s.}$ and $^{12}C(0_2^+)$-^{16}O (6.5 MeV) final states was interpreted as an artifact introduced by the upper energy threshold within the ADC.
Good agreement was attained between the ^{8}Be-$^{20}Ne^{*}$ final state cross-sections, measured here, and those previously measured, giving confidence that the cross-section measured for the seven alpha final state is correct.

6.1.2 Interpretation of States Seen in the ^{8}Be-^{20}Ne*, ^{12}C*-^{16}O* and ^{16}O*-^{12}C* Final State Channels

^{8}Be-^{20}Ne*

The $^{12}C(^{16}O,^{8}Be)^{20}Ne$ reaction has been used in several studies of the ^{20}Ne nucleus [Esw 93, Sug 95]. ^{20}Ne is a particularly attractive nucleus to study because it consists of two neutrons and two protons outside a ^{16}O core. This makes it suitable for simple cluster model calculations and was in fact one of the first nuclei to be treated in this way [Buc 75].
Experimentally, ^{20}Ne has been investigated using a wide range of reactions [Hin 83, Rae 94a], which have identified a number of rotational bands below E_x=20 MeV. A first attempt was made at classification of these bands by Litherland et al. in 1961 [Lit 61]. Since then several more rotational bands have been found and re-classifications have been made by a number of groups [Hin 83, Ric 84a, Ric 84b].
The levels observed in this study have been identified by comparison with the work of Allcock [All 86]. The agreement between the two studies is excellent, allowing firm energy and spin assignments to be made to the levels observed. These assignments were documented in Table 5.1.
These levels can be assigned to the rotational bands proposed by Hindi et al. [Hin 83] and are given in Table 6.1. The bands are variously described by shell model and cluster model calculations. Of particular interest to this study are peaks 10, 11 and 14 at 15.874 MeV, 16.581 MeV and 21.062 MeV respectively. These levels belong to the 0_3^+ and 1^- bands which are strongly populated by eight particle transfer; they

Peak	Level in ^{20}Ne	Assigned Rotational Band						
Number	(MeV)	0_1^+	0^-	0_4^+	0_2^+	0_3^+	1^-	
		shell	^{16}O-α	^{16}O-α	shell	^{12}C-2α	^{12}C-2α	
g.s.	0.0	0^+						
1	1.6337	2^+						
2	4.2477	4^+						
3	5.7877		1^-					
4	7.1563		3^-					
5	8.7776	6^+						
6	10.262		5^-					
7	11.951	8^+						
8	12.585			6^+				
9	13.928				6^+			
10	15.874					8^+		
11	16.581						7^-	
12	17.295			8^+				
13	19.884							7^-
14	21.062						9^-	

Table 6.1: *The assigned rotational bands for the peaks observed in* ^{20}*Ne.*

Level in ^{16}O (MeV)	Assigned Spin	Structure
0.0	0^+	spherical / tetrahedron
6.05	0_2^+	$^{12}C_{g.s.}$-α (kite)
6.13	3^-	tetrahedron
6.92	2^+	$^{12}C_{g.s.}$-α (kite)
7.12	1^-	
10.35	4^+	$^{12}C_{g.s.}$-α (kite)
11.10	4^+	
15.25	(6^+, 5^-, 3^-)	

Table 6.2: *Shape assignments for the observed levels in ^{16}O.*

are therefore considered to be fairly pure ^{12}C-^{8}Be or ^{12}C-2α bands [Mid 71, Zhu 84]. These prolate states might be expected to resonate more strongly than other ^{20}Ne states, if a chain state was being observed. Unfortunately the extremely low cross-sections for events in these channels, relative to the background data, prevented a possible measurement of the excitation function for these states. ΔE-E detectors would be needed for a full examination of this final state, to provide full particle identification.

$^{12}C^*$-$^{16}O^*$

The ^{12}C levels detected in these final state channels were at 7.65 MeV (0_2^+) and 9.6 MeV (3^-), while the ^{16}O was identified in a number of low lying levels. These ^{16}O states and their shape assignments in the cluster model are summarised in Table 6.2. By selecting the ^{12}C 0_2^+ and 3^- levels, these channels already contain some degree of deformity. This may make them likely decay channels for a ^{28}Si chain state.

Additionally this channel is analogous to the $^{8}Be_{g.s.}$-$^{16}O_{g.s.}$ final state channel examined by Aliotta et al. in ^{12}C+^{12}C scattering [Ali 94]. They observed a resonance at the same excitation energy in ^{24}Mg, as that observed by Wuosmaa et al., for the six alpha chain state [Wuo 92]. They also observed the characteristic enhancement at $\theta^*_{c.m.}$=90° in the $^{12}C(^{12}C,^{8}Be_{g.s.})^{16}O_{g.s.}$ angular distribution.

In the light of this, excitation functions were measured for the detection of both $^{12}C(0_2^+)$ and $^{12}C(3^-)$, for all ^{16}O levels observed. No enhancements were seen, indicating that no ^{28}Si chain state was being observed to decay through these channels.

^{16}O*-^{12}C*

From this channel, it was hoped to observe the states in ^{16}O above the four alpha decay threshold that have been identified with four alpha chains [Che 67, Ame 82]. In practice the high background obtained for this type of event prevented the positive identification of any states. Gating on the different levels reconstructed for the undetected ^{12}C provided some background reduction and possible peaks were identified at an excitation energy of 20 MeV in the ^{12}C(2^+)-^{16}O channel and at an excitation energy of 17.5 MeV in the ^{12}C(0_2^+)-^{16}O final state channel.
A similar experiment has been performed by Freer et al. [Fre 95] utilising an expanded detector array. By examining the same channels, but with a greatly improved efficiency for detecting the four alpha particles from the decay of the ^{16}O, they were able to identify levels at 17.1, 17.5, 18.0, 18.7, 19.3 and 21.4 MeV. These channels were observed to decay to ^{8}Be-^{8}Be, ^{12}C(7.65 MeV)-α and ^{12}C(9.6 MeV)-α. These observations are in agreement with this data, although a lack of statistics prevents a better comparison.
Although there is no definite identification of states through this decay channel, comparison with the data of Freer et al. shows that the right region in ^{16}O is being reached. This suggests that the decay channel ^{12}C(0_2^+)-^{16}O$_{chain}$ is being probed through the detection of the quasi-three body ^{12}C(0_2^+)-^{12}C(0_2^+)-α and ^{12}C(0_2^+)-^{8}Be-^{8}Be final states, but that no evidence is being observed for the decay of a ^{28}Si chain structure.

6.2 Discussion

The results presented and discussed above would seem to indicate that no seven alpha chain state has been formed through the ^{16}O+^{12}C reaction in the centre of mass region 37.7 MeV to 51.4 MeV with a width $\geq$2 MeV. In the three years since this investigation was begun, much work, both theoretical and experimental, has been devoted to the ^{12}C(0_2^+)-^{12}C(0_2^+) resonance in ^{24}Mg and to chain states in general. This section will attempt to relate this negative result in ^{28}Si to the new work.
The concept of chain like alpha clusters in light alpha conjugate nuclei has a long history both experimentally and theoretically. However it is only with the use of PSSD's in nuclear physics that it has become possible to probe for chain states

in the heavier alpha conjugate nuclei. The discovery of a resonance in $^{12}C+^{12}C$ scattering by a group at Argonne [Wuo 92], close to the energy predicted by Marsh and Rae [Mar 86] for a six alpha chain state in ^{24}Mg, has led to a revitalisation of the subject of chain states. Subsequent to this discovery, much theoretical work has been carried out to try to explain the $^{12}C(0_2^+)$-$^{12}C(0_2^+)$ resonance and the enhancement of the angular distribution in this channel at $\theta^*_{c.m.}=90°$ on resonance. These theories will also be discussed below.

In trying to explain why no chain state has been observed in ^{28}Si, there would seem to be five possible reasons:

1. The wrong energy region was examined,
2. The resonance is too broad / narrow,
3. The chain state does not decay through the expected channels,
4. The formation mechanism for the seven alpha chain is too complex, resulting in a low cross-section,
5. No chain states exist in ^{28}Si.

Although some of these points are inter-related, they will be treated separately below with a final conclusion at the end.

6.2.1 Wrong Energy Region Examined

There are only two published papers that predict the energies of chain states. These are by Horiuchi [Hor 72] and by Merchant and Rae [Mer 92], expanding the work of Marsh and Rae [Mar 86]. Horiuchi suggested that alpha chain like structures should exist in all alpha conjugate nuclei just above the threshold for decay into the constituent alpha particles. In contrast to this, Marsh and Rae suggested that the chain state in ^{24}Mg should lie significantly above the threshold for breakup into 6 alpha particles. Subsequently Merchant and Rae have extended these calculation to cover all alpha conjugate nuclei up to ^{60}Zn [Mer 92].

The excitation energy predictions of Merchant and Rae were used to decide which excitation region in ^{28}Si should be examined, since the prediction of Marsh and Rae of the ^{24}Mg six-alpha chain state resonance was close to the experimental resonance. However the Brink-Boeker nucleon-nucleon force [Bri 67], used by Merchant and Rae, does not allow them to predict the absolute values of the binding energies accurately, although they can calculate excitation energies relative to the ground state or appropriate breakup threshold. Therefore, when measuring the excitation function in ^{28}Si, a large margin of error was allowed for in this experiment on either side of the expected excitation energy.

6.2.2 Resonance Too Broad / Narrow

By comparison with the $^{12}C(0_2^+)$-$^{12}C(0_2^+)$ resonance in ^{24}Mg, the width of the ^{28}Si chain state resonance was expected to be between 2 MeV and 5 MeV in the centre of mass. Therefore the energy steps were chosen in order to cover this range.

A shape eigenstate model has been suggested [Rae 92a] to account for the width of the resonance in ^{24}Mg and also for the enhancement at $\theta^*_{c.m.}$=90° on resonance. This model assumes that the resonance actually consists of "a coherent superposition of quasi-degenerate resonances belonging to a rotational band having a very large moment of inertia" [Rae 94d]. This means that as the moment of inertia of the nucleus increases, the energy separation between successive angular momentum resonances becomes smaller. Eventually, the moment of inertia becomes so large that the width of the various angular momentum resonances exceeds the differences between their centroid energies, and they become effectively degenerate. The shape eigenstate model can be universally applied to any spatially extended nucleus that has a large moment of inertia [Mer 93]. The only reasonable assumption was to expect that the width of the ^{28}Si chain state resonance should be approximately the same as that for the ^{24}Mg chain.

6.2.3 Experiment Optimised for the Wrong Channel

Until the experiments by Aliotta [Ali 94], Chappell [Cha 95a] and Mirgule [Mir 94], which identified other resonant channels at $E_{c.m.}$=32.5 MeV in ^{12}C-^{12}C scattering, see Section 1.4.4, the dominant fission modes for chain states were expected to be into shorter chains. Recently Merchant and Rae have shown that these new decay modes and their enhanced cross-sections compared to the $^{12}C(0_2^+)$-$^{12}C(0_2^+)$ final state may still be consistent with chain state formation [Rae 94b]. They note that the barriers between minima (and hence different configurations) within the Coulomb barrier are lower than the Coulomb barrier itself at $\theta^*_{c.m.}$=90° and conclude that the spreading width into other alpha cluster configurations is likely to dominate over the escape width.

This conclusion suggests that, while a chain state may breakup into shorter chains, the cross-section for it to do so will be low compared with the yield from other breakup channels. Therefore, in future experiments, it may be better to optimise the detectors for these channels.

6.2.4 Formation Mechanism for the Seven Alpha Chain State is Too Complex

In Reference [Rae 94c] Rae, Merchant and Zhang show that the chain in ^{24}Mg may be formed through mixing of alpha cluster configurations. It has also been proposed that mixing between the ground state and 0_2^+ levels in ^{12}C may provide a mechanism for the excitation of the ^{24}Mg chain through ^{12}C-^{12}C scattering. Indeed it has been shown by Takigawa and Arima [Tak 71] that the ground state of ^{12}C can only be fully explained by adding a 20% chain-like admixture to the triangular structure.
In contrast, the four alpha threshold in ^{16}O lies much higher, so that no mixing is expected between the ground state and any chain configurations. This is likely to considerably suppress the formation of the ^{28}Si chain through^{16}O-^{12}C scattering if this is the correct formation mechanism. Nevertheless, examination of the ^{16}O*-^{12}C* singles channel and comparisons with the work of Freer et al. [Fre 95] seem to indicate that states in ^{16}O are being excited in the excitation energy region of interest and that they decay to ^{12}C(0_2^+)-α and ^{8}Be-^{8}Be, one of the signatures for four alpha chain states. This suggests that with an appropriately sensitive detection system, the suppression of the formation mechanism would not be great enough to prevent detection of any chain state formed.

6.2.5 A Chain State Does Not Exist in ^{28}Si

As a final hypothesis, it seems reasonable to examine other alternatives that have been put forward to explain the ^{12}C(0_2^+)-^{12}C(0_2^+) resonance in ^{12}C+^{12}C scattering, with the assumption that perhaps this resonance can be better explained using a different model. In this case, do these alternatives have any relevance for a seven alpha chain in ^{28}Si?
Chain states are undoubtedly the most contentious of all the predictions made by cluster models. This is particularly true of the assignment of a chain state structure to the ^{24}Mg resonance at 32.5 MeV in the centre of mass. In this section two models are presented that offer an alternative explanation of the ^{12}C(0_2^+)-^{12}C(0_2^+) resonance in ^{12}C.
One alternative explanation may come from the work of Hirabayashi et al. [Hir 95]. They have used a modified Band Crossing Model [Abe 78, Mat 78, Kon 79], based

on crossings of the molecular rotational bands due to the intrinsic spins of the excited nucleus. Using this model they predict that the resonance in the $^{12}C(0_2^+)$-$^{12}C(0_2^+)$ exit channel is due to a weakly coupled structure of two groups of three alpha particles (0_2^+ in^{12}C), which they claim is different from the linear chain configuration. Unfortunately, to obtain this result they are required to include many coupled channels, making it difficult to interpret these results in terms of the underlying nuclear structure. In addition, their enhancement at $\theta^*_{c.m.}$=90° does not resonate with energy, in contrast with the experimental data.

Rae and Merchant have also used an approximate coupled channels approach to examine the six-alpha chain structure [Rae 95a]. They find that in order to produce an aligned state in ^{24}Mg, they need to identify two highly deformed prolate configurations and associated rotational bands which can be coupled together. Since the 7.65 MeV state in ^{12}C is probably not a fully aligned chain, and the possible chain at 10.3 MeV (0_3^+) does not seem to have an accompanying rotational band [Ajz 86], they cannot form a chain from two ^{12}C nuclei. Alternatively, they suggest that the six-alpha chain should be observed most strongly in the ^{8}Be-^{16}O channel, since four-alpha chain states are known in ^{16}O. Their explanation of the $^{12}C(0_2^+)$-$^{12}C(0_2^+)$ resonance is discussed below. Their argument concerning ^{12}C has a strong bearing on this work because the main formation and decay mechanism of the seven alpha chain is expected to be through ^{12}C+^{16}O. Other possible paths, such as ^{20}Ne+^{8}Be or ^{24}Mg+α suffer from the same problem as ^{12}C; that there is no evidence that, by adding an alpha particle to a chain which is known to exist (viz. ^{8}Be or ^{16}O), a stable configuration can be formed. By this logic, there should be no reason to expect chain structures in any of ^{12}C, ^{20}Ne, ^{28}Si, ^{36}Ar etc. As a corollary to this, they note that, if the resonance in ^{24}Mg is to be describable in the ^{12}C+^{12}C mass partition, then there should be evidence for the decay of this resonance to higher spin, even parity resonances in ^{12}C above 7.65 MeV. Given this, more experimental information on 2^+ and 4^+ resonances in ^{12}C around 11-14 MeV would be desirable.

Rae and Merchant found that they could approximate their potential by a δ-function [Rae 95a]. Using this approximation in a schematic model to examine the chain structure in ^{24}Mg, they find resonances with properties similar to the configurations predicted by the Brink-Bloch model. They predict the energy of the 0^+ member of the six-alpha chain band to be at E_x=39.7 MeV, several MeV below the observed resonance in ^{12}C+^{12}C scattering at E_x=46.4 MeV. If we extend this prediction to ^{28}Si, then, if the same were true, the excitation energy of the seven alpha chain lies well below the excitation region studied in these experiments.

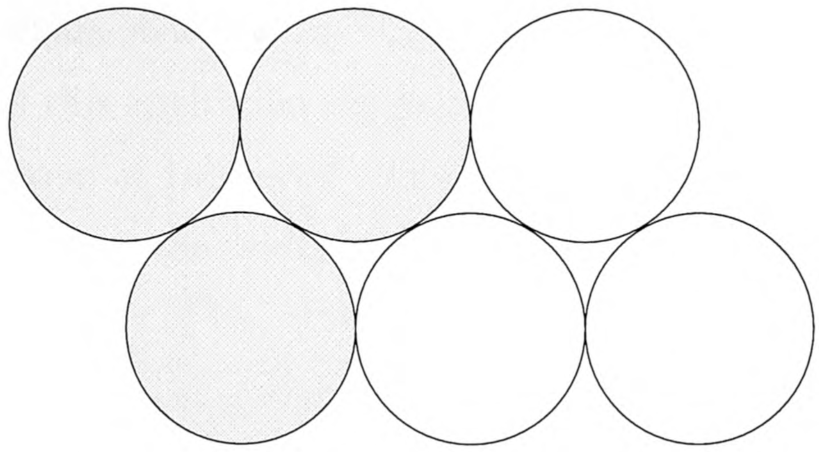

Figure 6.1: *A schematic diagram of the F1 configuration in ^{24}Mg, from Reference [Mar 86]. The shaded and unshaded circles represent the two ^{12}C nuclei.*

Recently, Rae, Fry and Merchant have suggested that in fact the resonance in ^{24}Mg may have an alternative explanation [Rae 95b]. In response to the new and much more extensive angular distribution data from Argonne [Wuo 94b] and from Chappell et al. [Cha 95b], they suggest that these resonances involve the F1 alpha-cluster configuration predicted by Marsh and Rae [Mar 86] which resembles two ^{12}C nuclei, side by side, with their symmetry axes aligned along the same direction, see Figure 6.1. In addition to correctly predicting the energy of the resonance and the enhancement of the resolution at $\theta^*_{c.m.}$=90°, this model also produces pronounced peaks at $\theta^*_{c.m.}$=36° and 57°, in reasonable agreement with the new data.

6.3 Conclusion

This study has used the ^{16}O+^{12}C reaction to examine the excitation region in ^{28}Si between 54.5 MeV and 68.2 MeV, in the search for a seven alpha chain. This search centered on E_x=60.2 MeV, the excitation energy at which Merchant and Rae predicted that the chain state should exist. The favoured decay channel was expected to be through shorter chains, of which, the ^{12}C(0_2^+)+^{16}O$_{chain}$ was thought to be the most easily identifiable. The detectors were thus optimised for this channel. No resonance was observed in this decay channel with 2MeV$\leq \Gamma_{c.m.} \leq$5 MeV. Three other decay channels have also been identified in this data, these are ^{8}Be-^{20}Ne*, ^{12}C*-^{16}O* and ^{16}O*-^{12}C*. Again, no resonance was observed, although comparisons with other experiments show that the expected excitation regions in the decay fragments were being reached. From these findings, we conclude that no chain structure has been found in ^{28}Si between the excitation energies of 54.8 MeV and 68.2 MeV with a width between $\Gamma_{c.m.}$=2 MeV and 5 MeV.

Various ideas have been discussed in this chapter to account for this negative result. Although the mechanism for the excitation of the ^{16}O chain is expected to be more complex than for a chain structure in ^{12}C, the results show that some ^{16}O nuclei are being detected from this excitation region. Hence it is thought that a mechanism exists for the formation of the seven-alpha chain in ^{28}Si. Also, there seems to be no reason to expect that the width of the chain state resonance in ^{28}Si will be unduly different from that of the ^{24}Mg chain state resonance. Thus, it seems that the apparently most radical suggestion, that the chain either does not exist at these excitation energies, or that it does not exist at all in ^{28}Si, must be taken seriously. In either case, this also raises questions about the assignment, to the resonance at E_x=46.6 MeV in ^{24}Mg, of a chain structure. Indeed, there have been a number of models proposed that explain the data well, but do not invoke the chain state hypothesis. However, before the idea of chain states is completely rejected, there would seem to be good grounds for a search in both ^{24}Mg and ^{28}Si, at lower energies, just above the alpha-decay threshold to look for evidence of a chain.

6.4 Outlook

While there would now seem to be some doubt concerning the assignment of the chain structure to the resonance at E_x=46.6 MeV in ^{24}Mg, there is no doubt that whatever its structure, it is certainly very unusual. No other resonance is known to have this enhancement at 90° in the angular distribution. Thus it is important to test the predictions of models which pertain to explain these data. The test undertaken in this thesis was to search for a chain in ^{28}Si. Although we cannot rule out the possible existence of a ^{28}Si chain, we do not observe anything like the effects observed in ^{12}C+^{12}C. The additional theoretical and experimental work that has been undertaken has created several new puzzles and also highlighted new areas in which further study may prove fruitful. It is therefore expected that this subject will remain one of the most keenly discussed topics in nuclear physics. The reason for the lack of experimental evidence for a ^{28}Si chain remains unknown and suggests that there is still much work to be done in the area of cluster structures and chain states, before a full understanding of these phenomena is attained.

Appendix A

Efficiency for the Detection of ^{8}Be and ^{12}C(0_2^+) Nuclei

This appendix describes the method used to calculate the efficiencies for the detection of the breakup fragments from the decay of either ^{8}Be, or ^{12}C(0_2^+), using the PSSD's. These calculations can be performed in isolation, without reference to the rest of the reaction, because these nuclei are relatively long lived and thus do not interact with the target or other decay products.

In both nuclei, the relative energy between the breakup fragments is much less than the kinetic energy of the parent nucleus. This means that the decay products emerge well focussed along the direction of the parent nucleus. However, since both nuclei decay from states with J^π=0^+ [1], the number of events increases towards the edge of the cone. Thus, for good efficiency, the detectors need to be larger than the projection of the cone in the plane of the detectors.

In order to calculate the differential cross-sections, the efficiency must be known for all points on the detector. To do this, a Monte-Carlo simulation was performed. The details of this simulation are covered in the following sections.

A.1 Principles of the Monte-Carlo Efficiency Code

This efficiency code was written to model a single detector in isolation. It works on the principle that if a nucleus hits the detector, then the probability of its detection is 1, anywhere on the detector. In fact, the nucleus breaks up before it can be

[1] States with J^π=0^+ which decay to spin zero nuclei, breakup isotropically in the centre of mass, giving an equal probability for the detection of one of the decay products anywhere on the surface of the breakup sphere.

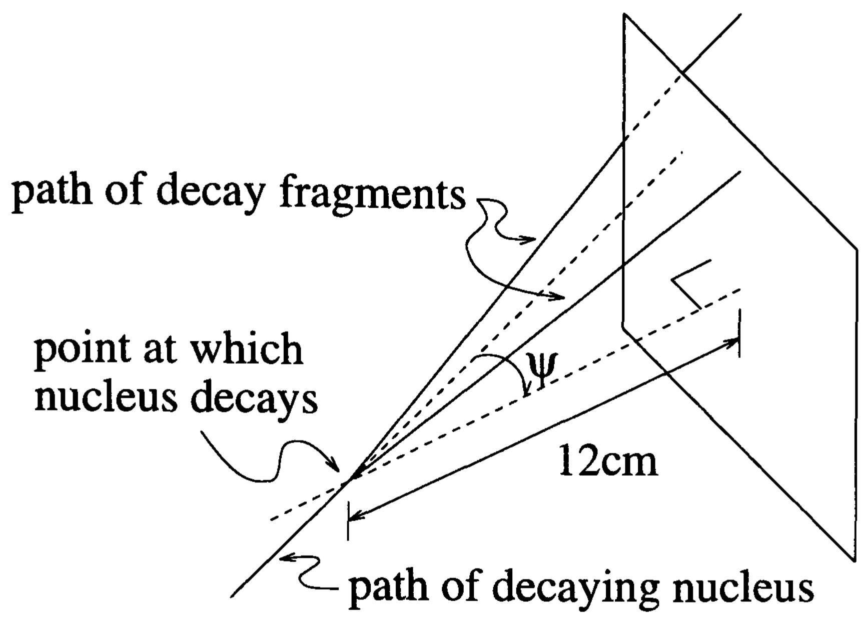

Figure A.1: *Schematic diagram showing one possible path for the decaying nucleus and its breakup fragments.*

detected. Now, because the decay fragments spread out from the original path, the probability that both particles are detected may no-longer be 1. This lower probability is recorded as an efficiency for the detection of the breakup fragments, at the point on the detector where the parent nucleus would have hit.

In these reactions, the decaying nucleus is part of a quasi-three body final state and therefore it may have a range of energies. Thus, the simulation was performed at a number of kinetic energies for the decaying nucleus, between 5 MeV and 100 MeV. Each decay was modelled to occur at the same distance above the centre of the target. The direction of the decaying nucleus was then varied to examine the efficiency at different points on the detector, see Figure A.1.

The decay of the nucleus is isotropic in the centre of mass. Thus, to model it correctly, there must be an equal probability of detecting one of the breakup fragments anywhere on the breakup sphere. The angles at which one of the decay fragments emerges in the centre of mass are chosen randomly, while the other fragment emerges in the opposite direction. The two angles of the decay fragment in the centre of mass are θ and ϕ, where θ is the polar angle and varies between 0° and 180°, and ϕ is the azimuthal angle and varies between 0° and 360°. However, the elemental surface area of a sphere is given by:

$$d\Omega_{c.m.} = \sin\theta d\theta d\phi, \tag{A.1}$$

thus to obtain equal probabilities for the decay into areas of equal solid angle in this simulation, the θ profile must have a $\sin\theta$ dependance. This dependance is introduced by calculating two random numbers A and B. A is calculated in the range 0 to 1, and B in the range 0 to 180. If $\sin B > A$ then the angle θ takes the value of B. If not, then this process is repeated until this condition is met.

When a nucleus decays, the two resulting fragments emerge with a characteristic relative energy, E_{rel} which is dependant on the excited state of the original nucleus, see Section 2.3.2. Conservation of momentum gives the velocities of the two decay fragments in the centre of mass. If the two fragments have masses m_1 and m_2 and have a relative velocity v_{rel}, then their velocities in the centre of mass will be:

$$\underline{v}_{1c.m.} = \frac{m_2 \underline{v}_{rel}}{m_1 + m_2} \quad \text{and} \quad \underline{v}_{2c.m.} = -\frac{m_1 \underline{v}_{rel}}{m_1 + m_2} \tag{A.2}$$

To convert these velocities to the laboratory frame, the centre of mass velocity (equal to the velocity of the parent nucleus, $\underline{v}_{parent}$) is added:

$$\underline{v}_1 = \underline{v}_{1c.m.} + \underline{v}_{c.m.} = \underline{v}_{1c.m.} + \underline{v}_{parent} \quad \text{and} \quad \underline{v}_2 = \underline{v}_{2c.m.} + \underline{v}_{c.m.} = \underline{v}_{2c.m.} + \underline{v}_{parent} \tag{A.3}$$

The path of these decay fragments can now be calculated from the components of their velocities. To determine whether a particular particle would have hit the detector, the angle at which it emerges from the decay is compared with the angles covered by the detector. For a parent nucleus to be tagged as successfully detected, both of its decay fragments must have been detected in different strips on the detector. The efficiency of that position on the detector is re-calculated according to whether or not these criteria are met.

Up to this point, the process by which a two body decay is modelled has only been discussed in general terms. Using this method, the decay of the $^8Be_{g.s.}$ to $\alpha + \alpha$ and $^{12}C(0_2^+)$ to $^8Be_{g.s.} + \alpha$ can both be simulated. However, the $^8Be_{g.s.}$ from the decay of the ^{12}C will also breakup. This can be simulated in exactly the same way as above, only now, the kinetic energy and direction of the ^8Be are calculated from equations A.2 and A.3. The efficiency for the detection of the ^{12}C breakup fragments was calculated for all three final state alpha particles being detected in different strips.

A.2 Variation of Efficiency Across the Detector

The efficiency was calculated at the centre of each strip in 0.25 cm intervals. At each point, 10,000 $^8Be_{g.s.}$ or $^{12}C(0_2^+)$ breakups were modelled. In addition, for each loop in the ^{12}C breakup, the breakup of the resulting $^8Be_{g.s.}$ was modelled 1,000 times. The resulting efficiency maps are shown in Figures A.2 and A.3.

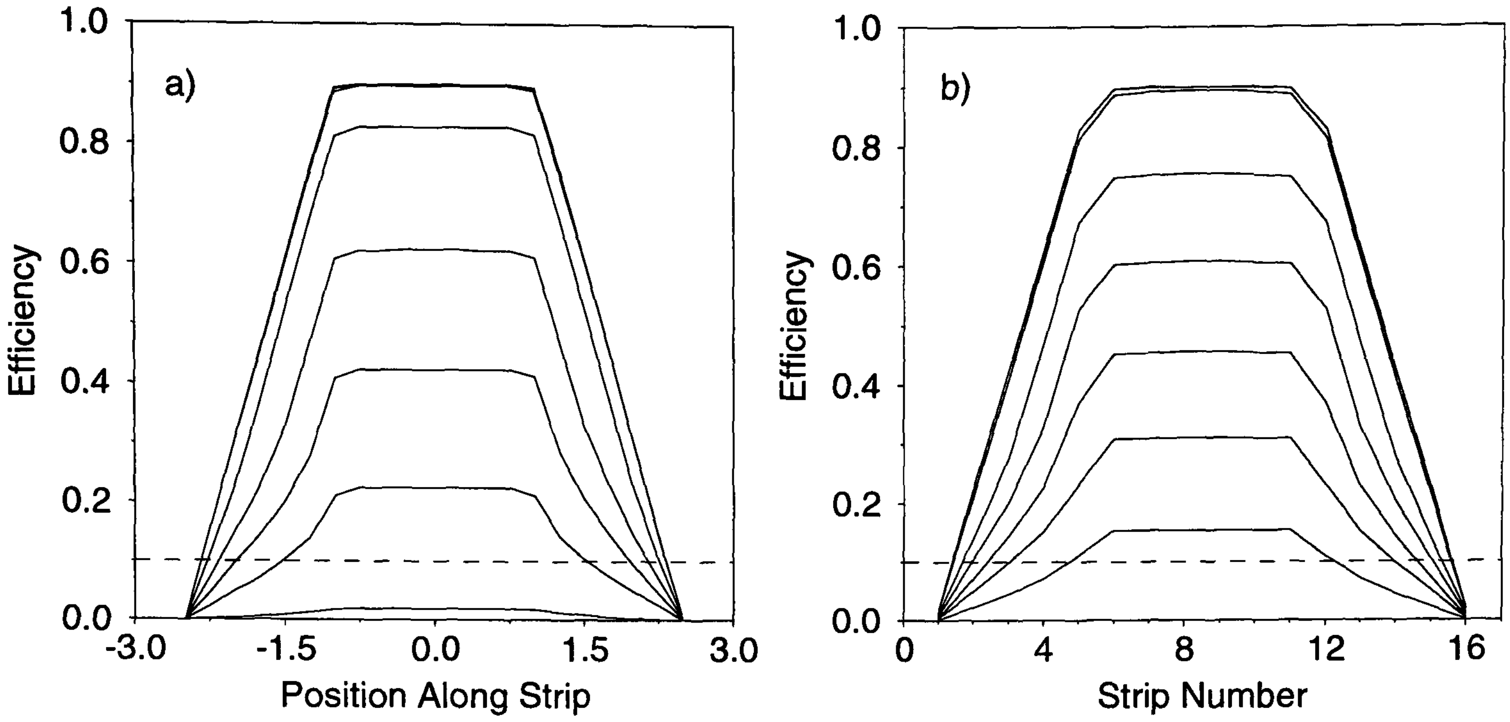

Figure A.2: *The efficiency for the detection of both of the alpha particles from the decay of ^{8}Be, a) along each strip and b) against strip number, at 10 MeV incident energy. The dashed line marks the level at which the efficiency is 0.1.*

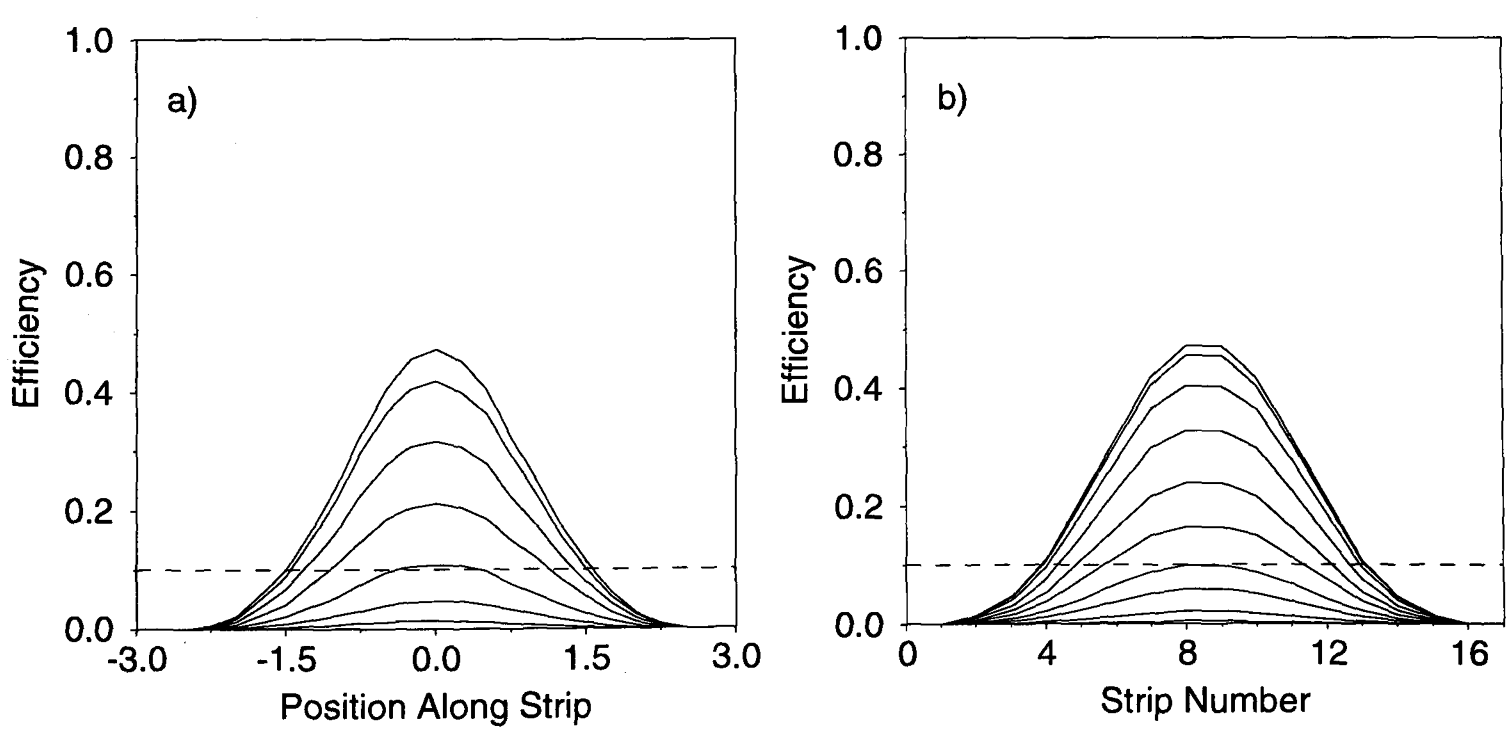

Figure A.3: *The efficiency for the detection of all three of the alpha particles from the decay of $^{12}C(0_2^+)$, a) along each strip and b) against strip number, at 10 MeV incident energy. The dashed line marks the level at which the efficiency is 0.1.*

A.2.1 ^{8}Be Efficiency

The efficiency plots in Figure A.2 are shown for an incident energy of the ^{8}Be of 10 MeV. At this energy, the ^{8}Be breakup cone has a half angle of $\sim$5.4° and a breakup radius at the centre of the detector of about 1.1 cm. Thus, the radius of the breakup sphere is smaller than the dimensions of the detector and so the efficiency for detecting the ^{8}Be is found to be good over a large area of the detector. This efficiency was found to vary by only a small amount over the energy range of interest

A.2.2 ^{12}C Efficiency

Compared with the efficiency for the detection of the ^{8}Be, the efficiency for the detection of the alpha particles resulting from the decay of the ^{12}C in its 0_2^+ level is much reduced, see Figure A.3. The breakup angles for the ^{8}Be and alpha particle decay products are no-longer equal. At 10 MeV, the half angle for the alpha particle decay cone will be $\sim$13.4° giving a radius of 2.9 cm. Since this is now closer to the size of the detector, the efficiency is correspondingly smaller. In addition, the detection efficiency is now strongly dependant on energy, and reduces dramatically for incident energies much below 10 MeV. Above an incident energy of about 20 MeV, the efficiency is greatly increased, almost reaching the same level as for the ^{8}Be.

A.3 Correcting Cross-Sections for Detection Efficiency

To use these results, look-up tables were created for each nucleus. These contained the efficiencies calculated at the different points over the detector for each incident energy. Two-dimensional spline fits were used to interpolate between points and between energies.

During the off-line analysis, for each detected ^{8}Be or ^{12}C(0_2^+), the probability that it was detected could be calculated. By doing this, the number of undetected nuclei of the same type, following the same path, and with the same energy was the inverse of the detection probability. Thus to correct for the efficiency of the detector, the properties of this detected particle could be incremented into spectra for each of the undetected nuclei.

It was found that the uncertainties in the Monte-Carlo calculations below an efficiency of 0.1 were large. Therefore, a cut was made at an efficiency of 0.1 and events below this threshold were rejected. This required a corresponding re-calculation of the solid angle of the detector. This cut did not alter significantly the number of events recorded in the $^{12}C(0_2^+)$-$^{12}C(0_2^+)$-α decay channel.

Appendix B

Study of the Background Contribution from the Strip Detectors

The growing need for large surface area detectors in nuclear and particle physics has led to a number of novel detector designs. The fabrication of these new detectors employs many of the techniques developed in micro-chip design, leading to the possibility that detectors may be designed for specific experiments or experimental setups. The position sensitive strip detectors (PSSD) used in these experiments are a natural extension of the one-dimensional position sensitive detectors (PSD), which have been extensively used in nuclear physics since their invention in the early 1960's [Lau 63, Boc 66]. The PSSD's were developed by Micron Semiconductors for Edinburgh University [Dav 90], and consist of 16×3 mm wide strips etched on to a 5 cm×5 cm silicon wafer, using photolithographic techniques developed by Kemmer [Kem 84]. During these experiments, each strip on a detector was independent, with signals taken off each end of each strip. The charge collection properties and the timing response of these individual strips are therefore expected to be similar to the PSDs, which have been studied extensively [Kal 67, Ben 92]. However, the effect of the proximity of others strips on the operation of each individual strip has not been examined for the PSSDs, and it is this effect that is studied in this appendix.

B.1 Test Setup

These tests utilise the data obtained from the elastic scattering of ^{16}O nuclei from a ^{197}Au target, which was obtained during the calibration runs for the second ex-

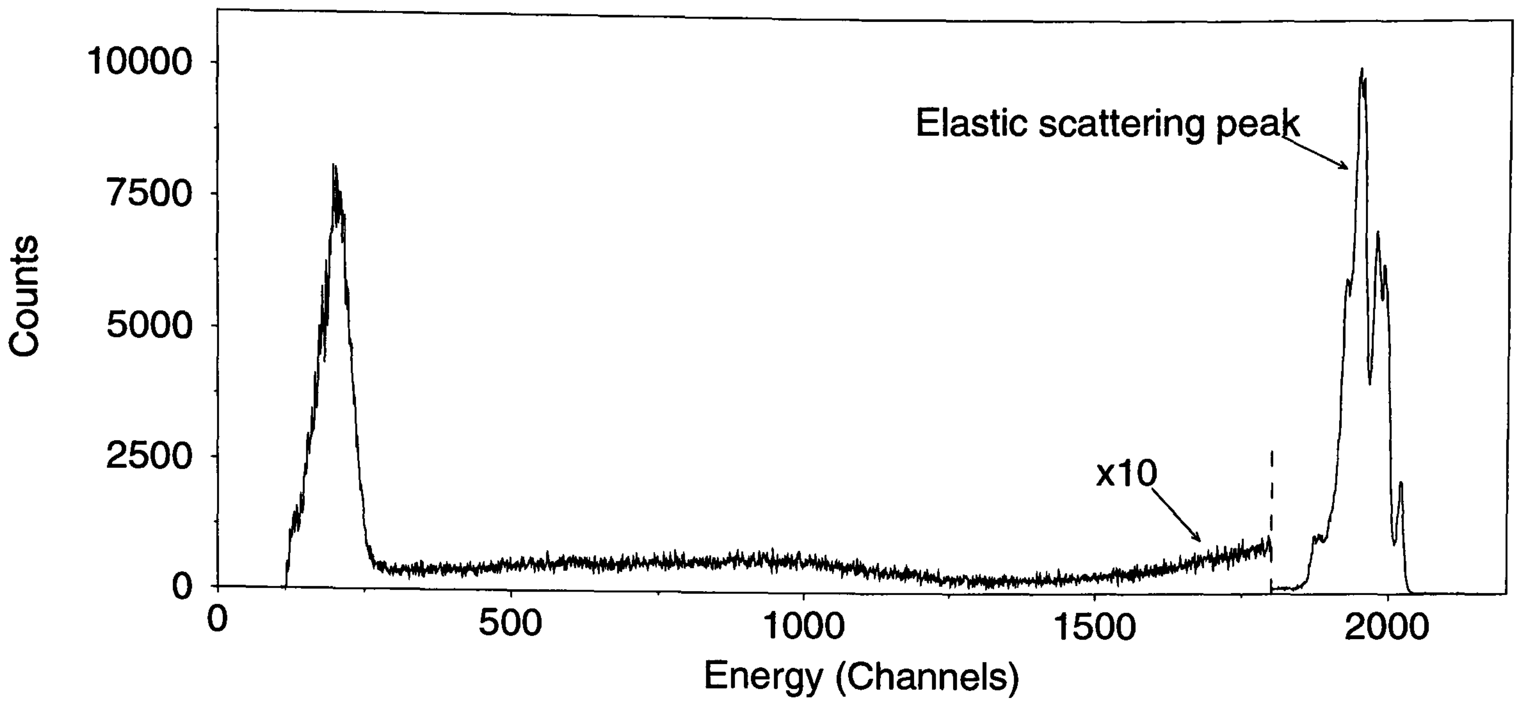

Figure B.1: *The energy histogrammed for all data stored from the elastic scattering of ^{16}O off ^{197}Au. The background has been multiplied by a factor of 10. Structure in the elastic peak is due to the grid on the front of the detector.*

periment at the NSF. The beam intensity during this run was low, so that generally only singles events were detected. The beam energy was 35 MeV, well below the Coulomb barrier for ^{16}O+^{197}Au, and thus only elastic scattering occurred. The two PSSDs were placed at 30.5° on either side of the beam and covered an angular range from ~19° to ~41°. There were no multiplicity requirements placed on the data; any hits recorded in either detector were stored.

B.2 Data Analysis

Although both detectors were examined, no significant differences were observed in the results, and thus only the data from one detector is presented.

A plot of the energy for these data was expected to contain a single broad peak, centered at 35 MeV, corresponding to the elastically scattered nuclei. In fact, when the energy of these events is histogrammed, a small background is seen below the main peak, shown in Figure B.1.

If this data contained only singles events then it would to difficult to study this background further. However, there are also some doubles events, ie. events where two hits were recorded in the same detector. For these events, the energy of the first hit can be plotted against the energy of the second hit, see Figure B.2a. The positions can also be plotted in the same way, Figure B.2b. Using this analysis, the various contributions to the background shown in Figure B.1 can be identified and examined.

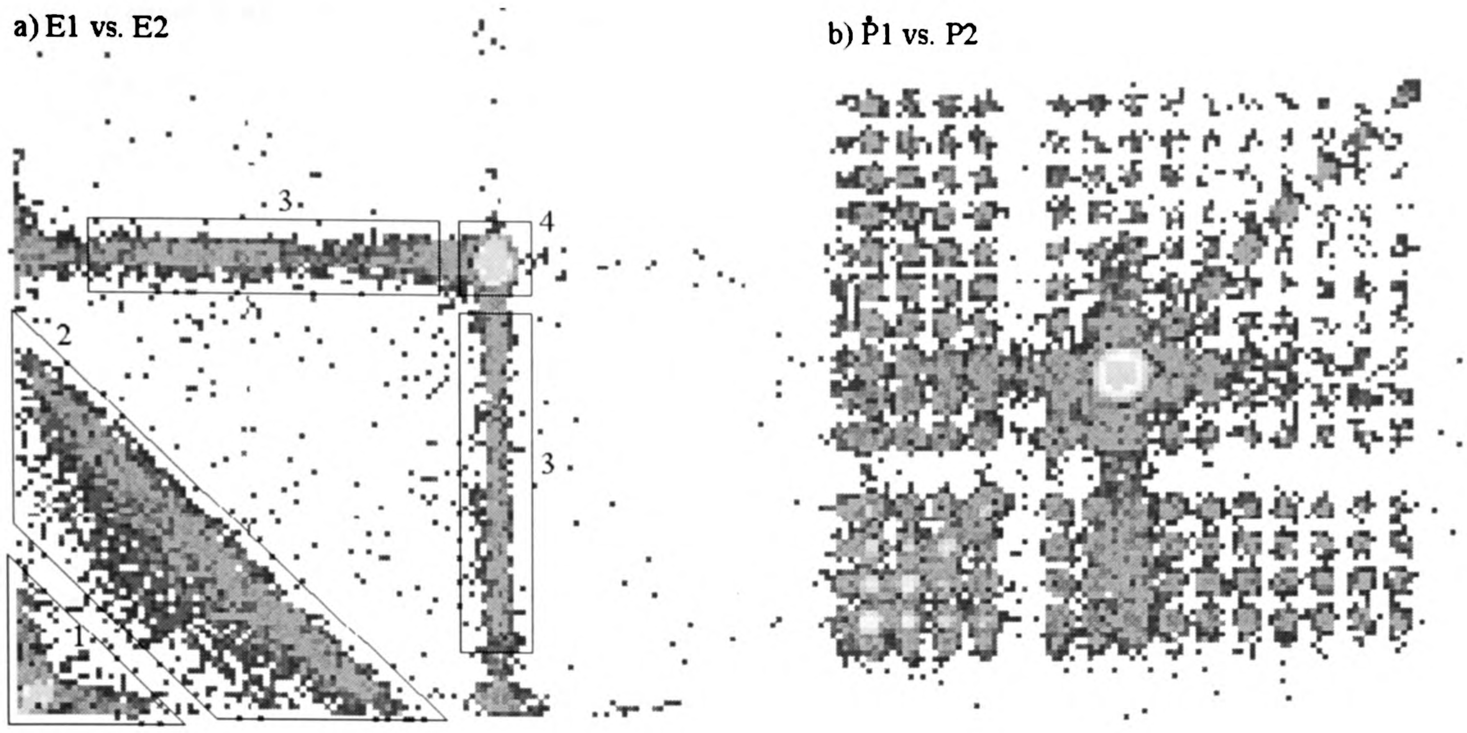

Figure B.2: *a) The energy of the first hit versus the energy of the second hit and b) the position of the first hit versus the position of the second hit.*

B.3 Test Results

The different areas of Figure B.2a have been numbered and are discussed individually below:

1. It was found that these events correspond to the large peak at low energy in Figure B.1. They originated exclusively from strips 1 and 16, and were generally observed in coincidence. In the position spectrum they are characterised by a broad peak at the centre of the detector, seen in the centre of Figure B.2b. It is thought that these events are the result of detector pick-up, and are observed only in strips 1 and 16 because these two strips lie at the edges of the detector, and are therefore most vulnerable to external sources of noise. Since these events occur at the opposite edges of the detector, any attempt to calculate their relative energy will result in an unusually high value, so that they are unlikely to be mistaken for real events.

2. Plotting the position of one of these hits versus the position of the other hit, results in a strongly correlated plot where only the diagonal is present. These events can therefore be identified as particles that have been incident in the gap between two strips and thus whose energy has been shared between the strips. No events were found where the energy was shared between more than two strips.

3. These two areas correspond predominantly to the case where one of the hits was recorded in either strips 1 or 16, while the other hit corresponds to an ordinary event. These events are thought to be caused by one of the particles hitting just outside the detector area and thus only part of the energy is measured by the strip. A small number of events are also observed where neither strip corresponds to an edge strip. In this case, if the position is plotted of the lower energy hit, then it is found that the hit originates at the end of the strip nearest the beam. These events are thought to be generated when one of the particles hits just beyond the end of one strip, they will be discussed again later.

4. This area corresponds to true multiplicity two events where the two scattered particles are detected in separate strips.

Having identified the different sources contributing to the background in the measured energy, it is also of interest to try to measure the relative magnitudes of these effects. In total, the background was found to consist of 16% of the total number of events taken, of which, 40% was contributed by the correlated noise and 60% by the other background effects. Of the other background effects, the inter-strip hits and the hits beyond the end of the individual strips were found to contribute in about equal proportions, while the effect of hits at the top or bottom of the strip were found to contribute a negligibly small amount to the background.

B.4 Conclusion

This analysis shows that the background introduced by the detectors to the energy signal is significantly higher than would be expected if the inter-strip gaps were contributing alone. In fact, the most significant effect, if the correlated noise is to be disregarded, is the effect of particles hitting the detector just beyond the end of the strips. During an experiment, these events could not be differentiated from the real events, since these real events would have a range of energies, and thus could only be removed if a software cut is made near the end of the strip. No method was found to identify and remove inter-strip hits from an experimental run, since the relative energies deposited in the two strips varies considerably and the relative position resembles the relative positions of two alpha particles originating from the decay of an ^{8}Be. Hence, it is thought that inter-strip events will be the only contributing background originating from the detectors, to the ^{8}Be relative energy spectra, however the effect is expected to be below 1%.

Appendix C

A Method for Strip Detector Calibration

The calibration method described below was one of the methods used to calibrate data taken during the experiments in October 1993 at the Australian National University, Canberra. The usual method of calibration is to use a slotted mask in front of the detectors. With this mask in place, data is taken from two low energy elastic scattering runs using different targets. Off-line, the mask gives a position / angle calibration and the elastically scattered nuclei give an energy calibration. Since it is necessary to remove the masks after calibration, the long pump down time and the long time interval, necessary between evacuations of the chamber to allow the sorbation pumps to de-gas, made it impossible to use masks at the ANU. Instead the angles of the centres of the detectors were measured, so that the detectors could be placed at the correct angle relative to the beam line. Then, with the detectors at these angles (30.5° on either side of the beam) elastic scattering data was taken using a 32 MeV ^{16}O beam on ^{197}Au, ^{27}Al and natural carbon targets. This appendix describes one of the off-line procedures used to provide a calibration for the detectors and electronics from this scattering data.

C.1 Notation

A schematic diagram of a typical strip is shown in Figure C.1. If the signals measured at each end of the strip are σ_1 and σ_2, then the measured energy deposited in a strip, E_m, and the measured position along the strip that this energy is deposited, P_m,

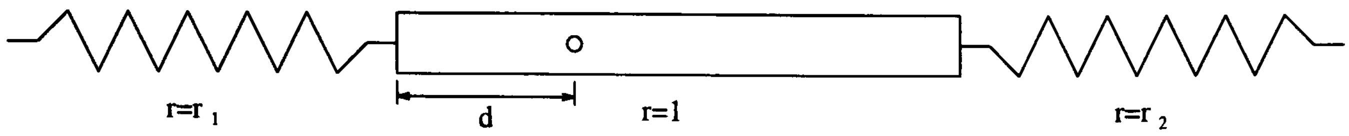

Figure C.1: *Schematic diagram showing a single strip.*

may be written

$$E_m = \sigma_1 + \sigma_2 = \frac{AE(d + r_1)}{1 + r_1 + r_2} + \frac{BE(1 - d + r_2)}{1 + r_1 + r_2}$$

and

$$P_m = \frac{\sigma_1 - \sigma_2}{\sigma_1 + \sigma_2} = \frac{\sigma_1 - \sigma_2}{E_m} = \frac{AE(d + r_1) - BE(1 - d + r_2)}{E_m(1 + r_1 + r_2)}$$

where r_1 and r_2 are the resistances at each end of the strip relative to the strip resistance and A and B are the gains at each end of the strip. It is assumed that any offsets have already been removed. If we then define

$$A' = \frac{A}{1 + r_1 + r_2} \quad \text{and} \quad B' = \frac{B}{1 + r_1 + r_2}$$

we can rewrite E_m and P_m as

$$E_m = A'E(d + r_1) + B'E(1 - d + r_2) \tag{C.1}$$

and

$$P_m = \frac{A'E(d + r_1) - B'E(1 - d + r_2)}{E_m} \tag{C.2}$$

C.2 Input Requirements

At the ends of the strip, d is either 0 or 1, making these the most obvious points to work with. If the energy, E_m, is plotted against position, P_m, see Figure C.2, then the measured energies, E_{m0}^{Au} and E_{m0}^{Al} can be found at P_{m0}, the low end of the strip, and E_{m1}^{Au} and E_{m1}^{Al} can be found at P_{m1}, the high end of the strip. Now equations C.1 and C.2 can be written in terms of these measured quantities. At $d = 0$ (the end of the strip nearest the beam):

$$E_{m0} = (A'r_1 + B(1 + r_2))E_0 = \alpha_0 E_0 \tag{C.3}$$

while at $d = 1$ (the end of the strip furthest from the beam):

$$E_{m1} = (A'(1 + r_1) + Br_2)E_1 = \alpha_1 E_1 \tag{C.4}$$

Similarly at $d = 0$, the position is

$$P_{m0} = \frac{\gamma_0}{\alpha_0} \tag{C.5}$$

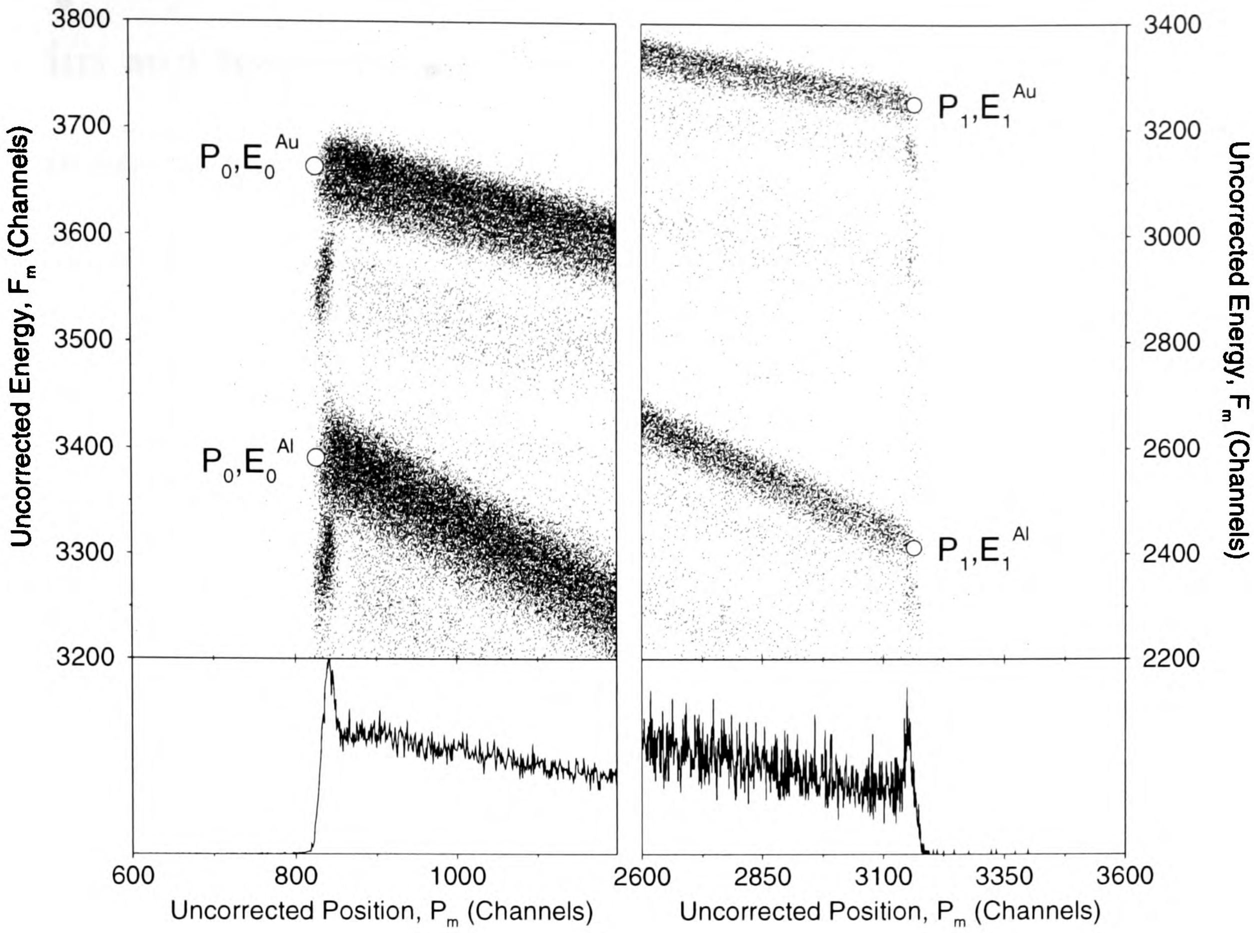

Figure C.2: *Plot of Position versus Energy for calibration data after offset correction.*

and at $d = 1$

$$P_{m1} = \frac{\gamma_1}{\alpha_1} \tag{C.6}$$

C.3 Calculations

C.3.1 Angle and Energy

For the case where $d = 0$, we can see from equation C.3 that the value of α_0 is independent of whether we use E_{m0}^{Au} and E_0^{Au} or E_{m0}^{Al} and E_0^{Al}. This can be exploited using the ratio of equation C.3 for Gold and Aluminium targets:

$$\frac{E_{m0}^{Au}}{E_{m0}^{Al}} = \frac{\alpha_0 E_0^{Au}}{\alpha_0 E_0^{Al}} \tag{C.7}$$

Using kinematic tables to lookup this ratio yields a unique angle at the position $d = 0$, hence E_0^{Au} and E_0^{Al} can also be found. Similarly the angle of the strip at $d = 1$ can be found, along with the energies E_1^{Au} and E_1^{Al}. Now equations C.3 and C.4 can be used to calculate α_0 and α_1, and equations C.5 and C.6 give γ_0 and γ_1.

C.3.2 Gains and Resistances

With some re-arrangement the equations above can now yield values for A', B', r_1 and r_2. Re-arranging equations C.2, C.5 and C.6 gives

$$\gamma_1 = A'(1+r_2) - B'r_2 = A' + A'r_1 - B'(1+r_2) + B' = A' + B' + \gamma_0$$

this yields

$$A' + B' = \gamma_0 - \gamma_1 \tag{C.8}$$

Also, from equations C.1, C.3 and C.4

$$\alpha_0 = A'(1+r_2) + B'r_2 + (B' - A') = \alpha_1 + (B' - A')$$

giving

$$A' - B' = \alpha_0 - \alpha_1 \tag{C.9}$$

Now adding equations C.8 and C.9 gives

$$A' = \frac{\gamma_1 - \gamma_0 + \alpha_1 - \alpha_0}{2} \tag{C.10}$$

while subtracting these equations gives

$$B' = \frac{\gamma_1 - \gamma_0 - \alpha_1 + \alpha_0}{2} \tag{C.11}$$

Similarly taking the definitions for α_0 and γ_0, and α_1 and γ_1 together gives equations for r_1 and r_2.

$$r_1 = \frac{\alpha_0 + \gamma_0}{2A'} \tag{C.12}$$

while subtracting these equations gives

$$r_2 = \frac{\alpha_1 - \gamma_1}{2B'} \tag{C.13}$$

C.4 Using these Results

Since α_0, α_1, γ_0 and γ_1 can be found using the relations from equations C.3, C.4, C.5 and C.6, the gain and resistance at each end of the strip can be calculated and corrected for. By inverting these equations, d and E can be calculated for any values of E_m and P_m.

Appendix D

Selected Levels and Decay Thresholds in ^{8}Be, ^{12}C and ^{16}O

This appendix contains the energy level diagrams for ^{8}Be, ^{12}C and ^{16}O. In ^{8}Be and ^{12}C, the levels are shown up to a maximum energy, while in ^{16}O, only selected levels are shown. In each case, selected decay thresholds are marked. The shaded areas denote the width of the levels.

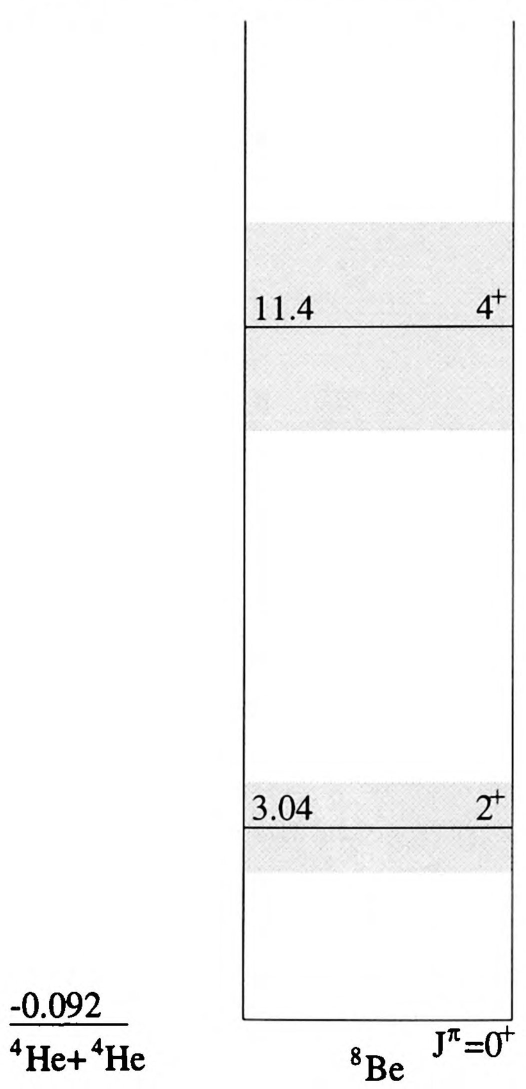

Figure D.1: *The levels in ^8Be below 16 MeV from Reference [Ajz 88].*

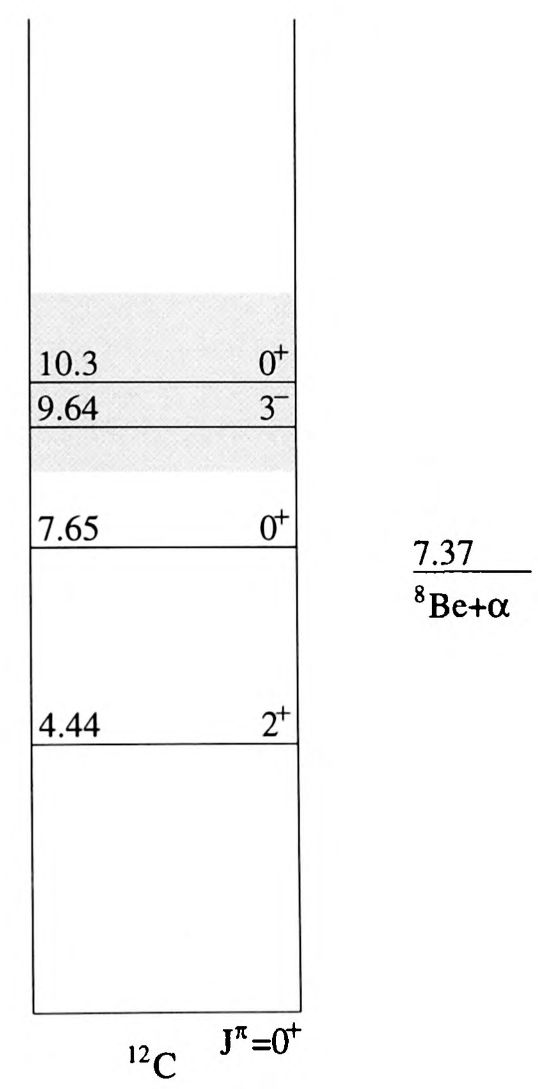

Figure D.2: *The levels in ^{12}C below 10.5 MeV from Reference [Ajz 90].*

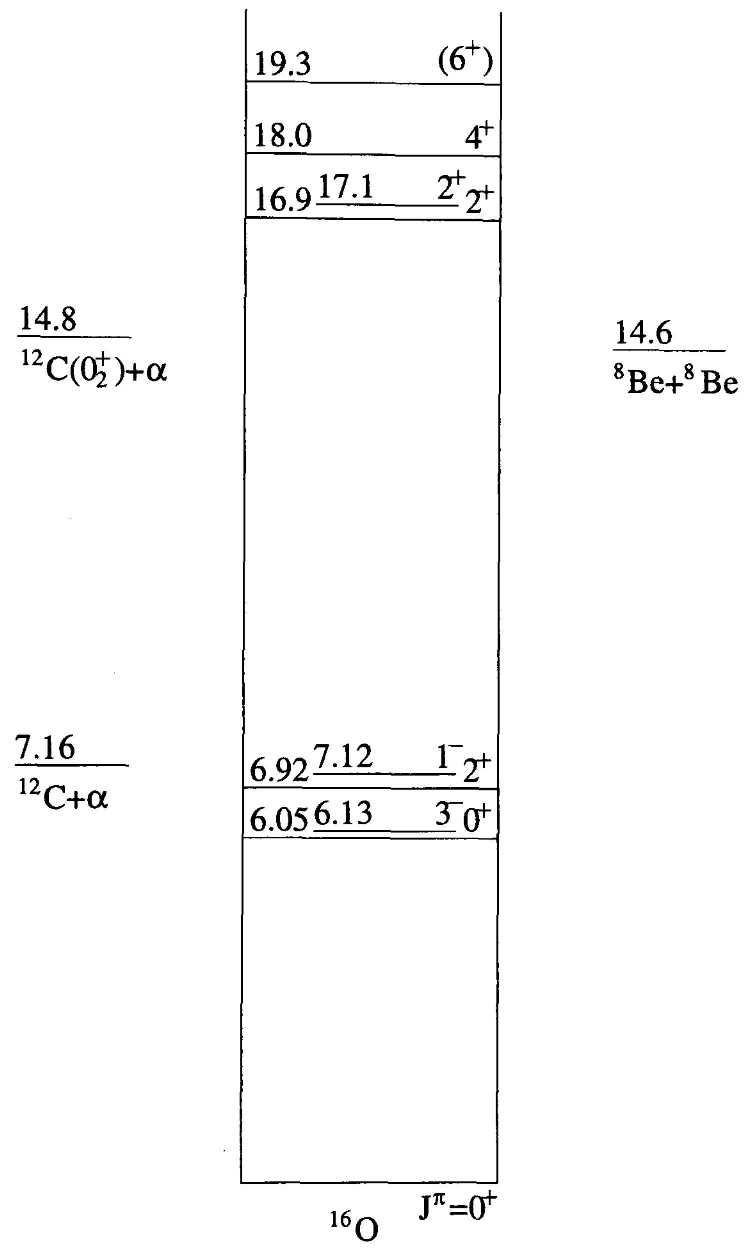

Figure D.3: *Selected levels in ^{16}O below 20 MeV from Reference [Til 93].*

References

[Abe 78] Y. Abe, *Nuclear Molecular Phenomena*, edited by N. Cindro (North-Holland, 1978) p.211

[Abe 80] Y. Abe, Y. Kondō and T. Matsuse, Prog. Theor. Phys. Suppl. **68** (1980) Chapt. IV

[Abg 74] Y. Abgrall P. Gabinski and J. Labarsouque, Nucl. Phys. **A232** (74) 235

[Afz 67] S.A. Afzal, A.A.Z. Ahmad and S. Ali, Rev. Mod. Phys. **41** (1967) 247

[Ait 74] T.W. Aitken, B.S. Halliday, W.T. Johnstone, C.W. Jones, T. Joy, M.C. Morris, N.R.S. Tait and R.P.G. Voss, Nucl. Instr. and Meth. **122** (74) 235

[Ajz 70] F. Ajzenberg-Selove, Nucl. Phys. **A152** (1970) 1

[Ajz 86] F. Ajzenberg-Selove, Nucl. Phys. **A506** (1990) 1

[Ajz 88] F. Ajzenberg-Selove, Nucl. Phys. **A490** (1988) 1

[Ajz 90] F. Ajzenberg-Selove, Nucl. Phys. **A506** (1990) 1

[Ali 94] M. Aliotta, S. Cherubini, E. Costanzo, M. Lattuada, S. Romano, C. Spitaleri, D. Vinciguerra and M. Zadro, Proc. of the 5th Int. Conf. on Nucleus-Nucleus Collisions, Taormina, Italy, May 1994, Book of Abstracts, P.22

[Ali 95] M. Aliotta, S. Cherubini, E. Costanzo, M. Lattuada, S. Romano, C. Spitaleri, D. Vinciguerra and M. Zadro, Nucl. Phys. **A583** (1995) 281

[All 85] S.C. Allcock, computer code RPS, unpublished (1985)

[All 86] S.C. Allcock, D.Phil Thesis, Oxford, 1986

[Alt 81] G.D. Alton, Proc. 3rd Int. Conf. on Electrostatic accelerator technology, Oak Ridge National Laboratory, 1981

[Ame 82] L.L. Ames, Phys. Rev. C **25** (1982) 729

[Ben 68] J. Benn, E.B. Dally, H.H. Müller, R.E. Pixley, H.H. Staub and H. Winkler, Nucl. Phys. **A106** (1968) 296

[Ben 92] S.J. Bennett, J.B.A. England, M. Freer, B.R. Fulton and J.T. Murgatroyd, Nucl. Instr. and Meth. **A311** (1992) 105

[Ben 93] S.J. Bennett, N.M. Clarke, M. Freer, B.R. Fulton, S.J. Hall, O. Karban, J.T. Murgatroyd, G. Tungate, G.J. Gyapong, N.S. Jarvis, D.L. Watson, W.D.M. Rae, A.E. Smith, J.S. Lilley, P.J. Woods and R.D. Page, Nucl. Instr. and Meth. **A332** (1993) 476

[Bit 54] J.W. Bittner and R.D. Moffat, Phys. Rev. **96** (1954) 374

[Boc 66] R. Bock, H.H. Duhm, W. Melzer, F. Pühlhofer and B. Stadler, Nucl. Inst. and Meth. **41** (1966) 190

[Bri 66] D.M. Brink, Int. School of Physics "Enrico Fermi" XXXVII (1966) 247

[Bri 67] D.M. Brink and E. Boeker, Nucl. Phys. **A91** (1967) 1

[Bri 70] D.M. Brink, H. Friedrich, A. Weiguny and C.W. Wong, Phys. Lett. B **33** (1970) 143

[Bri 73] D.M. Brink and J.J. Castro, Nucl. Phys. **A216** (1973) 109

[Buc 75] B. Buck, C.B. Dover and J.P. Vary, Phys. Rev. C **11** (1975) 1803

[Cas 78] G.T. Caskey, R.A. Douglas, H.T. Richards and H. Vernon Smith, Nucl. Instr. and Meth. **157** (1978) 1

[Cha 95a] S. Chappell, D.L. Watson, S.P. Fox, C.D. Jones, W.D.M. Rae, P.M. Simmons, M. Freer, B.R. Fulton, N.M. Clarke, N. Curtis, M.J. Leddy, J.S. Pople, S.J. Hall, R.P. Ward, G. Tungate, W.N. Catford, G.J. Gyapong, S.M. Singer and P.H. Regan, Phys. Rev. C **51** (1995) 695

[Cha 95b] S. Chappell, private communication

[Che 67] P. Chevallier, F. Scheibling, G. Goldring, I. Plesser and M.W. Sachs, Phys. Rev. **160** (1967) 827

[Coo 57] C.W. Cook, W.A. Fowler, C.C. Lauritsen and T. Lauritsen, Phys. Rev. **107** (1957) 508

[Cra 79] H. Crannel, J.T. O'Brien and D.I. Sober, contribution to the Int. Conf. on nuclear physics with electromagnetic interactions, Mainz (1979) No. 3.6

[Dav 90] T. Davinson, A.C. Shotter, E.W. Macdonald, S.V. Springham, P. Jobanputra, A.J. Stephens and S.L. Thomas, Nucl. Instr. and Meth. **A288** (1990) 245

[Dea 67] G. Dearnaley, Contemp. Phys. **8** (1967) 607

[Den 54] D.M. Dennison, Phys. Rev. **96** (1954) 378

[Dri 80] J. van Driel, Ph.D. Thesis, Rijksuniversiteit te Groningen, 1980

[Esw 93] M.A. Eswaran, S. Kumar, E.T. Mirgule, D.R. Chakrabarty, V.M. Datar, N.L. Ragoowansi and U.K. Pal, Phys. Rev. C **47** (1993) 1418

[Fla 78] J.B. Flanz, R.S. Hicks, R.A. Lindgren, G.A. Peterson, A. Hotta, B. Parker and R.C. York, Phys. Rev. Lett. **41** (1978) 1642

[Fre 94] M. Freer, private communication

[Fre 95] M. Freer, N.M. Clarke, N. Curtis, B.R. Fulton, M.J. Leddy, J.S. Pople, S.J. Hall, R.P. Ward, G. Tungate, W.N. Catford, G.J. Gyapong, S.M. Singer, W.D.M. Rae, P.M. Simmons, S. Chappell, D.L. Watson, S.P. Fox, C.D. Jones and P.H. Regan, Phys. Rev. C **51** (1995) 1682

[Fuk 77] Y. Fukushima and M. Kamimura, Proc. Int. Conf. on nuclear structure, Tokyo, 1977 p.225

[Gam 29] G. Gamow, Phys. Zeits. **30** (1929) 717

[Gil 70] A.B. Gillespie, *Electronics For Nuclear Particle Analysis*, edited by L.J. Herbst (OUP, Oxford, 1970) p.138

[Hir 95] Y. Hirabayashi, Y. Sakuragi and Y. Abe, submitted to Phys. Rev. Lett.

[Hin 83] M.M. Hindi, J.H. Thomas, D.C. Radford and P.D. Parker, Phys. Rev. C **27** (1983) 2902

[Hir 95] Y. Hirabayashi, Y. Sakuragi and Y. Abe, Phys. Rev. Lett. **74** (1995) 4141

[Hor 72] H. Horiuchi, K. Ikeda and Y. Suzuki, Suppl. Prog. Theor. Phys. **52** (1972) 89

[Hoy 53] F. Hoyle, D.N.F. Dunbar, W.A. Wenzel and W. Whaling, Phys. Rev. **92** (1953) 1095

[Ike 68] K. Ikeda, N. Takigawa and H. Horiuchi, Suppl. Prog. Theor. Physics Extra Number (1968) 464

[Kal 67] S. Kalbitzer and W. Melzer, Nucl. Instr. and Meth. **56** (1967) 301

[Kam 81] M. Kamimura, Nucl. Phys. **A351** (1981) 456

[Kat 80] K. Katori, K. Furuno, T. Ooi and S. Hanashima, Phys. Rev. C **21** (1980) 1387

[Kem 84] J. Kemmer, Nucl. Instr. and Meth. **226** (1984) 89

[Kon 79] Y. Kondō, Y. Abe and T. Matsuse, Phys. Rev C **19** (1979) 1356
Prog. Theor. Phys. 63 (1980) 722
Phys. Rev. C **22** (1980) 1068

[Lau 63] K.H. Lauterjung, I. Pokar, B. Schimmer and R. Stäudner, Nucl. Inst. and Meth. **22** (1963) 117

[Lea 75] G. Leander and S.E. Larsson, Nucl. Phys. **A239** (1975) 93

[Lit 61] A.E. Litherland, J.A. Kuehner, H.E. Gove, M.A. Clark and E. Almqvist, Phys. Rev. Lett. **7** (1961) 98

[Mar 41] H. Margenau, Phys. Rev. **59** (1941) 37

[Mar 86] S. Marsh and W.D.M. Rae, Phys. Lett. B **180** (1986) 185

[Mat 78] T. Matsuse, Y. Kondō and Y. Abe, Prog. Theor. Phys. **59** (1978) 1009, 1037 and 1904

[Mer 92] A.C. Merchant and W.D.M. Rae, Nucl. Phys. **A549** (1992) 431

[Mer 93] A.C. Merchant and W.D.M. Rae, Invited paper, 2nd International Conference on Atomic and Nuclear Clusters, Santorini, Greece, 28th June-2nd July 1993

[Mid 71] R. Middleton, J.D. Garret and H.T. Fortune, Phys. Rev. Lett. **27** (1971) 950

[Mid 74] R. Middleton and C.T. Adams, Nucl. Instr. and Meth. **118** (1974) 329

[Mir 94] E.T. Mirgule, S. Kumar, M.A. Eswaran, D.R. Chakrabarty, V.M. Datar, N.L. Ragoowansi, H.H. Oza and U.K. Pal, Proc. of the 5th Int. Conf. on Nucleus-Nucleus Collisions, Taormina, Italy, May 1994, Book of Abstracts, P.23

[Mir 95] E.T. Mirgule, S. Kumar, M.A. Eswaran, D.R. Chakrabarty, V.M. Datar, N.L. Ragoowansi, H.H. Oza and U.K. Pal, Nucl. Phys. **A583** (1995) 287

[Mor 56] H. Morinaga, Phys. Rev. **101** (1956) 254

[Mor 66] H. Morinaga, Phys. Lett. **21** (1966) 78

[Nil 55] S.G. Nilsson, Mat. Fys. Medd. Dan. Vid. Selsk. **29** (1955) No. 16

[Nya 84] B.M. Nyakó, J.R. Cresswell, P.D. Forsyth, D. Howe, P.J. Nolan, M.A. Riley, J.F. Sharpey-Schafer, J. Simpson, N.J. Ward and P.J. Twin, Phys. Rev. Lett. **52** (1984) 507

[Obs 72] A.W. Obst, T.B. Grandy and J.L. Weil, Phys. Rev. C **5** (1972) 738

[Oph 74] T.R. Ophel, J.S. Harrison, J.O. Newton, R.H. Spear, E.W. Titterton and D.C. Weisser, Nucl. Instr. and Meth. **122** (1974) 227

[Öpi 51] G.K. Öpik, Proc. Roy. Irish Acad. **A54** (1951) 49

[Pas 75] I.R. Paschopoulos, D.Phil Thesis, Oxford, 1975

[Rae 84] W.D.M. Rae, A.J. Cole, B.G. Harvey and R.G. Stokstad, Phys. Rev. C **30** (1984) 158

[Rae 85a] W.D.M. Rae and S. Marsh, Phys. Lett. B **161** (1985) 251

[Rae 85b] W.D.M. Rae, *Clustering Aspects of Nuclear Structure*, edited by J.S. Lilley and M.A. Nagarajan (D. Reidel Publishing, 1985) p.261

[Rae 88] W.D.M. Rae, Int. J. Mod. Phys. **A3** (1988) 1343

[Rae 92a] W.D.M. Rae, A.C. Merchant and B. Buck, Phys. Rev. Lett. **69** (1992) 3709

[Rae 92b] W.D.M. Rae, A.C. Merchant and B. Buck, private communication

[Rae 94a] W.D.M. Rae, S.C. Allcock and J. Zhang, Nucl. Phys **A564** (1994) 271

[Rae 94b] W.D.M. Rae and A.C. Merchant, Proc. of the VI International Conference on Clusters in Nuclear Structure and Dynamics, Strasbourg, France, 1994, edited by F. Haas (Editions Frontieres, Gif-sur-Yvette, 1995) p.39

[Rae 94c] W.D.M. Rae, A.C. Merchant and J. Zhang, Phys. Lett. B **321** (1994) 1

[Rae 94d] W.D.M. Rae and A.C. Merchant, (unpublished)

[Rae 95a] W.D.M. Rae and A.C. Merchant, Phys. Rev. Lett. **74** (1995) 4145

[Rae 95b] W.D.M. Rae, P. Fry and A.C. Merchant, submitted to Phys. Rev. Lett.

[Ric 84a] H.T. Richards, Phys. Rev. C **29** (1984) 276

[Ric 84b] H.T. Richards, G. Caskey, J.H. Billen, S.R. Riedhauser and D.J. Steck, Phys. Rev. C **29** (1984) 2332

[Rob 73] D. Robson, Nucl. Phys. **A201** (1973) 523

[Sal 52] E.E. Salpeter, Phys. Rev. **88** (1952) 547

[Smi 85] A.E. Smith, S.C. Allcock, W.D.M. Rae, B.R. Fulton and D.W. Banes, Nucl. Phys. **A441** (1985) 701

[Sug 95] T. Sugimitsu, N. Hori, H. Fujita, Y. Funatsu, N. Kato, K. Kimura, M. Matsuo, S. Mitsuoka, T. Mukae, S. Niiya, T. Okamoto, H. Yamaguchi and Y. Nakajima, Nucl. Phys. **A586** (1995) 190

[Suz 72] Y. Suzuki, H. Horiuchi and K. Ikeda, Prog. Theor. Phys. **47** (1972) 1517

[Tak 71] N.Takigawa and A. Arima, Nucl. Phys. **A168** (1971) 593

[Til 93] D.R. Tilley, H.R. Weller and C.M. Cheves, Nucl. Phys. **A564** (1993) 1

[Twi 85] P.J. Twin, A.H. Nelson, B.M. Nyakó, D. Howe, H.W. Cranmer-Gordon, D. Elenkov, P.D. Forsyth, J.K. Jabber, J.F. Sharpey-Schafer, J. Simpson and G. Sletten, Phys. Rev. Lett. **55** (1984) 1380

[Wef 37] Wefelmeier, Naturwiss **27** (1937) 525

[Whe 37] J.A. Wheeler, Phys. Rev. **52** (1937) 1083

[Wuo 92] A.H. Wuosmaa, R.R. Betts, B.B. Back, M. Freer, B.G. Glagola, Th. Happ, D.J. Henderson, P. Wilt and I.G. Bearden, Phys. Rev. Lett. **68** (1992) 1295

[Wuo 94a] A.H. Wuosmaa, Z. Phys. A **349** (1994) 249

[Wuo 94b] A.H. Wuosmaa, M. Freer, B.B. Back, R.R. Betts, J.C. Gehring, B.G. Glagola, Th. Happ, D.J. Henderson and P. Wilt, Phys. Rev. C **50** (1994) 2909

[Zam 92] L. Zamick, D.C. Zheng and D.W.L. Sprung, Phys. Lett. B **293** (1992) 1

[Zha 93] J. Zhang and W.D.M. Rae, Nucl. Phys. **A564** (1993) 252

[Zha 94] J. Zhang and W.D.M. Rae, Nucl. Phys. **A575** (1994) 61

[Zha 95] J. Zhang and W.D.M. Rae, private communication

[Zhu 84] M.V. Zhukov, Sov. J. Nucl. Phys. **40** (1984) 568